Center for Experimental Nuclear Physics and Astrophysics

University of Washington

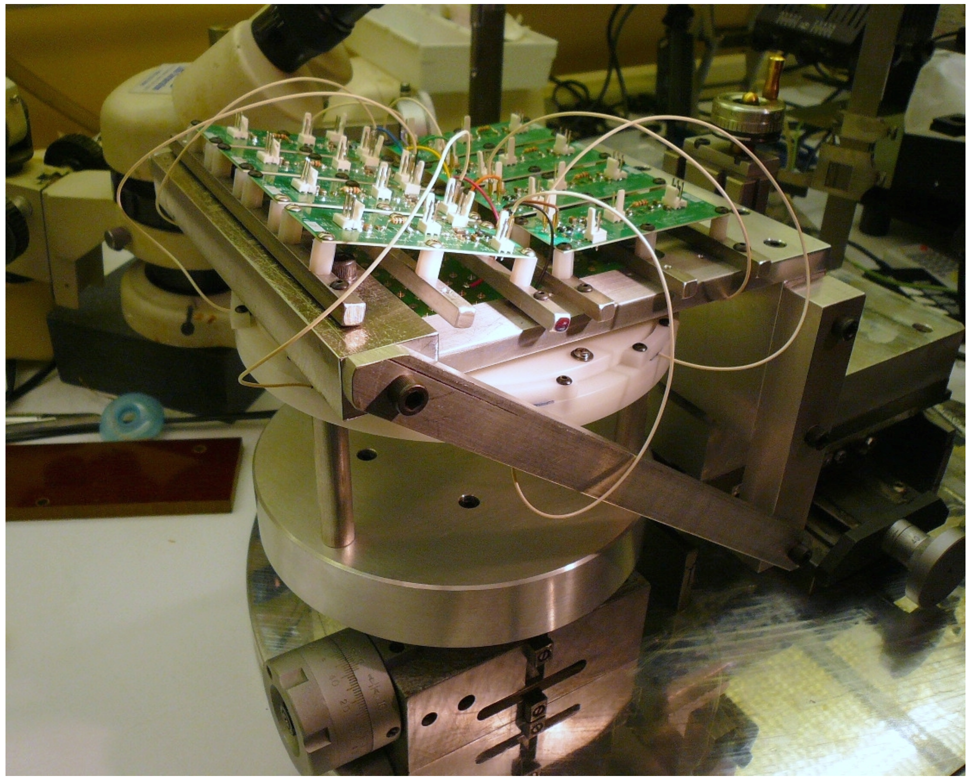

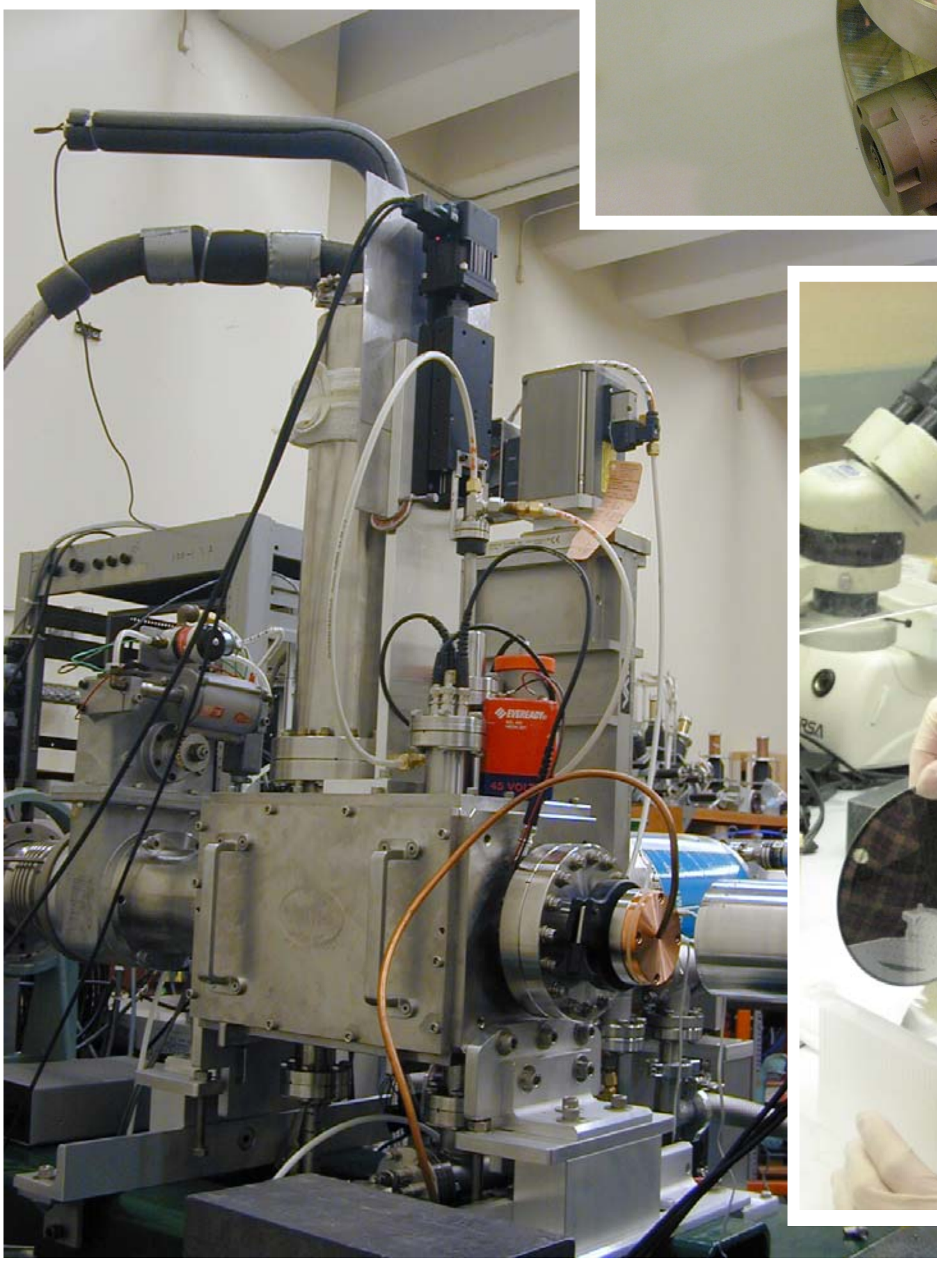

Annual Report 2008

ANNUAL REPORT

Center for Experimental Nuclear Physics and Astrophysics
University of Washington
May, 2008

Sponsored in part by the United States Department of Energy
under Grant #DE-FG02-97ER41020.

Cover photos, clockwise from top to bottom: KATRIN detector test wafer in test mount, Brent VanDevender examining KATRIN detector test wafer, Beamline for the ^{22}Na (p,γ) experiment.
Photos by Brent VanDevender, Laura Bodine, and Anne Sallaska.

INTRODUCTION

CENPA pursues a broad program of research in nuclear physics, astrophysics and related fields. Research activities are conducted locally and at remote sites. CENPA has been a major participant in the Sudbury Neutrino Observatory (SNO) and is presently a major participant in the KATRIN tritium beta decay experiment and the Majorana double-beta decay experiment. The current program includes "in-house" research on nuclear astrophysics and fundamental interactions using the local tandem Van de Graaff, as well as local and remote non-accelerator research on fundamental interactions and user-mode research on relativistic heavy ions at large accelerator facilities in the U.S. and Europe.

We thank our external advisory committee, Baha Balantekin, Russell Betts, and Stuart Freedman, for their continuing valuable recommendations and advice. The committee reviewed our program in May, 2005.

Analysis of the data from the third phase of the Sudbury Neutrino Observatory (SNO) with ^{3}He-filled proportional counters deployed to detect neutrons from the neutral-current disintegration of deuterium is nearly complete. We have contributed extensively to the development of a detailed physics model of the current profiles of ionization events in these detectors to sort out neutron events from other kinds. A number of other important questions that arose in the analysis have been addressed at UW by experimental and analytical work.

The construction of the detector system, the US contribution to KATRIN, has moved forward quickly during the past year. The superconducting magnets, the magnet support system,the multipixel Si PIN diode array, the vacuum system, calibration equipment, and the electronics are now under construction with support from both DOE and the University.

On the Majorana R&D project, we have made advances in a number of areas: an above ground low-background system has been constructed at CENPA and is being used to count samples for both Majorana and KATRIN; in collaboration with LANL a string deployment cryostat test system has been constructed and a hyperpure Ge detector successfully deployed, a new low-background, low-mass crystal mount has been designed and will be used to mount a segmented enriched Ge crystal for low-background testing, several papers have been published or submitted related to the development and verification of our MaGe simulation code.

The Object-oriented Real-time Control and Acquisition (ORCA) system that provides a general purpose acquisition and control system for KATRIN and Majorana continues to be improved. A number of new features have been added including a powerful scripting capability, plug-in filters, and support of a new generation of VME or PCI based single board computers. Additional hardware support continues to be added, in particular for the KATRIN IPE crate and cards, KATRIN related focal plane detector development hardware, and for the GRETINA digitizer board being used by Majorana. A near-time tool based on ORCAroot has been developed facilitating high-level monitoring of the ORCA data stream.

We completed and submitted for publication our analysis of the determination of the superallowed branch from ^{32}Ar, aimed at testing calculations of isospin breaking, of the kind that are used to derive V_{ud}. Our determination, which is the first one of a beta-delayed proton branch to better than 1%, is in good agreement with the model.

We have successfully finished taking data at Jyväskylä to determine the electron-capture branch of ^{100}Tc. This measurement was motivated by testing nuclear-structure calculations related to double-beta decay and our result is in strong disagreement with QRPA calculations.

The rebuilt liquid helium cryostat has been mounted in the neutron spin rotation apparatus at NIST, to measure the neutron-alpha parity-violating amplitude. Data collection over the course of three reactor cycles is in progress.

A continuously rotating torsion balance has been used to measure the differential acceleration of Be and Ti test bodies falling toward the earth, sun, and galactic center as a test of the principle of equivalence. A fractional sensitivity of 2×10^{-13} has been achieved.

A second continuously rotating torsion balance with a pendulum that contains 10^{23} polarized electrons has been used to test Lorentz invariance, non-commutative space-time geometries, and to search for new spin dependent forces. Recent null results from this pendulum (an upper limit of about 10^{-22} eV on the energy required to flip an electron spin about an arbitrary direction fixed in inertial space) probe theories of non-commutative geometries at the scale of 3×10^{13} GeV.

A third torsion balance that is designed to detect the virtual exchange of axions or axion-like particles (mixed scalar-pseudoscalar particles) has achieved its first results, a limit on the dimensionless coupling strength of 10^{-25} down to distances less than one millimeter.

The UCNA collaboration has improved the neutron flux by one order of magnitude over the last year so that it was possible to take data on the beta asymmetry at a rate of 22 Hz. To achieve our ultimate goal, to determine the beta asymmetry with uncertainties of $\sim 0.2\%$ will require still another factor of 5 improvement in the flux. We hope to accomplish that through 2008 as well as take data that will determine the beta asymmetry to better than 1%.

The major milestone of the Axion Dark-Matter eXperiment (ADMX) project was the transition from commissioning to data-taking that occurred late February 2008. The experiment will operate for a year at Laurence Livermore National Laboratory in California. It will then move to CENPA as part of a significant upgrade.

The ^{3}He(^{4}He,γ)^{7}Be experiment was completed and the results have been published.[1] Within an experimental uncertainty of a few percent, we found good agreement between the results obtained by observing the direct gamma rays from fusion and those from counting the ^{7}Be produced. Our combined results give an S-factor of 0.595 ± 0.018 keV b, slightly higher than the previously accepted values.

We have completed and operated the new 0° beamline for the ^{22}Na(p,γ) experiment. We have carried out a number of tests on targets of implanted ^{23}Na so we can anticipate how our implanted ^{22}Na targets will behave under bombardment with intense proton beams. We have modified existing anticoincidence shields to operate with our two large high-purity Ge detectors. Data taking with the ^{22}Na target is anticipated to begin shortly.

[1] T. A. D. Brown, C. Bordeanu, K. A. Snover, D. W. Storm, D. Melconian, A. L. Sallaska, S. K. L. Sjue, and S. Triambak, Phys. Rev. C **76**, 055801 (2007), arXiv:0710.1279v3 [nucl-ex].

Our event structure analysis of RHIC data reveals a sharp transition in the centrality dependence of parton energy loss and fragmentation, both in single-particle spectra and angular correlations, suggesting onset of a QCD energy-loss mechanism that scales with transverse particle density. Novel analysis of the azimuth correlation conventionally interpreted as "elliptic flow" reveals several features inconsistent with a hydrodynamic interpretation and suggests instead that interaction of low-x QCD fields at small energy scales over large space-time volumes may lead to emission of quadrupole radiation fragmenting to hadrons.

We have continued our work on the distorted-wave emission function (DWEF) model, which describes the production and evolution of hadrons in RHIC collisions in terms of their transport through an optical potential that simulates the opacity and diffractive effects of the hot dense medium on the particle spectra and HBT radii, with recent improvements in the model wave functions that give better agreement with expected production temperatures.

Four CENPA graduate students obtained their Ph.D. degree during the period of this report.

As always, we encourage outside applications for the use of our facilities. As a convenient reference for potential users, the table on the following page lists the capabilities of our accelerators. For further information, please contact Greg Harper, CENPA, Box 354290, University of Washington, Seattle, WA 98195; (206) 543-4080, or gharper@u.washington.edu. Further information is also available on our web page: http://www.npl.washington.edu.

We close this introduction with a reminder that the articles in this report describe work in progress and are not to be regarded as publications or to be quoted without permission of the authors. In each article the names of the investigators are listed alphabetically, with the primary author underlined, to whom inquiries should be addressed.

Derek Storm, Editor Victoria Clarkson, Assistant Editor

TANDEM VAN DE GRAAFF ACCELERATOR

A High Voltage Engineering Corporation Model FN purchased in 1966 with NSF funds, operation funded primarily by the U.S. Department of Energy. See W. G. Weitkamp and F. H. Schmidt, "The University of Washington Three Stage Van de Graaff Accelerator," Nucl. Instrum. Methods **122**, 65 (1974). Recently adapted to an (optional) terminal ion source and a non-inclined tube #3, which enables the accelerator to produce high intensity beams of helium and hydrogen isotopes at energies from 100 keV to 7.5 MeV.

Some Available Energy Analyzed Beams

Ion	Max. Current (particle μA)	Max. Energy (MeV)	Ion Source
^{1}H or ^{2}H	50	18	DEIS or 860
^{3}He or ^{4}He	2	27	Double Charge-Exchange Source
^{3}He or ^{4}He	30	7.5	Tandem Terminal Source
^{6}Li or ^{7}Li	1	36	860
^{11}B	5	54	860
^{12}C or ^{13}C	10	63	860
*^{14}N	1	63	DEIS or 860
^{16}O or ^{18}O	10	72	DEIS or 860
F	10	72	DEIS or 860
* Ca	0.5	99	860
Ni	0.2	99	860
I	0.001	108	860

*Negative ion is the hydride, dihydride, or trihydride.

Additional ion species available including the following: Mg, Al, Si, P, S, Cl, Fe, Cu, Ge, Se, Br and Ag. Less common isotopes are generated from enriched material.
In addition, we are now producing a separated beam of 15-MeV ^{8}B at 6 particles/second.

BOOSTER ACCELERATOR

See "Status of and Operating Experience with the University of Washington Superconducting Booster Linac," D. W. Storm *et al.*, Nucl. Instrum. Methods A **287**, 247 (1990). The Booster is presently in a "mothballed" state.

Contents

1 Neutrino Research

SNO

1.1 Status of the SNO Project

J. F. Amsbaugh, G. A. Cox-Mobrand, P. J. Doe, S. R. McGee, A. W. Myers, N. S. Oblath, R. G. H. Robertson, T. D. Van Wechel, B. A. VanDevender, and J. F. Wilkerson

Although data taking at the Sudbury Neutrino Observatory (SNO) detector ended in November, 2006, a wealth of data remain to be analyzed. The third and concluding phase of SNO was a measurement of the rate of neutral-current disintegration of deuterium by solar neutrinos using an array of ^{3}He-filled proportional counters deployed in the heavy water. SNO has already shown in its first two phases that the neutral-current disintegration rate is some three times larger than the charged-current rate induced by electron neutrinos, when normalized with respect to cross section. It was this evidence that demonstrated the solar neutrino problem was due to neutrino flavor conversion, requiring new neutrino properties, specifically mass. The method adopted for the third phase has been designed to use a completely different detection approach, and so also to have completely different systematics.

The signals from the proportional counters are digitized at 1 Gs/s and contain a great deal of information that can be used to distinguish valid neutron capture events from other types of event such as alpha backgrounds and microdischarges. The classification of the information by empirical approaches has led to a substantial improvement in the signal-to-background.

A major activity for us this past year has been the development of a complete physics-based Monte Carlo model for characterizing these pulses. The success of this difficult project has in fact led to a transition within the collaboration as to how the analysis will be carried out for the results soon to be published. It has been made possible by the formation of a dedicated group led by UW graduate student Noah Oblath, and consisting of Oblath, Berta Beltran (Queens University postdoc), Jocelyn Monroe (MIT postdoc), and Hok Wan Chan Tseung, an Oxford graduate student who came to CENPA as a visitor during the 2007-8 academic year. Working closely together, this group managed to solve a number of seemingly intractable difficulties, such as the instantaneous modification of gas gain by positive-ion space charge, the details of avalanche formation, the modifications of pulse waveform due to electronic response and noise, and many other complexities. As is described in the following pages, the success of the resulting Monte Carlo model is striking.

In another challenging aspect of the analysis, it was discovered in studies of low-level Cherenkov light emission that there were three 'hot spots' in the NCD array, isolated locations of radioactive contamination. One was on K2, the other two on K5. Without detailed knowledge of the nature and level of that contamination, the extracted neutral-current rate would be more uncertain, and considerable effort was devoted to quantifying it. An "External Alpha Counter" was built by the UW group to measure surface alpha activities on the suspect counters. Radiochemical measurements were made by the Oxford group. The Cherenkov analysis was placed on a quantitative footing. The combined techniques provided a remarkably clear picture, essentially removing the uncertainty from a level of concern. This work is described below. The source of the contamination, almost pure ^{228}Th, remains unknown.

The integrity of the data obtained from the NCDs must be assured, and a comprehensive program of checks was initiated at UW by Adam Cox-Mobrand, Sean McGee, Keith Rielage (Los Alamos), and John Wilkerson. A very important defect, an intermittent connection at the resistive coupler at the top of the NCDs, was discovered. Detailed analysis showed that only 2 strings, K2 and M8, suffered from this defect. A wide variety of checks confirmed that the other strings in the final set of 30 chosen for analysis performed reliably.

The NCDs, 9 to 11 m in length, were anchored to precisely surveyed points in the acrylic vessel, but the tops were pulled a few cm off in one direction or another from vertical by vagaries in the way the cables ran. The exact positions do not affect the sensitivity to the neutral-current signal significantly, but are more important when point sources of neutrons are deployed in the array for calibration. A special-purpose laser rangefinder designed and built by John Amsbaugh at UW was used to determine the counter-top positions, and the analysis of that data has been recently completed. This has substantially improved the accuracy of efficiency calibrations using point sources.

Although very complex, the analysis of the third phase of SNO is nearing completion, and it is hoped that a paper will be finished early in the summer of 2008.

Sections of the strings of NCDs removed from SNO are now stored in racks in the corridor leading to the SNO cavity awaiting their future use in another application. It is planned that they will be incorporated into a lead-based supernova detector called HALO (Helium And Lead Observatory). Recently NSERC Canada announced its positive decision to provide some funding for HALO.

1.2 Pulse-shape analysis methods for SNO

N. S. Tolich

Two signals contribute to the energy spectrum observed on the NCD array: neutrons and alpha particles. The alpha events have an almost flat energy spectrum between 0.3 MeV and 1.5 MeV, as opposed to the neutron events, which are peaked at approximately 0.76 MeV, and including energy resolution do not go above about 0.85 MeV. The goal of this analysis is to develop parameters other than energy to distinguish the neutrons and alpha particles. Provided the parameter distribution for alpha events is relatively stable as a function of energy below 1.5 MeV, it can be used to eliminate alpha particles without distorting the background energy spectrum. Cuts based on these parameters should remove fewer neutrons than alpha particles to be successful.

We have developed a set of cuts based on the rise and fall times for the pulses after filtering and deconvolving the response of the electronics and the ion mobility. Based on neutron calibration data, the acceptance (the fraction of neutrons retained) of the cuts is 0.801 ± 0.003. The systematic error on the acceptance due to variation of the acceptance as a function of position, date, and other effects is estimated to be 0.007. The alpha rejection (the fraction of alpha particles removed) is estimated be greater than 90 %. This is based on events above the neutron energy peak, events on NCD strings filled with ^{4}He, which do not have a neutron signal, and Monte Carlo simulations of alpha event waveforms.

Fig. 1.2-1 shows the energy spectrum before and after applying pulse-shape cuts. After applying pulse-shape cuts the neutron peak at 0.76 MeV remains, while the alpha particles, which have an almost flat energy spectrum, are significantly reduced.

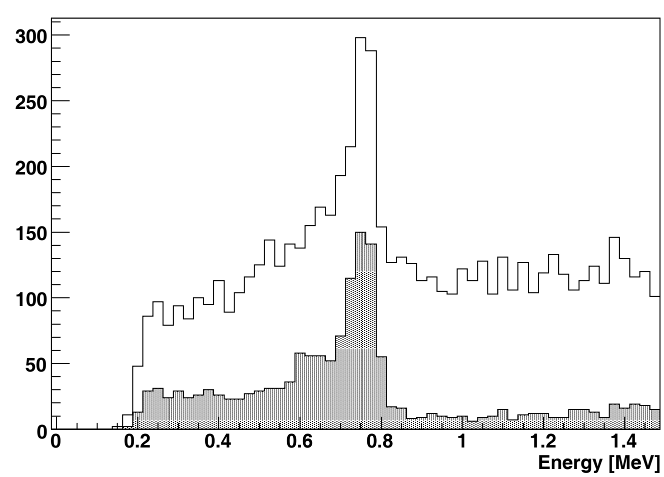

Figure 1.2-1. The energy spectrum of NCD array events. The non-shaded and shaded histograms, respectively, are before and after pulse-shape cuts have been applied.

1.3 Data Integrity Tests for the NCD Phase of SNO

G. A. Cox-Mobrand, B. A. VanDevender, and J. F. Wilkerson

In the third phase of SNO, the ^{8}B solar neutrino flux is being measured using an array of ^{3}He proportional counters. Neutral current interactions occur in the SNO detector when a neutrino breaks up a deuteron, resulting in a free neutron that can then be detected via the n + ^{3}He $\rightarrow$ p + ^{3}H reaction. Extracting the signal from backgrounds relies on the identification of neutron capture events via pulse-shape analysis techniques. Four independent methods are being utilized to extract signals from the SNO data. A model of the NCD DAQ electronics model was developed and quantified, calibrations were performed over the course of the experiment, and a systematic uncertainty in the number of neutrons identified via the pulse-shape analysis techniques due to variations in the measured logamp parameters was estimated for each different method. The parameters that characterize the logarithmic amplification of pulse shapes were found to contribute 1.65%, 0.65%, 0.05% and 0.0% to the systematic uncertainty in the number of identified neutrons in each of the four methods.

A mechanical problem in two NCDs was discovered that caused the detectors to disconnect from the signal cable with little evidence of being disconnected. This problem was discovered while data were still being collected, based on discrepancies observed in the logamp calibration data that were performed on a regular basis. An additional calibration method was developed and implemented to test for this problem in all the detectors during the remainder of the data collection period.

Disconnects, if unrecognized, have the potential to introduce a serious systematic error in the ^{8}B flux measurement. Two independent analysis techniques, one looking at the rate of thermal noise triggers and the other measuring the rates of background alpha events were developed to test the entire data set for any instances of these mechanical disconnects. Both analysis methods gave consistent results. Two NCD strings that suffered from this mechanical problem were identified, and the amount of time that each was disconnected was estimated. The remaining strings were shown to be unaffected by this problem and an upper limit on the amount of time disconnected was estimated. It was determined that these two strings should be removed from the final neutrino flux analysis, with an estimate that their exclusion improved the accuracy of the NCD phase neutrino flux measurement by 1.5%. More details appear in Adam Cox-Mobrand's thesis.[1]

[1]G. A. Cox-Mobrand, Ph.D. Dissertation, University of Washington, 2008.

1.4 Monte Carlo for the Neutral-Current Detection Array in SNO

N. S. Oblath, R. G. H. Robertson, and H. Wan Chan Tseung

The Neutral-Current Detection (NCD) Array in SNO is an array of 36 strings of ^{3}He proportional counters designed to measure the ^{8}B solar neutrino flux via neutral-current interactions on deuterium. We have developed a detailed simulation of the NCD system to be used in the analysis of data from the third phase of the SNO experiment.

In the past year we have made immense progress in moving the simulation from a development stage to production running. The model itself includes detailed aspects of the physical processes that take place, as well as a custom-built simulation of the electronics and data-acquisition system. We simulate the creation of the ionization track, including multiple scattering and energy deposition in the gas, the drift of electrons to the anode, the creation of the avalanche near the anode and the effects of charge saturation, the effects of the ions drifting slowly to the cathode, the propagation of the electrical pulse along the counter, the preamplifier, and the logarithmic amplification before the pulse is digitally recorded. Three simulated neutron pulses are shown in Fig. 1.4-1.

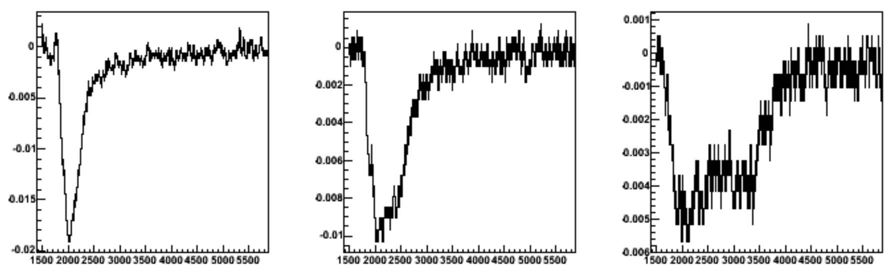

Figure 1.4-1. A small sample of neutron pulses from the NCD Monte Carlo.

Recent improvements to the model included making an *in situ* measurement of the ion mobility in the counter gas. We also improved the implementation of the electronics model by adding secondary pulse reflections from the preamplifiers, which has a particularly significant effect on the shape of narrow current pulses. Furthermore, we added the capability for simulating alpha particles emitted from the endcap regions and anode wires of the counters. Fig. 1.4-2 shows the pulse width vs. energy; the left plot is data, and the right plot is Monte Carlo. The peak near 5 MeV is from polonium alpha decays. A class of pulses can be seen extending above and to the left of the polonium peak; the Monte Carlo data sets clearly show that these are wire alphas. Based on the comparison of Monte Carlo and data we know that the wire alphas are dominated by polonium on the wire surface.

We, along with other members of the SNO Collaboration, have conducted extensive verifications of the Monte Carlo. Comparisons between neutron calibration Monte Carlo and data show that the energy spectrum and distributions of pulse-shape parameters (*e.g.* width, risetime, and kurtosis) are reproduced well by the simulation. The remaining differences between the Monte Carlo and data are fairly well understood and will be addressed in the future. Those limitations on the quality of the Monte Carlo were taken into account when deciding on the appropriate plan for utilizing the simulation.

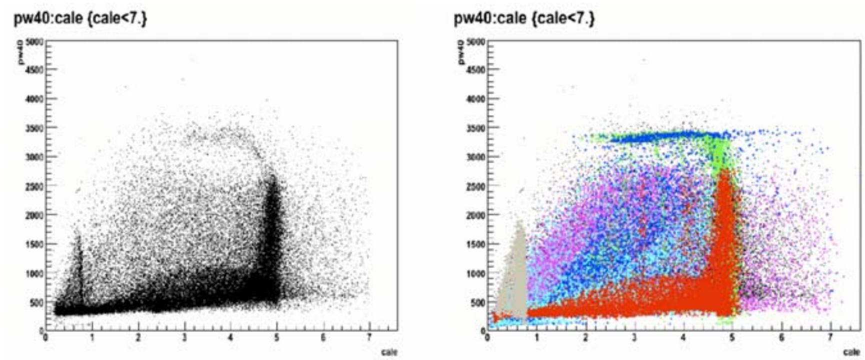

Figure 1.4-2. Pulse-width vs. energy for blind neutrino data (left) and Monte Carlo (right). The Monte Carlo plot includes contributions from different types of alpha particles: Green = Wire Po (surface); Blue = Wire U (bulk); Cyan = Endcap Nickel Po (surface); Red = Nickel Po (surface); Magenta = Nickel U (bulk); Grey = Neutrons. (Color online)

By simulating alpha particles emanating from the endcap regions and anode wires, we were able to account for two classes of previously unexplained pulses. We also analyzed the affects of applying the algorithms designed to remove instrumental backgrounds to the Monte Carlo. There is a slight energy-dependent sacrifice of neutrons ($< 1\%$) by the data-cleaning cuts. The sacrifice when applying the cuts to Monte Carlo agreed well with data within the well-understood accuracy of the simulation.

For the first solar-neutrino analysis from the third phase of the SNO experiment the collaboration decided to use the NCD pulse energies to separate neutron-capture pulses from the background alpha pulses. The Monte Carlo was used to generate the energy spectrum for the alpha background since we do not have an alpha calibration source. We performed fits to determine the relative contributions of alpha particles from polonium near the inner surface of the counter walls and uranium and thorium distributed in the bulk of the nickel walls. The total spectrum, and the contributions from polonium and from uranium and thorium are shown in Fig. 1.4-3. We also did extensive work to determine the relevant systematic effects in the model. We performed simulations after varying these parameters to understand the fluctuations in the energy spectrum due to these parameters. The systematic variations and the central-value energy spectrum are being used in the extraction of the neutral-current neutrino flux from the NCD Array data.

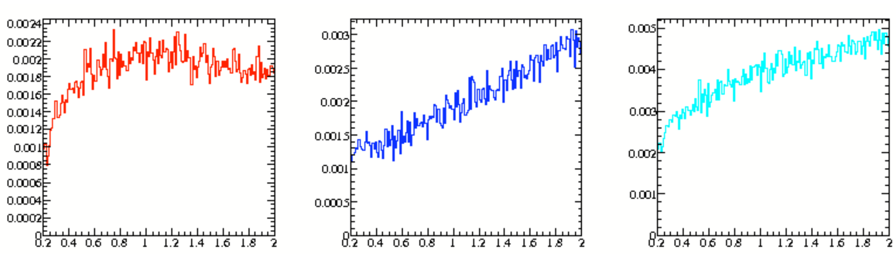

Figure 1.4-3. Pre-PSA MC alpha spectra in the neutron region. Left: Polonium. Center: Bulk = 50% uranium + 50% thorium. Right: Total.

1.5 Multiwire proportional counter for ultra-sensitive detection of alpha activity on surfaces

T. H. Burritt, S. R. McGee, A. W. Myers, R. G. H. Robertson, B. A. VanDevender, and T. D. Van Wechel

Last year we reported the construction and initial commissioning of a new multiwire proportional counter in an article titled "A new external alpha counter for the SNO neutral current detectors." We concluded that article by noting that high-voltage discharges had precluded any measurements of α-emitting contamination on the NCD outer surfaces. We proposed a solution to the problem and shortly after that report we implemented it with great success. The counter has been used to determine the precise composition of two "hotspots" on the NCD denoted as K5 (see Sec. 1.6). Also, the counter was shown to have a spatial resolution of 1.0 cm along its $\approx$ 100 cm length. This latter feature allowed for corroborating radiochemical assays of the active spots by SNO collaborators at other institutions by narrowing the location of the spots from the initial $\approx$ 100 cm uncertainty down to an area $\approx$ 10 cm long.

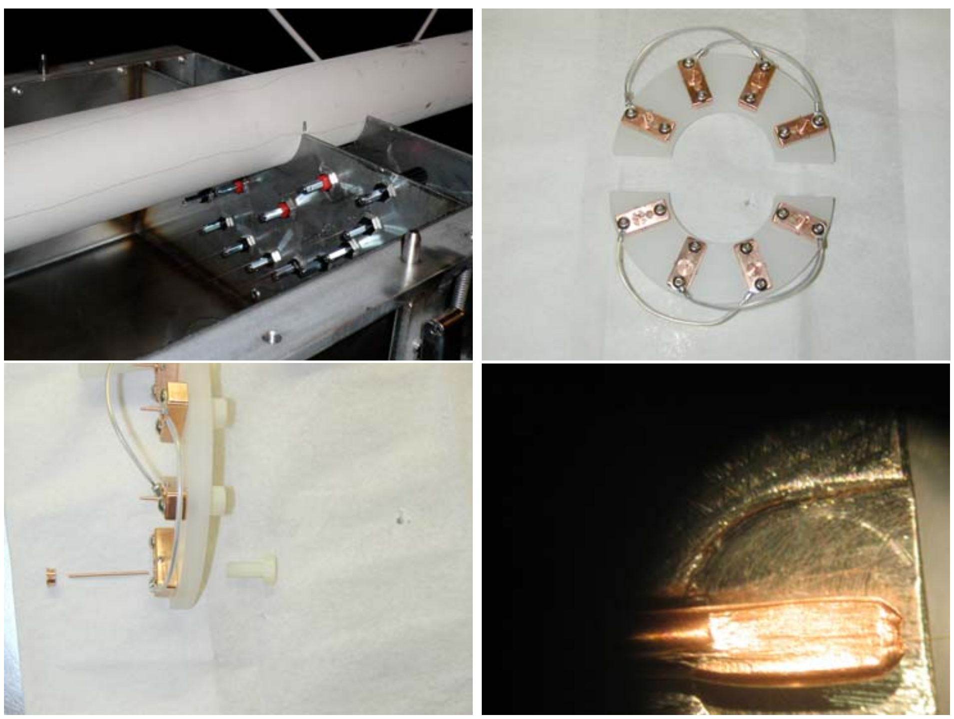

Figure 1.5-1. Clockwise from top left. a: An NCD resting in the lower half of the counter, before modification. The symmetric upper half is lowered into place to enclose the NCD. b: The red anode binding posts in (a) were replaced, due to high-voltage discharges, with the assembly shown here. The white nylon insulators greatly increase the electrical path between the copper high-voltage parts and the grounded chassis. This was done at both ends of the counter. c: A close-up showing how the wire is crimped in a narrow tube to enclose fully the end of the anode wire. d: An exploded view of the binding mechanisms. All of the copper parts have carefully rounded and smoothed edges.

1.6 Analysis of "hotspot" alpha activity on SNO neutron detectors

S. R. McGee, R. G. H. Robertson, and B. A. VanDevender

An analysis of the α-particle emissions from two hotspots on the NCD string labeled K5 has been performed. This analysis looks at the total energy spectrum of α-particles recorded with the new SNO External Alpha Counter (EAC) (see Sec. 1.5). The activity is assumed to consist of ^{232}Th and ^{238}U and all of the daughters in their decay chains, along with a background of ^{210}Po, known to be present on the surfaces of all NCDs. Because radium is readily dissolved in water, we treat the upper and lower parts of each chain independently to allow the possibility that the chains are out of equilibrium. The demarcation between upper and lower chains is made at ^{228}Ra in the thorium chain and at ^{226}Ra in the uranium chain. There is another radium isotope (^{224}Ra) lower in the thorium chain, but it is too short lived (3.6 days) to expect a significant disruption of equilibrium there. The background-subtracted data is fit with a Monte Carlo calculated spectrum, allowing the relative strengths of the decay chains as free parameters. The depth of the distribution in the nickel bulk is also allowed to vary, but good fits are possible only for contamination confined to the surface. Table 1.6-1 and Fig. 1.6-1 show the results of this analysis and the quality of the match between the collected data and our hypothesis about the composition of the hotspots.

This determination of the hotspots' compositions is in agreement with radiochemical assays performed on the contaminated regions. Together, these precise measurements have reduced a potentially large and unforeseen systematic uncertainty $\approx$ 3–4 % in SNO's NCD phase results to $\ll 1$ %.

Table 1.6-1. Final results for K5 hotspot compositions, measured by the mass of the parent nuclei in μg. The uranium numbers are 90 %-confidence upper limits.

Hotspot	$m_{\rm Th}^{\rm up}$	$m_{\rm Th}^{\rm lo}$	$m_{\rm U}^{\rm up}$	$m_{\rm U}^{\rm lo}$
K5 Upper	2.41±0.15	1.03±0.09	< 0.01	< 0.08
K5 Lower	1.60±0.14	0.34±0.06	< 0.13	< 0.07

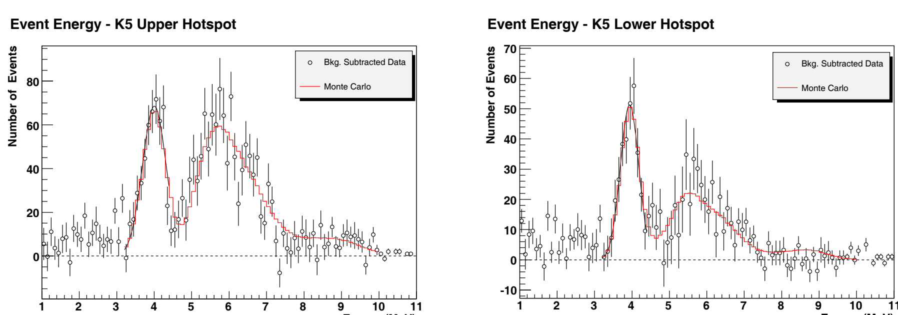

Figure 1.6-1. Background-subtracted K5 hotspot spectra, fit with Monte Carlo-calculated ^{238}U and ^{228}Th α-particle spectra.

KATRIN

1.7 Status of the CENPA contribution to the KATRIN experiment

J. F. Amsbaugh, L. I. Bodine, T. H. Burritt, P. J. Doe, G. C. Harper, M. A. Howe, M. L. Leber, A. W. Myers, R. G. H. Robertson, B. A. VanDevender, T. D. Van Wechel, B. L. Wall, and J. F. Wilkerson.

The KATRIN experiment,[1] currently under construction at the Forschungszentrum Karlsruhe (FZK) in Germany, will attempt to measure directly the mass of the neutrino to a sensitivity of 200 meV by searching for minute distortions in the energy spectrum of electrons produced in the beta decay of tritium. Beta particles from a gaseous tritium source are energy selected by an electrostatic spectrometer. Those beta particles with sufficient energy to pass through the spectrometer are recorded by a detector, yielding the energy spectrum of the beta decay. Small distortions of this spectrum provide a direct measure of the neutrino mass. The US is responsible for providing the beta detection system and the data acquisition system for KATRIN.

The massive spectrometer vessel has successfully undergone a bake cycle and is expected to reach its design pressure of 10^{-11}mbar or less. Approximately 10% of the wire electrodes that will be installed inside the main spectrometer to suppress backgrounds from the vessel walls have been fabricated. The goal is to install the complete electrode assembly by the end of the year. The UW continues to provide support for the commissioning of the pre-spectrometer (see Sec. 1.9). The lessons learned from this experience are proving very valuable in planning the commissioning of the main spectrometer, particularly in understanding the role of Penning traps as a source of background. Commercial fabrication continues on the Windowless Gaseous Tritium Source, the Differential Pumping System, and the Cryogenic Pumping System. The availability of DOE capital equipment funds for the US program in June 2007, coupled with forward funding from the University of Washington, has enabled the US KATRIN program to make significant progress as described below.

In April 2007, as a result of the November 2006 review, the US KATRIN proposal was approved for full capital funding. Unfortunately, the funding profile did not enable timely acquisition of expensive, long-lead items, such as the magnet system and detector. To resolve this problem the University of Washington agreed to provide forward funding to allow these purchases to proceed. As a result the detector wafers will be available in June 2008, and the magnet system (see Sec. 1.11) is scheduled for delivery in July 2008. In October 2007 the final design review of the detector system took place enabling purchase and fabrication to start on the remaining detector system components. All vacuum system hardware has now been purchased, and in-house fabrication of the vacuum housing has begun, with commissioning of the entire system scheduled to begin in June 2008. The final design of the detector consists of an array of 148 PIN diode pixels arranged in a “dart board” pattern. These pixels are read out via an unusual arrangement of pogo pins: spring loaded pins that connect each

[1] More details of the experiment can be found at the official KATRIN home page: http://www-ik.fzk.de/ katrin/index.html

pixel directly to a corresponding feedthrough pin. To further investigate the properties of this system, two test wafers were supplied by Canberra Industries in March (see Sec. 1.12). Although the final readout electronics will be provided by our colleagues at the FZK, we have developed a set of preamplifiers here at UW that is being used to study the test wafers, and, if necessary, the final detectors (see Sec. 1.10). Studies have been made of the efficacy of the “dart board” pixel pattern in understanding the resolution of the spectrometer (see Sec. 1.14). The UW electron gun (see Sec. 1.13) has been modified to test the final detectors. These modifications include the cryocooler that will be used in the actual detector apparatus in KATRIN. The modified gun will be used to quantify the performance of the final detectors. To better understand the various processes that determine the detector performance, Monte Carlo simulations of energy loss in the silicon detector are being carried out (see Sec. 1.15). The ORCA data acquisition system (see Sec. 6.2) has been well received in commissioning the prespectrometer. Capabilities to explore and sort the data using the run header and a real-time data filter have been added and are proving powerful tools in aiding and speeding the commissioning process. ORCA is also compatible with the latest version 4 trigger cards in the readout electronics supplied by FZK.

Our colleagues at MIT and FZK have also been busy. MIT is responsible for supplying the veto, shield and calibration system and is carrying out this work under sub-contract from the University of Washington. Around the time of the design review, improvements to the calibration system were realized that would not only make calibration less costly in terms of run time, but might also enable absolute calibration of the detector efficiency. It was noted by the November Review Committee that although this capability was not essential to meet the physics goals it was nevertheless a desirable parameter to know. This system is being developed jointly by UW and MIT. The IPE group at the FZK, who are responsible for providing the final detector electronics, has successfully prototyped the preamplifiers used to read out the detector. Currently the final preamplifiers are being fabricated using low background ceramic PC boards. Interface to the preamplifiers is provided by the distribution board, also under construction, as are the final fiber optic signal drivers.

2007 was a busy but productive year. 2008 holds similar promise since much ground remains to be covered before a detector system is ready for shipping to FZK in Spring 2009.

1.8 Status of the KATRIN detector vacuum system.

J. F. Amsbaugh and T. H. Burritt

The previously outlined[1] design of the mechanical and vacuum system for the KATRIN focal plane detector (FPD) has been completed. The design accommodates the pinch and detector magnets, cosmic ray veto, radiation shield, FPD calibration equipment, and FPD analog electronics. The vacuum system begins with the DN250 gate valve at the exit of the pinch magnet. After the gate valve is an extreme high vacuum (XHV) chamber with a cryopump, design base pressure 1.0×10^{-11} mbar. The XHV chamber provides mounts for the calibration equipment, vacuum measurement equipment and the 30-kV copper post acceleration electrode which extends into the middle of the detector magnet. At the end of this electrode is the FPD mounted on a feed through flange, with the FPD pre amp box on the outside. A pulse tube cooler cools the FPD and pre-amp by conduction through the ceramic insulator and copper electrode. A medium high vacuum (MHV) chamber, base pressure 1.0×10^{-6} mbar, mounts on the electrode flange providing thermal and high voltage electrical isolation. It is at ground potential and is inside the shield and veto assembly. At the end of the MHV chamber is the signal feed through flange, which is at post-acceleration potential. The stands for the two magnets and vacuum system roll on rails during main spectrometer bakeout (the thermal expansion is significant) to allow removal of the detector magnet, shield, and veto when access yo the FPD is required. The general layout is shown in Fig. 1.8-1.

An extractor ion gauge protects the main spectrometer vacuum and is located via an extension in a low magnetic field. Inverted magnetron cold cathode and conductance gauges are used for magnet-off calibration and bakeout monitoring. A 200 AMU residual gas analyzer (RGA) can diagnose XHV problems. To provide roughing and bakeout pumping, a 200 l/s magnetic-bearing turbo-molecular pump (TMP) backed by a scroll pump is used on the XHV system with a second RGA when isolated for testing and qualification. A dry 70 l/s TMP station is used on the medium vacuum system.

All major components of the vacuum system have been purchased with about one third delivered. The two large gate valves for the XHV chamber donated by the FZK have been received. Construction of the vacuum chambers has begun in our shop. The UW Physics shop has completed 50% of the work on the magnet and vacuum stands.

[1] CENPA Annual Report, University of Washington (2007) p. 13.

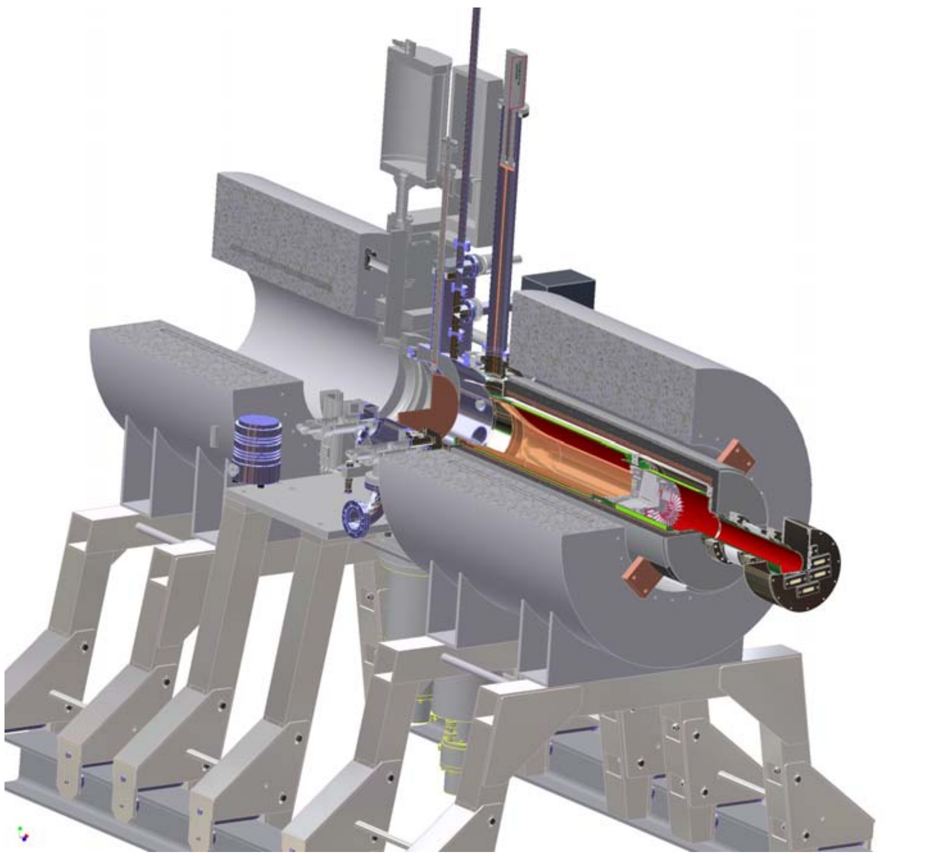

Figure 1.8-1. An overview of the KATRIN FPD assembly with a partial section exposing post acceleration electrode, FPD wafer, feed through flange, pre amp box, MHV chamber, veto scintillator, and radiation shield. Cryopumps are at bottom. MHV vent valves and vacuum measurement equipment are obscured by magnet. The pulse tube cooler and extractor ion gauge (off the top) are positioned high, where the magnetic field is reduced to acceptable levels.

1.9 Progress at the KATRIN prespectrometer

L. Bornschein,* F. Glück,* M. L. Leber, and J. F. Wilkerson

Last year, Penning traps were found at the KATRIN prespectrometer, which prevented simultaneous use of the magnets and high voltage because of breakdowns.[1] The ground electrodes were redesigned and installed in August of 2007, and in November 2007 background measurements with high voltage and magnetic fields resumed. First tests with the redesigned ground electrodes showed the major Penning trap is now gone. Tests at maximum high voltage and magnetic field can be conducted, but a small remaining Penning trap of 200 V is causing an elevated background rate.

The 64-pixel detector intrinsic background had been measured to be very high and to have a large number of events clustered into bursts, but the cause of this was unknown. It was thought that the method of gluing the silicon wafer to the ceramic backing caused stress on the wafer and therefore the bursts. While investigating these bursts, a correlation between the energy of subsequent events in a pixel was found, see Fig. 1.9-1. This pattern

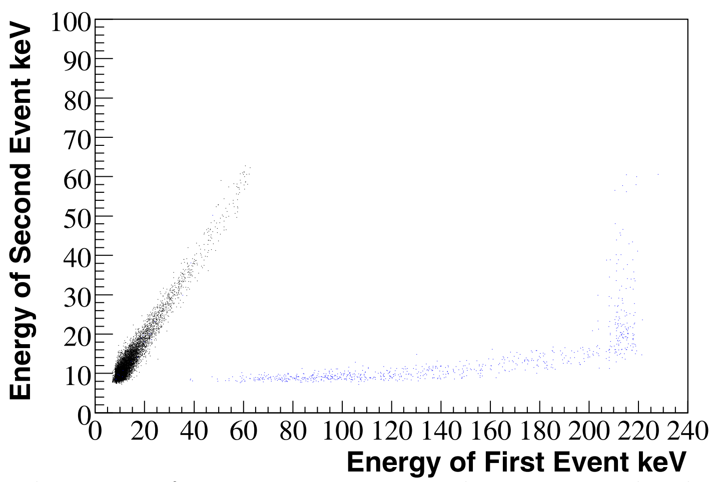

Figure 1.9-1. The energy of consecutive events in a burst are correlated, indicating these are not physics events. The very first event of the burst is shown in blue, and is usually above 60 keV. These are followed by many consecutive events under 60 keV, each with energy close to the previous event. Essentially all events above 60 keV are followed by a burst.

was an indication that physics events above a certain threshold caused bursts. Investigations revealed the fall time of the prespectrometer preamps, 1 ms, was much longer than the pole zero correction time of the shaper card ADC, 39 us. The solution was to remove the resistor that connects the pole zero correction circuit. After this, the bursts disappeared, effectively lowering the intrinsic background rate.

*Forschungszentrum Karlsruhe, Institut für Experimentelle Kernphysik, Postfach 3640, 76021 Karlsruhe, Germany.

[1]CENPA Annual Report, University of Washington (2007) p. 15.

1.10 Low noise preamp developed for KATRIN detector studies

A. W. Meyers, R. G. H. Robertson, C. L. Smith, B. A. VanDevender B. L. Wall,
T. D. Van Wechel, and J. F. Wilkerson

We developed a low noise preamplifier for detector studies for the KATRIN experiment. The amplifier was designed to be paired with a variety of different PIN diode detectors; it is used in deadlayer measurements of Hamamatsu S3590 PIN diodes,[1] systematic studies of CANBERRA CARAC test wafers,[2] and (in the future) the KATRIN calibration system shakedown.

The various uses planned for the preamplifier led to several design criteria. The preamp needed sensitivity to at least 15 keV electrons and had to be vacuum compatible. Also the gain needed to be stable over a range of temperatures. The gain changed less than 0.06% from 20 degrees Celsius to −10 degrees Celsius.

A pulser was connected to the test input of the preamplifier and connected to a KATRIN ADC shaper card to measure the linearity. The KATRIN ADC is the same ADC shaper card originally developed for the emiT and SNO NCD experiments, but has updated FPGA code and shaping times appropriate to the KATRIN experiment. The preamplifier and shaper card deviate from linearity by less than 0.05%.

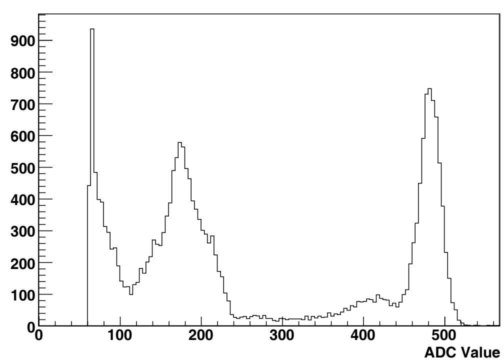

Figure 1.10-1. Americium-241 spectrum measured with the low-noise preamplifier and a Hamamatsu S3590 PIN diode. The highest-energy peak is at 59.45 keV.

An ^{241}Am source was measured with a Hamamatsu S3590 PIN diode connected to the preamplifier input and ADC shaper card. The resulting spectrum (Fig. 1.10-1) had a resolution of 3.9 keV at 59.4 keV(bin 481.7). Also, the spectrum indicates that the lower noise limit of amplifier is 8.7 keV at ADC bin 70.

[1]Hamamatsu Photonics K.K.: www.hamamatsu.com
[2]CANBERRA, 800 Research Parkway, Meriden, CT 06450: http://www.canberra.com

1.11 Superconducting Magnets for KATRIN

T. H. Burritt, P. J. Doe, G. C. Harper, and R. G. H. Robertson

The electrons emitted in the beta decay of tritium in the KATRIN source are guided through the train of pumping restrictions and analyzing potentials by an axial magnetic field. Those that surmount the potential barrier in the main spectrometer regain their kinetic energy and are guided to a 90-mm diameter multipixel Si PIN-diode detector. The axial magnetic field in this region is established by two superconducting solenoids, each capable of 6 T at its midpoint. Fig. 1.11-1 shows the arrangement of the magnets, vacuum system, and detector. With two magnets there is space to insert calibration devices and an isolation

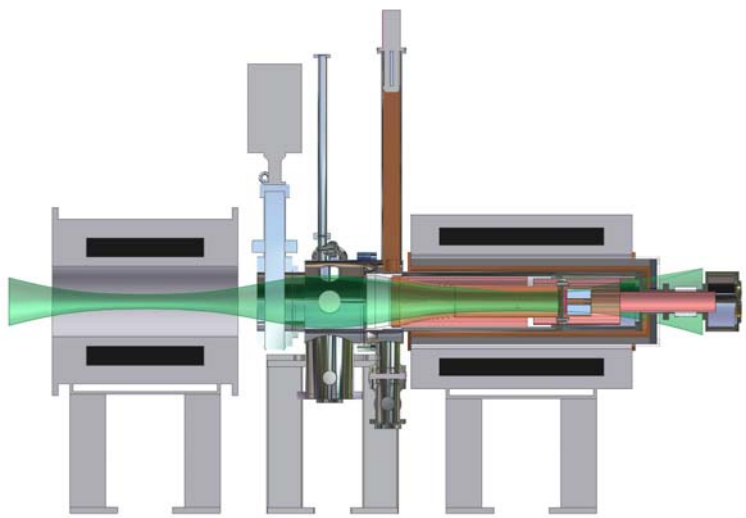

Figure 1.11-1. Cross section of the detector system showing the two magnets. The spectrometer is to the left. The vacuum system is shown only to the right of the gate valve. The magnet on the left is the "pinch" magnet, and the one on the right the "detector" magnet. The flux tube is indicated in green (color online), for a pinch field of 6 T and a detector field at the midplane of 3.6 T. The detector itself is located just to the right of the midplane of the detector magnet where the axial field is 3.3 T, and the detector electronics and connections are rightmost.

valve. The pinch magnet, in addition to its function of collecting the electrons transiting the main spectrometer, also defines the maximum angle relative to the axis that electrons in the source may have in order to be accepted. This serves to eliminate very long trajectories that will suffer inelastic losses. The detector magnet field defines the relationship between the maximum angle of incidence on the detector and the size of the beam spot. Combined with postacceleration, this permits some freedom to choose conditions that maximize signal to background.

The magnets are being constructed by Cryomagnetics, Inc., Oak Ridge, TN. They are LHe-bath cooled, but the liquid is recondensed locally in each magnet by a pulse-tube cryocooler. No refilling is required during normal operation.

1.12 Preparations for KATRIN Prototype Detector Tests

L. I. Bodine, J. A. Dunmore, M. L. Leber, A. W. Myers, C. L. Smith,
B. A. VanDevender, T. D. Van Wechel, and B. L. Wall

KATRIN's focal plane detector will be a large (> 10 cm diameter) monolithic array of silicon PIN diodes. While such detectors are a well-established technology, KATRIN intends to mount the detector and connect electronics in a novel way. Stringent radiopurity requirements dictate that the detector not be mounted on a ceramic backing, as is the usual practice. Nor is it possible to use standard techniques for connecting electronics. Electrical contact between the detector and its front-end electronics will be made with spring-loaded pogo pins. These pins will apply a total force of up to 8 kg on the detector, which is only 0.5 mm thick. It is unknown whether the stresses in the silicon bulk will result in increased leakage currents, and thus noise. We must prove that our mounting scheme is feasible. To do this, we have constructed an apparatus to test a standard large wafer of similar size as the final focal-plane detector under similar stresses. Early tests have indicated that the pogo pins make good electrical contact to the standard aluminum pads and that stress will not be a severe problem. More detailed studies will be done to rule out small subtle effects. The apparatus is shown in Fig. 1.12-1.

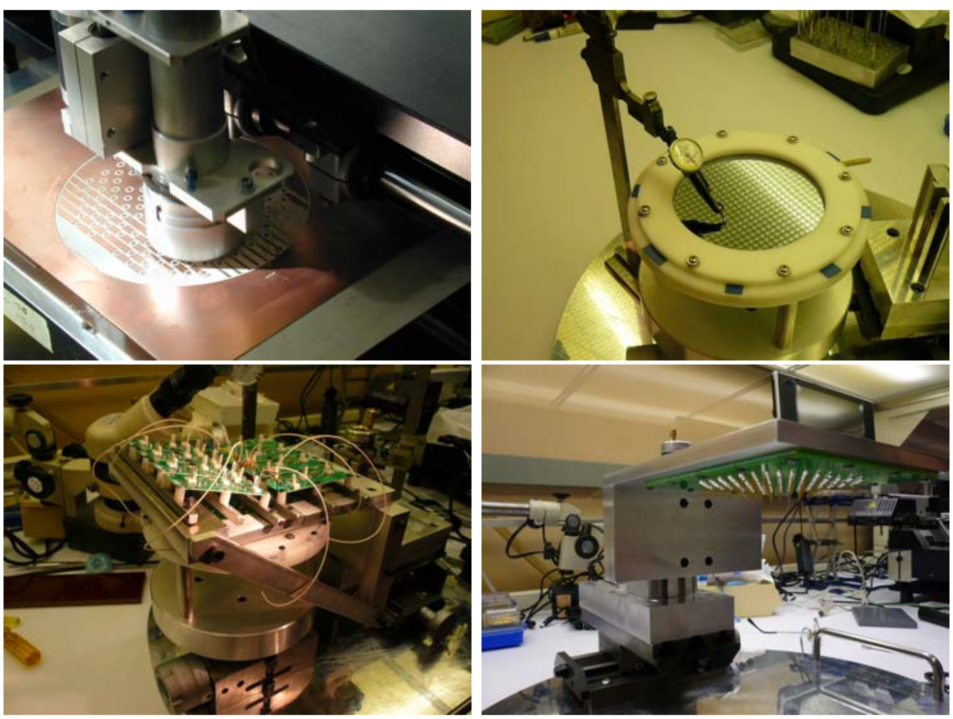

Figure 1.12-1. Clockwise from upper left: a: An electronics dummy was made at UW from a standard circuit board material to have exactly the geometry of conductors, and thus capacitance, as the prototype detector. This was installed in the holder during electronics testing. b: All critical components were aligned to < 0.001 in tolerances. c: The array of pogo pins that presses down from above. d: The complete assembly, with front-end electronics.

1.13 KATRIN electron gun development

P. J. Doe, J. A. Dunmore, G. C. Harper, C. L. Smith, B. A. VanDevender, and B. L. Wall

The monoenergetic electron source was first developed in 2003[1] to profile electron backscattering with respect to incident angle of the large area silicon detectors to be used in the KATRIN experiment. The gun produces low energy electrons by UV photoemission from a stainless steel surface. A UV grade silica fiber and hypodermic needle collimator direct photons from a mercury arc UV lamp onto a 1-mm diameter spot on the cathode emission surface. The electrons are accelerated through a potential that can be varied up to −30kV. The electron beam is focused to a spot on the device under test (DUT) 0.75 m from the emission surface by an einzel lens operating at about half of the accelerating potential. The apparatus uses an electron gun and an einzel lens to produce a tight, focused electron beam of a few Hz to a few kHz. A small aperture in the anode restricts the beam halo. Improvements to the electron gun were made and documented in 2005,[2] 2006,[3] and 2007.[4] Some of the most extensive modifications have been implemented this year. The gun and associated parts are shown in Fig. 1.13-1.

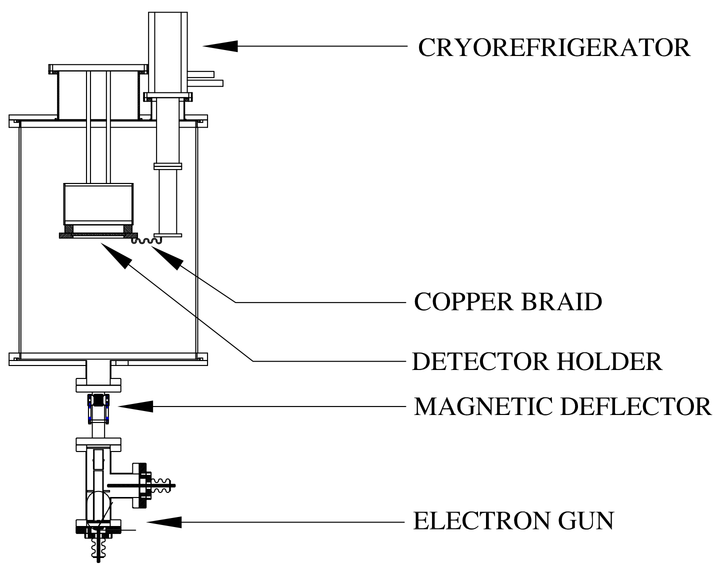

Figure 1.13-1. KATRIN monoenergetic electron gun with magnetic deflector and cryorefrigerator

Prior to the modifications this year, detectors were moved by an X-Y translation table to center the region of interest over the electron beam. This system was plagued by electronics noise from the table motor drive cables. The solution to this problem was to remove the cables during data acquisition. This made data taking very inconvenient. The table also

[1]CENPA Annual Report, University of Washington (2003) p. 65.
[2]CENPA Annual Report, University of Washington (2005) p. 40.
[3]CENPA Annual Report, University of Washington (2006) p. 12.
[4]CENPA Annual Report, University of Washington (2007) p. 17.

required a large amount of real estate in the vacuum chamber. As a solution an externally mounted magnetic X-Y steering system was developed for the gun. The beam is deflected as it leaves the einzel lens by a steel framed magnetic steering assembly. An extension nipple 15 cm long and 4 cm in diameter was built to accept the external magnet frame and a field clamp to reduce the stray field in the region of the einzel lens. The nipple was inserted between the electron gun assembly and the vacuum chamber. The steel exhibited some magnetic hysteresis as expected but an automated routine to eliminate the hysteresis was easily developed. The beam spot can be placed anywhere at the target distance within a 50 mm radius with 0.1 mm precision and repeatability.

The cold nitrogen vapor cooling system has been replaced by a CryoMech PT-60 pulse tube cryorefrigerator.[5] We purchased a cryorefrigerator with a 60 W rating at 80 K for cooling the final detector assembly and pre-amplifiers for test here and at KATRIN. A new top flange for the vacuum chamber has been designed and built to accommodate the cooler, an extractable detector mount, and 6 general purpose feed thru ports. The cooler was tested with no thermal load. The temperature of the cold head was measured with an E-type chromel-constantan thermocouple. The cold head reached $-200°$ C (73 K) within 5 minutes of turn on. Short copper braid flex couplings have been designed to transfer heat from the detector and electronics assembly to the cryorefrigerator and allow easy servicing. Tests are planned for an array of 5, 10-mm square PIN diodes as well as tests for the final KATRIN detector.

After 15000 hours of intermittent use, the bearings of the turbo molecular pump in the dry pumping station failed. The pump core was exchanged for a new pump which has been installed and tested.

[5] CryoMech, Syracuse, NY

1.14 Radial dependence of KATRIN's energy resolution

J. A. Dunmore and R. G. H. Robertson

The exceptional sensitivity of the KATRIN neutrino mass measurement is due to the power of the MAC-E Filter. The resolution is defined by $\Delta E/E = B_{min}/B_{max}$, where B_{min} and B_{max} are the minimum and maximum values of the magnetic field experienced by the electrons emitted from the tritium source. B_{max} occurs at a pinch magnet placed near the detector and B_{min} occurs in the *analyzing plane*, where the electrons must overcome a specified potential to pass through the spectrometer to the focal plane detector.

The transmission function represents the fraction of electrons transmitted through the spectrometer as a function of electron energy above an applied retarding potential $(E - qU)$. In addition to B_{min} and B_{max}, the transmission function depends on the magnetic field strength at the source, B_s. The ratio of B_s to B_{max} defines the maximum angle by which electrons may be emitted from the tritium source. Because of this angle, the transmission function has a width equal to ΔE, since electrons emitted at larger angles will have significant transverse energy. At the analyzing plane, only electrons with longitudinal energy greater than qU will be transmitted. An idealized transmission function is shown in Fig. 1.14-1.

For the nominal magnetic field strengths of B_{min} = 3.0 G and B_{max} = 6.0 T, ΔE is 0.93 eV at 18.575 keV. This energy resolution, however, assumes constant magnetic field and retarding potential in the analyzing plane. Over its large radius (4.5 m) there will be inhomogeneities in these fields. A simulation was written to determine the effect of the expected inhomogeneities on the resolution ΔE. The left-hand plot shows the broadening of the transmission function due to each of the inhomogeneities.

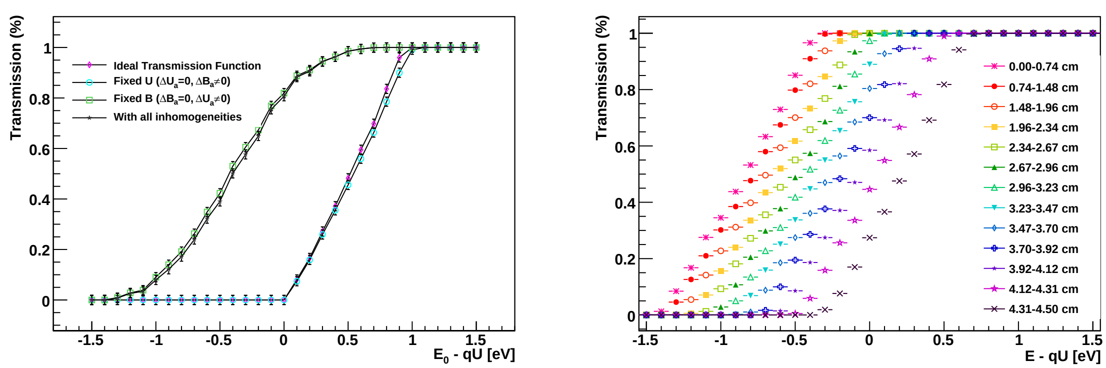

Figure 1.14-1. [Left] Effects of radial variation in magnetic field strength and retarding potential on the transmission function. [Right] Transmission function for each pixel.

The focal plane detector is divided into 148 pixels which, although maintaining the same area, decrease in width as they go further out in radius. This helps to reduce the effect of the inhomogeneities, since the fields (particularly the retarding potential) vary the most at large radii. The plot on the right shows the transmission function for each pixel. Broadenings of the resolution were determined for each pixel. The largest effect occurs in the outermost channels, where the resolution is broadened by 0.057 eV.

1.15 Monte Carlo Studies of low energy electrons incident on silicon

H. Bichsel, Z. Chaoui,* R. G. H. Robertson, and B. L. Wall

The signal-to-background in the end point measurement of the beta decay spectrum in KATRIN is associated with the backscattering of low energy electrons. The amount of backscattered electrons determines to a large extent the overall efficiency of the detector section. There exist few experimental results in the energy region of electrons, and a Monte Carlo would be the best solution to understand keV electron backscattering. It was decided to collaborate with Bichsel and Chaoui to develop a Monte Carlo to determine the energy spectrum and angular distribution of the backscattered electrons.

The endpoint energy of tritium beta decay is 18.6 keV, which defines the lower limit of incident energy in the KATRIN experiment. The upper limit of incident energies is determined by the amount of post acceleration. This will most likely be between 20 to 30 keV, meaning that KATRIN must understand the backscatter spectrum from 18.6 keV to 50 keV. The incident angular distribution is determined by the ratio of the magnetic field of the source magnet and the pinch magnet. The maximum angle will be less than 60 degrees.

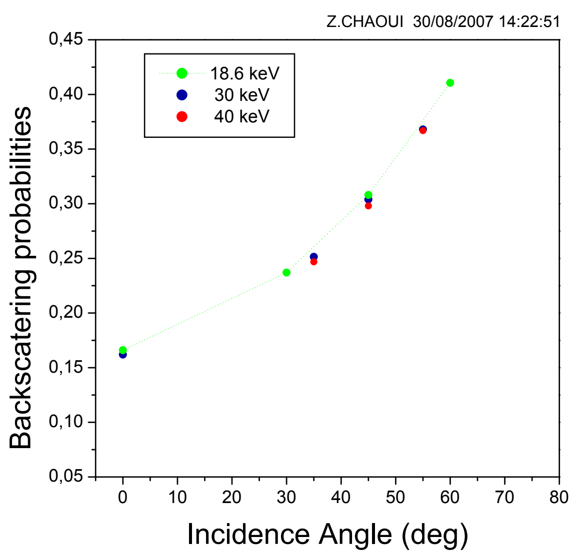

(a)

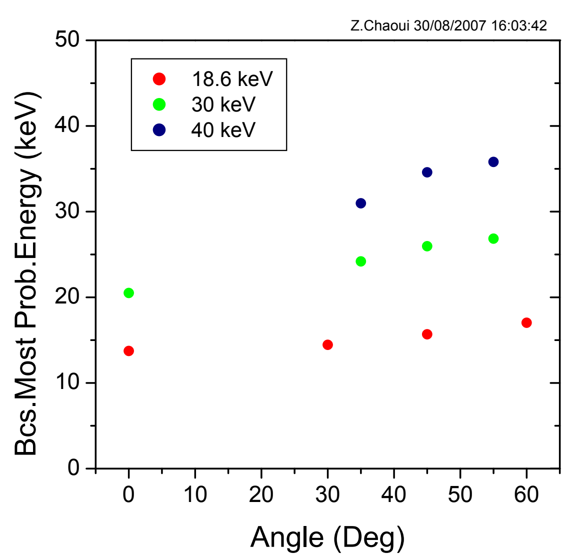

(b)

Figure 1.15-1. (a) Electron backscattering probability versus incidence angle. (b) Most probable energies of backscattered electrons as function of the angle of incidence.

The results of the Monte Carlo studies showed that there was a large dependence on the incident angle of the backscattering probability (Fig. 1.15-1 (a)). Also, there is much smaller dependence of the backscatter probability on the incident energy. Finally, most backscattered electrons leave with most of their incident energy(Fig. 1.15-1 (b)).

*University of Setif, Algeria

Majorana

1.16 Majorana R&D Activities

J. F. Amsbaugh, T. H. Burritt, P. J. Doe, J. A. Dunmore, A. García, M. A. Howe, R. A. Johnson, M. G. Marino, A. W. Myers, R. G. H. Robertson, A. G. Schubert T. D. Van Wechel, B. A. VanDevender, J. F. Wilkerson, and D. I. Will

The Majorana Collaboration is performing R&D to demonstrate the feasibility of building a 1-tonne modular array of 86% enriched ^{76}Ge capable of searching for neutrinoless double-beta ($0\nu\beta\beta$) decay in the inverted mass hierarchy region ($\sim$ 30 meV). A cornerstone of the plan is the development and construction of the Majorana Demonstrator, a R&D module comprised of 30 kg of 86% enriched ^{76}Ge and 30 kg of non-enriched Ge detectors. The use of a mixture of both enriched and natural or depleted Ge, has the advantages of lowering the costs in the R&D phase, accelerating the deployment schedule, and also giving Majorana an opportunity to verify that any observed peak in the $0\nu\beta\beta$ region of interest is directly associated with the presence of ^{76}Ge. The goals for the Demonstrator are:

- Show that backgrounds, at or below 1 count/ton/year in the $0\nu\beta\beta$ - decay peak 4-keV region of interest, can be achieved, a necessary condition for scaling up to a 1 tonne or larger mass detector.
- Demonstrate sensitivity by testing the validity of the Klapdor-Kleingrothaus reported ^{76}Ge $0\nu\beta\beta$ observation.[1]
- Show successful long-term operation of crystals in their respective environments.
- Demonstrate a cost-effective and scalable approach.

The proposed method uses the well-established technique of searching for $0\nu\beta\beta$ in high-purity Ge (HPGe) diode radiation detectors that play both roles of source and detector. These detectors will be located in specially fabricated ultra low-background, electroformed Cu cryostats. The technique is augmented with recent improvements in signal processing, detector design, and advances in controlling intrinsic and external backgrounds. Since detector fabrication is a critical issue for performance, cost, and schedule of a 1-ton detector, a number of alternative detector technologies including both p-type and n-type diodes will be examined in the R&D phase.

Highlights of local CENPA Majorana activities follow. In many of these areas our graduate students, postdocs, staff, and faculty are involved in collaborative efforts with researchers from other Majorana institutions.

[1] H. V. Klapdor-Kleingrothaus, I. V. Krivosheina, A. Dietz, and O. Chkvorets, Physics Letters B **586**, 198 (2004).

1.17 Sample preparations for the investigation of ultra-radiopure materials

T. H. Burritt, P. J. Doe, J. A. Dunmore, A. W. Myers, R. G. H. Robertson,
A. G. Schubert, J. F. Wilkerson, and D. I. Will

The clean room located in the basement of the Physics and Astronomy Building, room B037 is being used for the preparation of samples which will be tested for extraordinarily low levels of natural radioactivity. Samples will be prepared for gamma-counting, neutron activation analysis (NAA), and inductively coupled plasma mass spectrometry (ICP-MS). Procedures are being established for the packaging of powders, metals, and plastics for the various types of measurements.

The clean room has been surveyed and determined to be running at about class 30 (maximum of 30 particles of size ≥ 0.5 μm per cubic foot) at the area reserved for sample preparations. Plans have been made to replace HEPA filter units and to install a ductless fume hood. The deionized water system is operating with a resistivity of 17.6 MΩ-cm, and the pre-filter system and four filters will be upgraded so that it will operate at > 18 MΩ-cm.

A sample of Rexolite®[1] was machined into a cylinder with 4"-diameter and 6"-length. It was then cleaned using baths of acetone (to remove machining oil), isopropylene, and deionized water. The 1.3 kg sample was double-bagged in nylon lay-flat tubing and transferred to CENPA for gamma-counting using the surface material-screening facility (see Sec. 1.18). The outer bag was removed and the sample was counted for eight days. No significant signal was found due to ^{208}Tl (^{232}Th daughter). There was a significant signal of ^{214}Bi (^{238}U daughter), but the signal had a time variation, indicating that radon gas had drifted through the system.

Pogo pins and pogo pin adaptors, planned for use in KATRIN are ready be cleaned with alcohol, dried, double-bagged in nylon lay-flat tubing, and shipped to Lawrence Berkeley National Lab for counting.

For Majorana, we would like to obtain NAA measurements of the raw material for certain plastics. To handle and contain these powders, only the highest-purity plastic (no glass or metal) tools and containers may be used and must be leached prior to use. Leaching will be done with a nitric acid solution once the deionized water system is running at the necessary level of > 18 MΩ-cm.

We have been investigating the polymer, parlyene, for use in making flexible low-mass cables for Majorana. Powder samples of parylene dimer were obtained and will be prepared to make one large sample for gamma-counting and a number of smaller samples (> 10 g) for NAA at North Carolina State University and University of California, Davis. On-going test preparations of the small samples in 8-ml polyethylene vials have been performed outside the clean room.

[1] Rexolite® is a plastic made by C-Lec Plastics. www.rexolite.com

1.18 Material screening with germanium detectors

J. F. Amsbaugh, P. J. Doe, J. A. Dunmore, R. A. Johnson, M. G. Marino, A. G. Schubert, J. F. Wilkerson, and D. I. Will

The MAJORANA neutrinoless double-beta decay experiment[1] will require extremely low background rates. Materials used in the experiment must meet very high radiopurity standards to achieve MAJORANA background goals. Assaying raw materials at the sensitivity required for Majorana is costly and time consuming. A surface material-screening facility has been established at CENPA to prescreen materials for MAJORANA.

The material-screening facility consists of two high-purity germanium detectors enclosed in a six-inch-thick lead shield. The background spectra in the two detectors are shown in Fig. 1.18-1. A MaGe[2] simulation of the screening facility is available so that detected signals can be translated into estimates of sample activity. The facility allows materials that are not clean enough for MAJORANA to be identified without sending them to higher-sensitivity facilities.

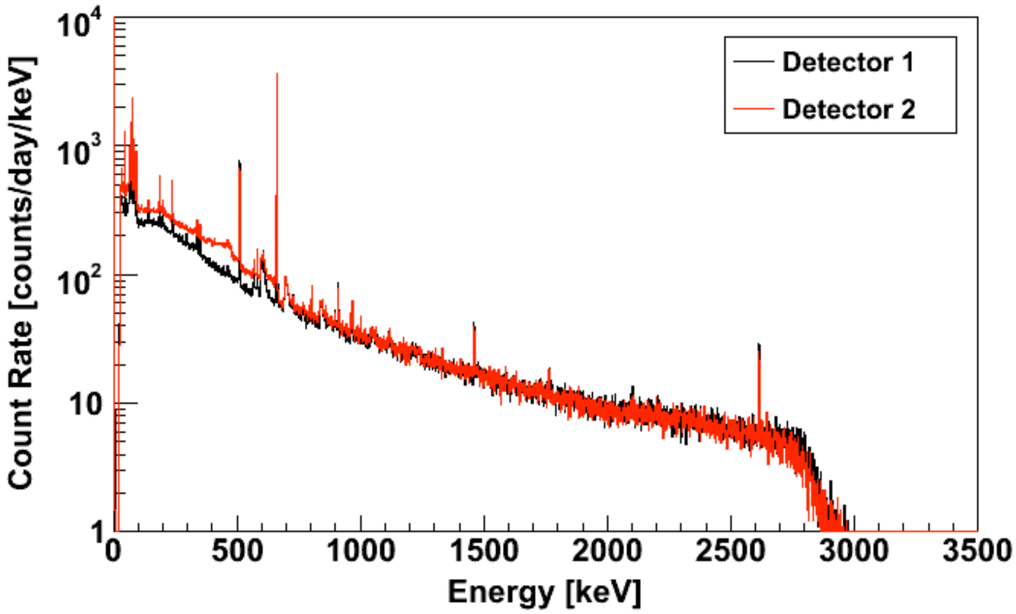

Figure 1.18-1. An eight-day background spectrum collected with the two detectors in the counting facility. Detector 2 has a higher low-energy continuum because it has a higher ^{137}Cs peak.

[1] C.E. Aalseth *et al.*, Phys. Atom. Nucl. **67**, 2002 (2004).
[2] M. Bauer *et al.*, J. Phys. Conf. Ser. **39**, 362 (2006).

1.19 A test stand for surface-alpha measurements on HPGe detectors

R. A. Johnson, T. H. Burritt, S. R. Elliott,* V. M. Gehman,* V. E. Guiseppe,* and J. F. Wilkerson.

Work has begun on the design and construction of a test stand for studying the effects of surface-alpha activity on hyper-pure germanium (HPGe) detectors. Alpha-decays of radioactive isotopes on or near the surfaces of HPGe detectors constitute a background for extremely-low background experiments like those searching for neutrinoless double-beta decay and dark matter. N-type HPGe detectors are particularly susceptible because of their thin ($\sim 0.3\mu$m) outer dead layer. It is for this reason that our test stand will consist of an n-type detector. This Surface Alpha N-Type Analysis (SANTA) will consist of a modified ORTEC Pop-Top n-type HPGe detector. The detector will be modified to hold a windowless α source next to the outer surface of the crystal.

Electric field lines at the surface of a biased HPGe detector are not uniform. The goal for SANTA will be to map out the detector's response as a function of surface location using a collimated α source over the surface of a detector at various angles of incidence. Of particular interest is the surface of the detector dividing the electrodes, the passivated surface. Field lines here are poorly understood, and there is the possibility of incomplete charge collection.

The initial stage of SANTA, allowing an α source to shine on the front end of the HPGe crystal, has been machined and is ready for installation (Fig. 1.19-1). This replaces the outer can on the original detector. The new outer can has a rotational feedthru with an α-source holder attached on the vacuum end. The top cover of the inner-crystal mount (currently mylar) will be replaced with an aluminum cap with collimation holes of differing sizes and angles, allowing selective access of α particles from the source to the front end of the detector. The rotational feedthru allows changing the placement of the α source above the different collimation holes without having to open the detector. This stage will be installed shortly. Future upgrades will include the ability to scan the sides of the HPGe crystal and also the bottom (passivated) surface.

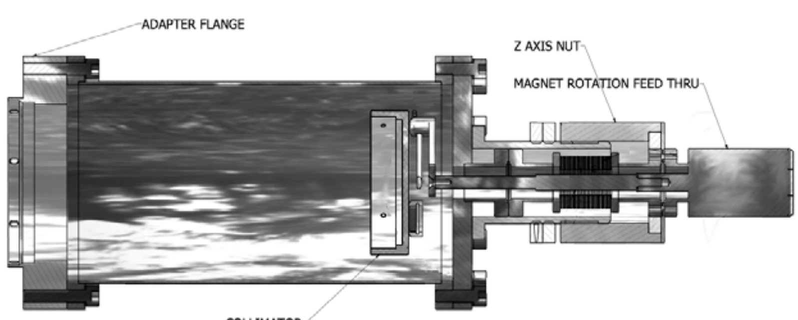

Figure 1.19-1. Side-view of new Surface Alpha N-Type Analysis outer can (rotated 90°). The rotational feedthru connects to an α-source holder. The source can then be swept above collimation holes through the collimator plate.

*Los Alamos National Laboratory, Los Alamos, NM

1.20 A time-coincidence analysis of surface-alpha activity on an n-type HPGe detector

R. A. Johnson, S. R. Elliott,* V. M. Gehman,* V. E. Guiseppe,* and J. F. Wilkerson.

The WIPP-n detector is an n-type HPGe detector, currently situated at the Waste Isolation Pilot Plant (WIPP), 2150 feet below ground near Carlsbad, NM. This detector is used primarily as a screening / counting detector in a low-background, underground setting. The thin, outer dead layer of this n-type detector also makes it a good candidate for studies of surface α backgrounds. The counts above the 2.6 MeV peak (^{208}Tl) are likely either from α decays from the ^{232}Th and ^{238}U chains, or else events originating from cosmic rays. Certain α decays from the U and Th chains occur within characteristic times (see Table 1.20-1). A time-coincidence analysis was used to attempt to quantify the amount of U/Th near the surface of the detector. A time cut was applied to the events in the data set such that if two or more events occur within a given time period and satisfy a minimum energy, then they are counted as potential coincident pairs. There is also a possible triple coincidence from the decays ^{224}Ra$\rightarrow^{220}$Rn$\rightarrow^{216}$Po$\rightarrow^{212}$Pb.

α Decay	Decay Half-Life
^{218}Po$\rightarrow^{214}$Pb	186 s
^{214}Po$\rightarrow^{210}$Pb	164 μs
^{220}Rn$\rightarrow^{216}$Po	55.6 s
^{216}Po$\rightarrow^{212}$Pb	145 ms

Table 1.20-1. Short-lived daughters from the U and Th decay chains that are useful for time coincidence studies of α decays.

The dataset used represented 30.86 days of livetime. To reduce accidentals resulting from the 3 event per minute rate, only events satisfying a minimum energy cut and occurring within a window of 111.2 s (twice the half-life of the ^{220}Rn decay) were considered. Accidental coincidences were computed from the singles rate. Results are shown in table Table 1.20-2. This initial analysis shows no evidence of coincident α decays characteristic of the ^{238}U/^{232}Th decay chains. A future analysis will look for $\alpha/\beta/\gamma$ coincidences.

Time Window [s]	Min. Energy Threshold	Number of Coincidences	Expected Accidentals
Doubles			
0.3	1 MeV	2	1.9
111.2	1 MeV	739	722.3
0.3	2.65 MeV	0	1.5×10^{-2}
111.2	2.65 MeV	6	5.7
Triples			
111.2 & 0.3	1 MeV	0	0.35
111.2 & 0.3	2.65 MeV	0	2.4×10^{-4}

Table 1.20-2. Coincidence results from the time-correlation analysis.

*Los Alamos National Laboratory, Los Alamos, NM

1.21 Methods for deploying ultra-clean detectors

T. H. Burritt, M. Howe, R. A. Johnson, M. G. Marino, A. G. Schubert, J. F Wilkerson, S. R. Elliott,* V. M. Gehman,* and V. E. Guiseppe*

The MAJORANA Collaboration will use an array of germanium crystals enriched in ^{76}Ge to search for neutrinoless double-beta decay. The Ge crystals will be housed in radiologically-pure copper cryostats. Several vertical strings of three to four Ge crystals will be deployed in each cryostat. A test cryostat for the MAJORANA experiment has been assembled at Los Alamos National Laboratory. The test cryostat can accommodate three test strings, where each string has a three-detector capacity. The cryostat was built to test electrical and mechanical designs for the Majorana project.

To test the thermal performance of the MAJORANA design, temperature sensors were installed at various locations within the test cryostat. Temperature sensors were also attached to two stainless-steel detector blanks that were deployed into the cryostat. The blanks approximated the geometry, thermal mass, and emissivity of Ge detectors. After cooling the system with liquid nitrogen, it was determined that the cryostat would cool Ge detectors to suitable operating temperatures.

To test the electrical properties of the string design, a retired p-type Ge detector with modest energy resolution, 1.5% at 1333 keV, was removed from its commercial cryostat and deployed in a detector string in the test cryostat. A photograph of the detector and a ^{60}Co energy spectrum collected with the detector appear in Fig. 1.21-1. The detector's resolution was not affected by moving it into the test cryostat.

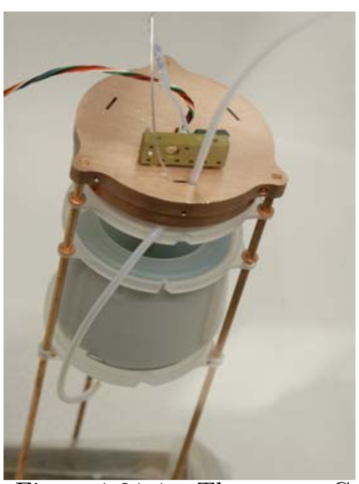

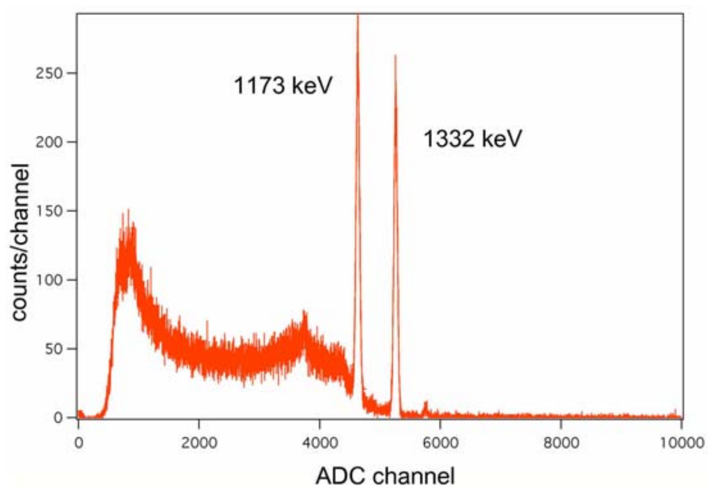

Figure 1.21-1. The p-type Ge detector mounted in a detector string before deployment into the cryostat (left). A ^{60}Co spectrum collected with a detector in the test cryostat (right). The energies of two ^{60}Co peaks are labeled.

*Los Alamos National Laboratory, Los Alamos, NM

1.22 Testing of fast digitizers for the MAJORANA experiment

M. A. Howe, M. G. Marino, and J. F. Wilkerson

Fast analog-to-digital converters (ADCs) can be used to digitize pulses from the preamp of a germanium detector. Digitization of pulses enables later software analysis for the extraction of parameters (e.g. energy and timing) and for the determination of event topology (e.g. multi-site vs. single-site events). Work has progressed to determine digitization needs for the MAJORANA neutrinoless double-beta decay experiment. Several digitizers have been tested and compared (see Table 1.22-1).[1]

	Gretina Mark IV	Gretina Mark I	XIA DGF-4c
Channels	10	8	4
Freq (MS/s)	100	100	40
Readout	(32-bit) DMA, BLT	(32-bit) DMA, non-incrementing	CAMAC (16-bit)
Resolution (Bits)	14	12	14
FIFO (KB)	∼524	∼64	∼64

Table 1.22-1. The Gretina cards are VME-based modules; XIA card is CAMAC based. DMA: Direct Memory Access. BLT: BLock Transfer.

A number of tests have been performed including speed and linearity tests. Results from speed tests performed using ORCA and the newly implemented SBC (see Sec. 6.3) with the Gretina digitizer cards are presented in Fig. 1.22-1.

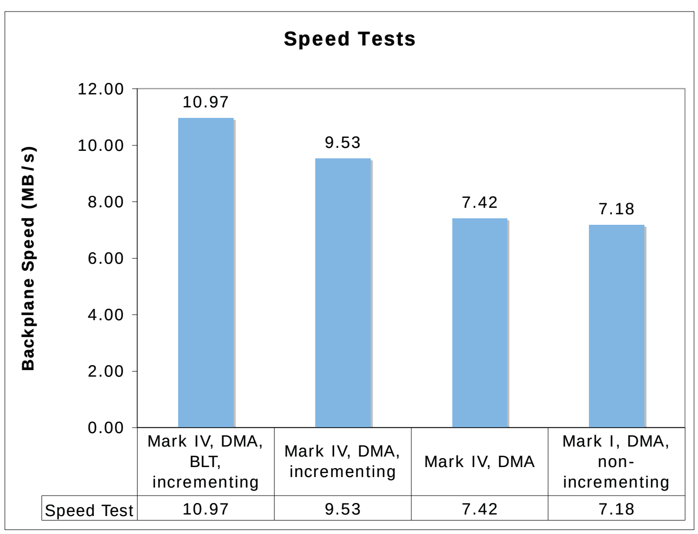

Figure 1.22-1. Speed tests performed with the Gretina Digitizer cards.

To aid in the determination of digitizer needs for the MAJORANA experiment, software has been developed to simulate the digitization of generated pulses. This software enables the testing of "virtual" digitizers with different parameters (e.g. resolution, digitization speeds).

[1]The Gretina cards are on loan from the Gretina group at Lawrence Berkeley National Laboratory.

2 Fundamental Symmetries and Weak Interactions

Torsion Balance Experiments

2.1 Progress report on the wedge pendulum test of the gravitational inverse-square Law

E. G. Adelberger, T. S. Cook, and H. E. Swanson

As reported last year,[1] the primary hurdles for the Wedge Pendulum have been understanding and utilizing new technologies. Now the hurdles appear to be behind us as we are currently readying the system for scientific data.

The most time consuming effort has been toward building a precision, servo-controlled rotary drive to turn the attractor. After discovering our Nanomotion HR1 Ultra-High-Vacuum motor was incapable of continuous operation in a vacuum environment (due to heat management issues), we were forced to redesign the system such that the motor remained in atmosphere. We are pleased with the final performance. Fig. 2.1-1A

Although the motor is outside the vacuum, a once per revolution temperature modulation (presumably, due to radial run-out of the ceramic disk) is noticeable on in-vacuum temperature sensors. Therefore, it was also necessary to design a PID-controlled peltier element mounted to the motor body to adequately manage the problem.

Finally, we mounted the pendulum and attractor foils using Dow Integral E100 adhesive film. The final mount was suitably flat, Fig. 2.1-1B, but there were some inconsistencies with how the glue behaved in the gap regions of the wedges; there are crater like voids in a small percentage of the exposed areas of glue. We determined that these could be adequately modeled and have moved forward to taking data.

[1] CENPA Annual Report, University of Washington (2007) p. 41.

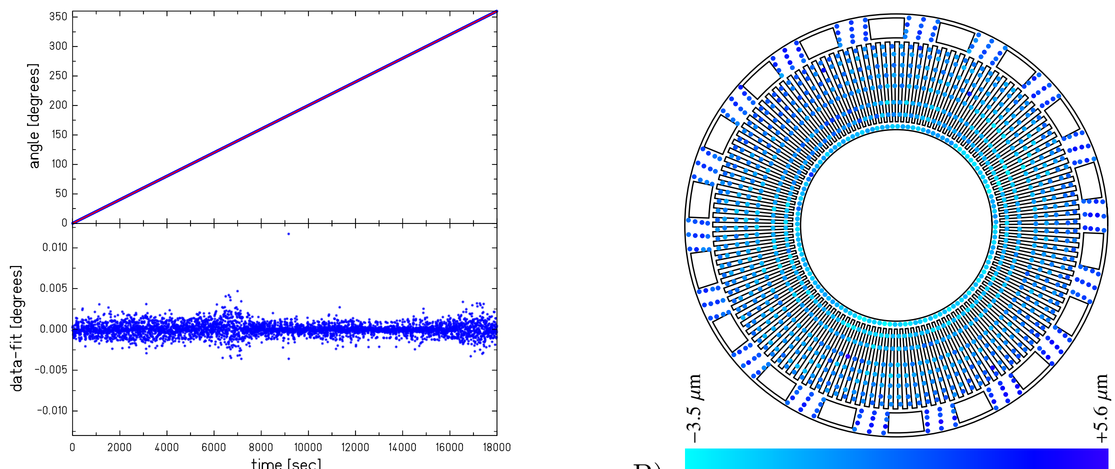

A) B)

Figure 2.1-1. A) Angle readout from attractor encoder. Each point represents a 4 second average, sub-sampled at 50Hz. The standard deviation is less than 0.0009 degrees. B) Surface measurements of mounted foil. Each dot represents a hit of the coordinate measuring machine, with the color (color online) indicating deviation from the best fit plane. The standard deviation is less than 1.6μm.

2.2 First results from the "axion" torsion-balance experiment

E. G. Adelberger, F. Fleischer, B. R. Heckel, and S. A. Hoedl

Our torsion pendulum search for an axion-like particle offers a significant improvement over the most recent such measurement.[1] The axion is the result of the hypothesized Peccei-Quinn symmetry and is a favored cold dark matter candidate. Its mass is constrained by the known flat geometry of the universe to be heavier than 1 μeV, and is constrained by the neutrino flux from SN1987A to be lighter than 10000 μeV.[2] Note that microwave cavity searches probe for light axions ($m_a \sim 1\mu$eV) and have sufficient sensitivity to see the expected cosmological axion flux.[3] A torsion-pendulum based search is possible because the axion mediates a macroscopic pseudo-scalar potential ($\propto \Theta_{QCD}$) between polarized and unpolarized fermions. By observing the motion of a planar torsion pendulum (source of unpolarized fermions) positioned near the pole faces of an energized ferromagnet, we can observe such a force.

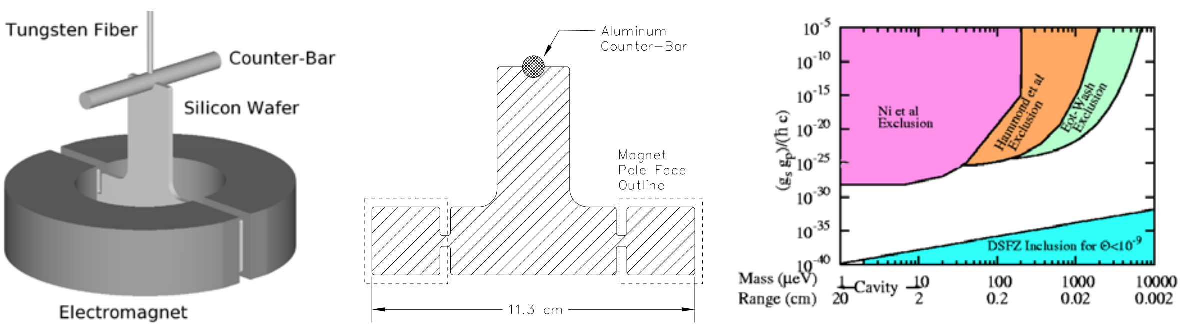

Figure 2.2-1. A scale diagram of one of our pendulums positioned in between the magnet pole faces; A face-on view of the pendulum; Our exclusion bounds compared with recent experimental searches and the expected coupling for $\Theta_{QCD} < 10^{-9}$.

In the past year, we have identified the residual magnetization of the magnet iron as the dominant systematic error of the experiment. We have minimized the effects of this residual magnetization by carefully investigating the proper degauss procedure. We also carefully control the magnet current so that the magnetic field is changed in a slow and repeatable manner. However, a small torque is observed and is being explored. Within the sensitivity of the apparatus, this torque does not depend on the pendulum position, as it should if the torque were due to a new axion-like particle. In this manner, we can constrain a new short-range force despite the effects of residual magnetization. At present, the apparatus puts a limit on a macroscopic parity and time violating force which is 100 trillion times more restrictive than Hammond *et al.*[1] for an axion mass of 2 meV, although this is not sensitive to conventional axion models. We expect these results will be submitted for first publication no later than July 31, 2008.

[1] G. D. Hammond *et al.*, Phys. Rev. Lett. **98**, 081101 (2007).

[2] G. Raffelt hep-ph/0611350.

[3] L. D. Duffy *et al.*, Phys. Rev. D **74**, 012006 (2006).

2.3 New results from a spin-polarized torsion balance

E. G. Adelberger, C. E. Cramer, and B. R. Heckel

The extraordinary sensitivity of the torsion balance instrument has made it a valuable tool to test symmetries in nature and to search for new weak macroscopic forces. There are several reasons to perform torsion balance measurements with a spin polarized test body: to perform a precise test of Lorentz and CPT invariance, to search for new forces mediated by pseudoscalar bosons, and to help elucidate the role of spin in gravitation.

Our group at the University of Washington has constructed a spin polarized test body that contains 9.8×10^{22} polarized electrons, with negligible magnetic moment. The polarized test body was mounted with the spin dipole horizontal in our original Eöt-Wash II torsion balance, which rotates about a vertical axis at a constant rate. The angular read-out of the balance provides a measure of the orientation of the spin pendulum that corresponds to an energy minimum, *i.e.* the horizontal direction along which the polarized electrons prefer to point.

Because the magnetic moment of the spin pendulum vanishes, the pendulum has a net angular momentum that is equal and opposite to the spin angular momentum: $\vec{J} = -\vec{S}$. For $\vec{J}$ to remain constant in the frame of the rotating earth, the torsion fiber has to apply a steady torque given by $(\Omega \times \vec{J}) \cdot \hat{n}$, where Ω is the sidereal rotation frequency of the earth and $\hat{n}$ is local vertical. We have measured this "gyro-compass" torque that acts on the spin pendulum and can use the measurement to calibrate the number of polarized electrons, N_p, in the pendulum. We find $N_p = (9.80 \pm 0.27) \times 10^{22}$.

We have used our spin-polarized torsion balance to search for CP-violating interactions between the pendulum's electrons and unpolarized matter in the earth or the sun and to test for rotation and boost-dependent preferred-frame effects using the earth's rotation and velocity with respect to the entire cosmos. Our first results were reported in 2006.[1] Newer results will be presented in a review paper that is nearing completion.

We find that for a preferred-frame coupling to electron spins of the form:

$$V = -\vec{\sigma} \cdot \vec{A} \quad \text{our result is} \quad |A_{x,y}| < 2 \times 10^{-22}\text{eV}$$

where $\vec{\sigma}$ is the electron spin and the torsion fiber is along the z axis.

For a CP-violating interaction mediated by the exchange of a mixed scalar-pseudoscalar particle:

$$V(r) = g_P g_S \frac{\hbar}{8\pi m_e c} \vec{\sigma} \cdot \vec{\nabla}\Big(\frac{e^{-r/\lambda}}{r}\Big)$$

we find $|g_P g_S|/\hbar c < 9.4 \times 10^{-37}$ for $\lambda > 1$ AU.

Spin sources have been constructed with 10^{25} polarized electrons. The spin pendulum apparatus is currently taking data with the local spin sources to search for new weak spin-spin interactions.

[1] B. R. Heckel *et al.*, Phys. Rev. Lett. **97**, 021603 (2006).

2.4 A new short-range spin-spin experiment

E. G. Adelberger, B. R. Heckel, and W. Terrano

We have begun building a new torsion pendulum to study spin-spin interactions between test bodies with polarized electron spin. This pendulum, a ring consisting of alternating high (Alnico) and low (SmCo5) spin density segments, is designed to operate at shorter separations than previous experiments.[1]

The mechanical and magnetic properties of the two materials led us to adopt the following assembly process. The permanent SmCo5 magnets were wire EDM burned to shape from a single block after having been magnetized to an internal magnetization of nearly 10,000 Gauss. This allowed the greatest possible uniformity in the magnetizations of the individual SmCo5 pieces. The soft Alnico magnets were cut unmagnetized. We then assembled a prototype ring and magnetized the Alnico pieces in place so that the Alnico would adopt the magnetizations needed to minimize leakage fields. The prototype has also been used to begin designing the magnetic shielding needed to operate at short distances.

We have designed and machined the fixture for the attractor ring: it consists of a twenty sided central post to align the twenty trapezoidal magnets. Directly above and below the magnet ring is an annulus of .010" Conetic as a flux return for the leakage fields. Alnico is less dense than SmCo5, so we will place tantalum leaves above and below the Alnico segments (outside the Conetic ring). In order to assure the compensation plates are aligned with the Alnico, the exterior plates holding the attractor plates from above and below will be registered to the central post, and will have insets for the tantalum foil. Fig. 2.4-1

One important test for systematics is to flip the attractor ring upside down: this will invert the direction of the attractor's spin field while leaving the gravitational signal unchanged. As long as we know the phase of the attractor relative to the pendulum before and after the flip, we can distinguish the two signals. Therefore, we will have four tungsten rods in both the pendulum and the attractor. Looking at this 4-omega signal will allow us to determine the relative phase of the 10-omega gravity and spin signals.

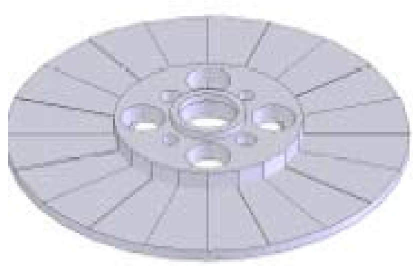

Figure 2.4-1. Drawing of the bottom half of the attractor fixture. The gravity compensation plates sit in the milled out insets on the plate, then the magnets go on top of those, around the central post. A matching piece is then placed over this and screwed down.

[1]CENPA Annual Report, University of Washington (2007) p. 38.

2.5 Progress toward a new sub-millimeter test of the gravitational inverse square law

S. J. Caley, P. Emani, J. H. Gundlach, C. A. Hagedorn, K. K. Krause, S. E. Pollack, S. Schlamminger, and M. D. Turner

We have constructed a new torsion balance for a parallel-plate test of the gravitational inverse square law.[1] Our apparatus is operational. The challenging work of achieving short range results awaits.

It was a constructive year. Our in-vacuum fiber translation and rotation stages have been mounted on a sturdy frame. An in-vacuum laser autocollimator allows us to monitor the deflection of our pendulum. A continuous gravitational torque calibration system has been constructed and installed. One attractor and three successively superior pendulums have been used in the apparatus. To separate the pendulum and attractor physically and electrically, we use a stretched gold coated aluminum membrane. Our measurement of the attractor's motion was improved with a simple optical readout. An in-vacuum encoder on a fiber translation stage has been installed. We will use a second one to corroborate our existing attractor readout. New electrical feedthroughs, PEEK in-vacuum breakout blocks, cabling, and electronics have largely separated signals related to our attractor and pendulum. To further separate the attractor from the pendulum, we have fabricated and installed an aluminum sheet metal wall. Our data acquisition and control software, developed in parallel with our LISA experiment, is installed and functional.

Figure 2.5-1. The pendulum and its reflection in the foil that isolates it from the attractor. The feedback electrodes are in the foreground.

We have achieved pendulum-attractor separations as small as 200 μm. Ongoing development of a simple and repeatable alignment procedure will allow us to reach shorter distances. In addition, dust accumulation on the critical surfaces of the experiment makes attaining short distances challenging. To combat dust, we have recently fabricated a clean room over the experiment.

The torsion balance itself functions well. We are able to hold the pendulum in electrostatic feedback at separations as small as 50 μm from the foil. We have achieved sufficiently low torque noise to complete our planned measurement.

[1] CENPA Annual Report, University of Washington (2007) p. 40.

2.6 Limits on weak equivalence principle violation using beryllium, titanium, and aluminum test bodies

E. G. Adelberger, J. H. Gundlach, S. Schlamminger, and T. A. Wagner

The equivalence principle is a fundamental assumption of general relativity and has withstood all tests to date. Yet while the empirical evidence for the equivalence principle is strong, there are many reasons to improve tests of it. The inability to quantize general relativity implies that there is some more fundamental theory of gravity. Gravity has yet to be combined with the standard model in a manner that does not violate the equivalence principle.[1] Many theoretical models predict the violation of the equivalence principle at a level just beyond current limits, including a dilaton-runaway scenario,[2] an anomalous coupling to the weak interaction,[3,4] supersymmetric theories,[5] and a time-dependent scalar field.[6] The weak equivalence principle is one of the most sensitive probes into possible new physics.[1] In our recent measurements we have improved limits on weak equivalence principle violations.

We used a rotating torsion balance to measure the differential acceleration between different composition test masses. The test masses were arranged in a dipole configuration on the pendulum and the entire apparatus was rotated, so that a signal would occur at the rotation frequency of the apparatus. We measured the difference in acceleration for beryllium and aluminum to the North, $\Delta a_{N,Be-Al} = (-2.6 \pm 2.5) \times 10^{-15}$ m/s^2 and to the West, $\Delta a_{W,Be-Al} = (0.7 \pm 2.5) \times 10^{-15}$ m/s^2. We also published our results for beryllium and titanium of $\Delta a_{N,Be-Ti} = (0.6 \pm 3.1) \times 10^{-15}$ m/s^2 to the North and $\Delta a_{W,Be-Ti} = (-2.5 \pm 3.5) \times 10^{-15}$ m/s^2 to the West.[7] Our new result for beryllium and aluminum constrains the parameter $\eta_{Be-Al} = \Delta a/a_{\perp} = (-1.6 \pm 1.5) \times 10^{-13}$, where $a_{\perp}$ is the horizontal gravitational attraction due to the earth.

Understanding and measuring systematic effects is important to the measurement. We found effects due to temperature variations, tilt of the apparatus, magnetic fields, and gravity gradients that could mimic an equivalence principle violating signal. We measured each effect by exaggerating it, e.g., we applied a large temperature gradient across the apparatus to measure temperature gradient effects. We correct for tilt misalignments and gravity gradients. Temperature effects are difficult to model accurately, so we do not correct for them. We summarize our results in Table 2.6-1.

By combining our weak equivalence principle results for beryllium and aluminum with our measurements for beryllium and titanium, we set better limits on forces due to charges that are a linear combination of baryon number and lepton number. The combination of

[1] T. Damour, Class. Quantum Grav. **13**, A33 (1996).

[2] T. Damour, F. Piazza, and G. Veneziano, Phys. Rev. D **66**, 046007 (2002).

[3] E. Fischbach, D. E. Krause, C. Talmadge, and D.'Tadic, Phys. Rev. D **52**, 5417 (1995).

[4] E. Fischbach, S. W. Howell, S. Karunatillake, D. E. Krause, R. Reifenberger, and M. West, Class. Quantum Grav. **18**, 2427 (2001).

[5] P. Fayet arXiv:hep-ph/0111282v1 (2001).

[6] G. Dvali and M. Zaldarriaga, Phys. Rev. Lett.**88**, 1303 (2002).

[7] S. Schlamminger, K.-Y. Choi, T.A. Wagner, J.H. Gundlach, and E.G. Adelberger, Phys. Rev. Lett. **100**, 041101 (2008).

differential acceleration in	$\Delta a_{N,Be-Al}$ (10^{-15} m/s^2)	$\Delta a_{W,Be-Al}$ (10^{-15} m/s^2)
as measured (statistical)	-3.2 $\pm$ 1.9	1.1 $\pm$ 1.9
magnetic	0.0 $\pm$ 0.4	0.0 $\pm$ 0.4
residual gravity gradients	0.0 $\pm$ 0.5	0.3 $\pm$ 0.6
temperature gradients	0.0 $\pm$ 1.2	0.0 $\pm$ 1.2
tilt	-0.6 $\pm$ 0.6	0.1 $\pm$ 0.7
corrected	-2.6 $\pm$ 2.5	0.7 $\pm$ 2.5

Table 2.6-1. The raw differential accelerations between Be and Al towards the North (N)and West (W) are shown in line 1. Lines 2 to 5 list corrections that were subtracted, and the bottom line gives our corrected results. Uncertainties are 1σ.

beryllium and titanium was selected for its sensitivity to baryon number as a charge, whereas the beryllium and aluminum combination has a better sensitivity to lepton number as a charge. We parameterize a possible interaction as V $= \alpha(\frac{q}{\mu})_1(\frac{q}{\mu})_2\frac{Gm_1m_2}{r_{12}}\ e^{-r_{12}/\lambda}$, where $\frac{q}{\mu}$ is the charge per atomic mass unit, G is Newton's constant, m is the mass, r_{12} is the range between the bodies, and λ is the effective range of the Yukawa potential. We analyzed our measurements with respect to different sources to set limits on the violation of the equivalence principle for ranges from one meter to infinity. We present limits on a ranged force with B-L as charge in Fig. 2.6-1.

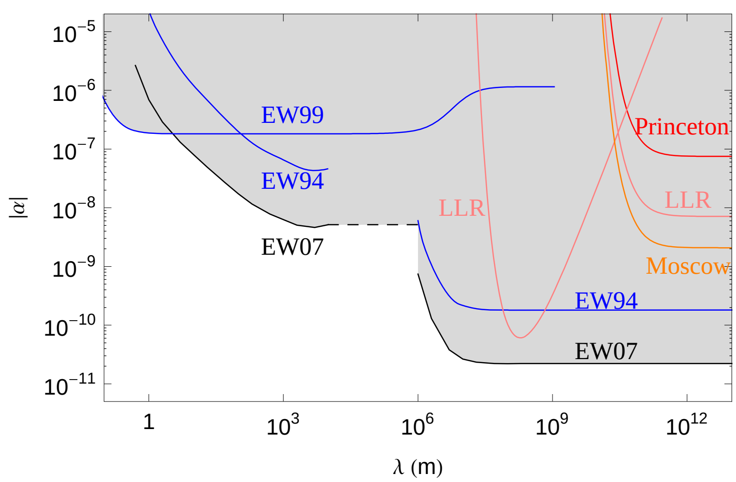

Figure 2.6-1. Limits on the strength, compared with gravity, of a ranged force with a charge of B-L.

The galaxy provides an additional interesting source, since approximately one quarter of the total acceleration of the solar system toward the center of the galaxy is caused by dark matter.[8] We resolve no difference in the acceleration due to dark matter as $\eta_{DM,Be-Al} = (-7\pm7)\times10^{-5}$ for beryllium and aluminum and as $\eta_{DM,Be-Ti} = (-4\pm7)\times10^{-5}$ for beryllium and titanium.

[8]G.L. Smith *et al.*, Phys. Rev. D **61**, 22001 (2000).

2.7 Improving equivalence principle limits for gravitational self-energy

E. G. Adelberger, J. H. Gundlach, B. R. Heckel, S. Schlamminger, and T. A. Wagner

Recent advances in lunar laser ranging promise to improve limits on the violation of the strong equivalence principle, which states that even gravitational energy obeys the equivalence principle. To unambiguously conclude that a strong equivalence principle violation due to the gravitational self-energy of the earth and moon is not masked by a weak equivalence principle violation due to differences in the earth's and moon's compositions, laboratory tests of the weak equivalence principle are required.[1] Using our existing rotating torsion balance, we are measuring the differential acceleration towards the sun of test bodies that model the earth's and moon's compositions. Since the size of our test bodies is roughly a few centimeters, they have no appreciable gravitational self-energy. The gravitational self-energy of the earth and moon reduces their masses by 4.6 and 0.2 parts in 10^{10}, respectively.

The lunar laser ranging improvements should allow tests of $\eta_{LLR} = \Delta a_{LLR}/a_s \sim 10^{-13}$, where $a_s = 5.93 \times 10^{-3}$ m/s^2 is the acceleration toward the sun.[2] The strong equivalence principle will be tested by comparing the lunar laser ranging result with our composition dependent result $\eta_{SEP} = (\Delta a_{LLR} - \Delta a_{CD})/a_s$. The earth's mantle has a similar composition to the moon, so we enhance our sensitivity by using test bodies with compositions similar to the earth's core and moon. We hope to improve our previous measurement[3] of the composition dependent part commensurate with the improvement in the lunar laser ranging limit.

An analysis of our expected uncertainties in Table 2.7-1 shows that we will primarily be limited by the statistical uncertainty of our measurement. The systematic uncertainties are estimated using the measured daily variation since this could produce a response of our torsion balance mimicking an equivalence principle violation. The uncertainty due to the daily variation of gravitational gradients that couple to our pendulum will likely be our largest systematic, with other sources having a relatively negligible impact.

uncertainty estimates for differential acceleration in	Δa_{CD} (10^{-16} m/s^2)
one-year estimated statistical	$\pm$ 2.1
magnetic	$\pm < 0.1$
residual gravity gradients	$\pm$ 0.7
temperature gradients	$\pm$0.2
tilt	$\pm$0.4
total	$\pm$ 2.3

Table 2.7-1. The estimated uncertainties for the differential acceleration towards the sun between test bodies with compositions similar to the earth and moon. Uncertainties are 1σ.

Thus we expect to limit $\eta_{CD} = \Delta a_{CD}/a_s \sim 10^{-13}$, which is comparable to the lunar laser ranging goal. Combining the results should give a test of the equivalence principle for gravitational self-energy of $\eta_{grav} < 5 \times 10^{-4}$.

[1] K. Nordtvedt, Phys. Rev. D **37**, 1070 (1988).
[2] Murphy *et al.*, arXiv:0710.0890v2 [astro-ph].
[3] S. Baessler, B. R. Heckel, E. G. Adelberger, J. H. Gundlach, U. Schmidt, and H. E. Swanson, Phys. Rev. Lett. **83**, 3585 (1999).

Weak Interactions

2.8 Parity non-conserving neutron spin rotation experiment

C. Bass,* K. Gan,† B. R. Heckel, D. Luo,‡ D. Markoff,§ A. Micherdzinska,¶
H. P. Mumm,* J. Nico,* A. Opper,† W. M. Snow‡ and H. E. Swanson

Installation of the cryogenic target on the NIST beam line was completed in November of 2007. As part of this installation we re-wound a damaged input spin transport coil and added two new coils to wash out any remaining transverse neutron polarization.

The target is divided into 4 approximately half meter long chambers. Two are upstream positioned in the neutron beam on its west and east sides and the other two are symmetrically downstream of the first set. Polarized neutrons scattering through the liquid helium in the chambers undergo rotations about their momentum axes from parity non-conservation in the weak interaction. Separating the upstream and downstream chambers is a Pi-coil which precesses the horizontal component of the rotated neutrons polarization by 180 degrees. This allows us to cancel much larger spin rotations from background axial magnetic fields in the target regions.

The data acquisition program NSAC was modified from controlling room temperature targets to control the pump and system of valves that alternately fill and drain the target chambers. While changing target configuration it reads out helium level and temperature sensors and displays them on a target status panel. It can also read 4 flux gate magnetometer probes mounted on the target chambers and from these values determine the currents required by a set of trim coils to null the measured fields. These trim coils are powered by computer controlled constant current sources built at CENPA.

Fig. 2.8-1 shows histograms of data taken during our first cycle of reactor operation. Those labeled E and W are differences in measured spin rotation angles between the two target configurations (full upstream and empty downstream vs. full downstream and empty upstream) on the east and west sides respectively. They are shown multiplied by 5 for clarity and in color on-line. The differences are nearly zero even though spin rotations from background magnetic fields are of the order of milli-radians. The widths of these histograms are dominated by fluctuations in the reactor's output. Also shown is a histogram of east minus west difference angles (our PNC signal). Here reactor fluctuations are common to both sides so the width of the histogram is dominated by the shot noise in detected neutrons.

Our need to add liquid helium to the target volume every 8 hours determines the operating

*NIST Center for Neutron Research, 100 Bureau Drive, Stop 8461, Gaithersburg, MD 20899-8461.
†The George Washington University, Department of Physics, Corcoran 105, 725 21st St, NW, Washington, DC 20052.
‡Department of Physics, Indiana University Cyclotron Facility, 2401 Milo B. Sampson Lane, Bloomington, IN 47408.
§Triangle Universities Nuclear Laboratory, Duke University, TUNL Building, Science Drive, Room 414, P.O. Box 90308, Durham, NC, 27708.
¶Postdoctoral Research Associate, University of Winnipeg, 515 Portage Avenue Winnipeg, MB R3B 2E9 CANADA

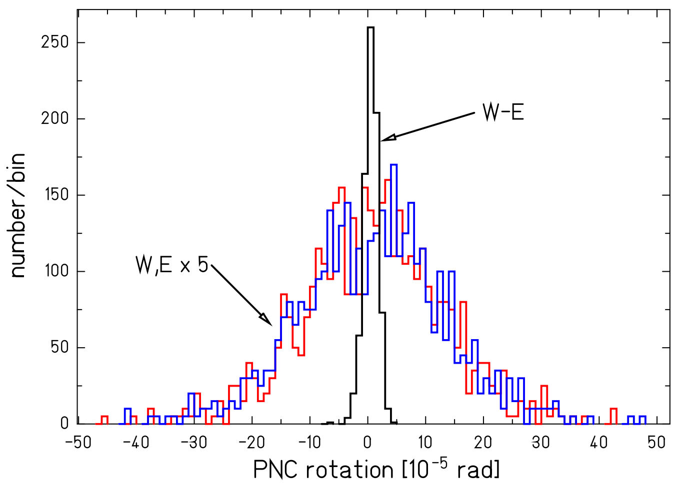

Figure 2.8-1. Data taken during the first reactor cycle after cool-down to liquid helium temperatures. Histograms show our PNC spin rotation signal from the East and West sides of the apparatus and the combined E-W signal.

schedule of three runs per 24 hour period. Each reactor cycle corresponds to about 20 days of beam time and 10 days when it is shut down. When running, half the time is spent changing the target configuration and half is spent acquiring data. We have currently completed two reactor cycles and our resulting statistical error on the spin rotation angle is about 9 x 10^{-7} radians/meter. We plan on running one more cycle before completing this experiment at NIST.

The super mirror polarizer-analyzer pair gives the neutrons a vertical polarization with a polarization product of 0.75. Since the Pi-coil causes some depolarization due to the spread in neutron velocities the effective polarization product is only 0.6. We determine this periodically throughout the measurement.

The background axial magnetic field in the target region is typically about 100 microGauss. This is associated with a potential systematic contribution to the PNC spin rotation. We applied a 10 milliGauss axial field to amplify any systematic contribution and determined this contribution to be less than 0.8 x 10^{-7} radians/meter.

2.9 Progress toward determination of the beta asymmetry from neutron decay

A. García, S. Hoedl, A. L. Sallaska, S. K. L. Sjue, and UCNA collaboration*

Ultra-Cold Neutrons (UCN) provide an excellent opportunity to determine the correlation parameters of β decay: they are simple to polarize and, in principle, could yield the most accurate determinations of the β asymmetry. During the past five years we have been working as members of the UCNA collaboration at Los Alamos to produce enough UCNs to extract the β asymmetry.

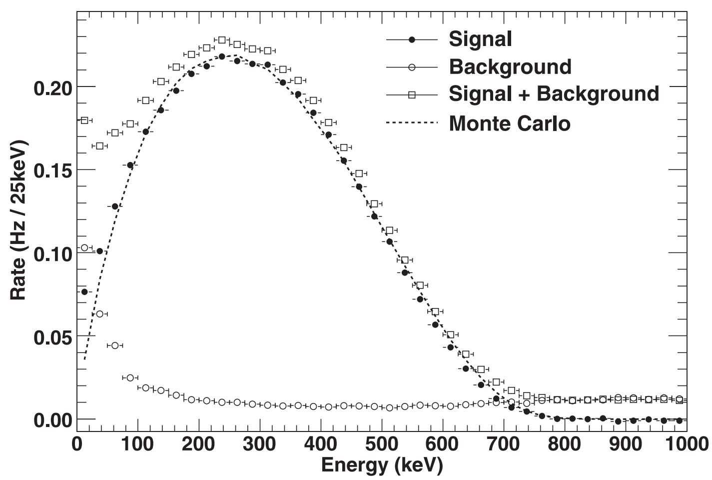

Figure 2.9-1. Beta spectrum taken at the end of 2007 at Los Alamos in one of our detectors.

At the end of 2006 we produced the first measurements of neutron decay with a counting rate of approximately 2 Hz. Through 2007, the collaboration worked on improving the production/transmission of UCN. Several major projects were undertaken. Among them was a full new design of a flapper unit that allows trapping UCN after each proton pulse so they can only move toward the decay area instead of going back to the production area. This flapper unit has important technical constraints because it needs to work reliably for long periods of time within a high radiation environment and at low (≈ 4 K) temperatures, opening and closing at fast rates. By the end of 2007 the spectrum shown in the figure was taken at a total rate of ≈ 22 Hz.

We believe the detection system is ready to do a high precision measurement of the β asymmetry and what is needed at this point is a further significant improvement (≈ 10) in the neutron decay rate to achieve our goal of determining the beta asymmetry with uncertainties of $\approx 0.2\%$.

*A. Saunders, A. Young, spokespersons; the collaboration is formed by approximately 30 scientists from Caltech, Univ. of Kentucky, Los Alamos National Lab., North Carolina State University, Texas A&M, Virginia Tech, Univ. of Washington, Univ. of Winnipeg.

2.10 Positron-neutrino correlation from ^{32}Ar: A reanalysis in view of new data

E. G. Adelberger, A. García, and H. E. Swanson

The positron neutrino correlation in a $0^+ \rightarrow 0^+$ decay can be used to put upper limits on scalar contributions to the Weak Interaction. In 1999 we published data taken at Isolde that allowed determination of the e^+, ν correlation from the superallowed decay of ^{32}Ar, thus placing the tightest constraints on scalar currents at the time.[1]

The extracted e^+, ν correlation coefficient depends on the beta-decay Q value and on the energy calibration of the beta-delayed proton spectrum. Recently[2] we measured ^{32}S(p, γ) to determine excitation energies of some of the states that are fed in the decay of ^{33}Ar, which we used for energy calibration in the ^{32}Ar experiment. The figure below shows the beta-delayed proton spectrum from ^{33}Ar with arrows pointing to the lines whose energies we determined via ^{32}S(p, γ). The beta-decay Q value can be determined using the mass of ^{32}Ar, which was determined using Isoltrap[3] plus our determination of the beta-delayed proton combined with the masses of ^{31}S and the proton.

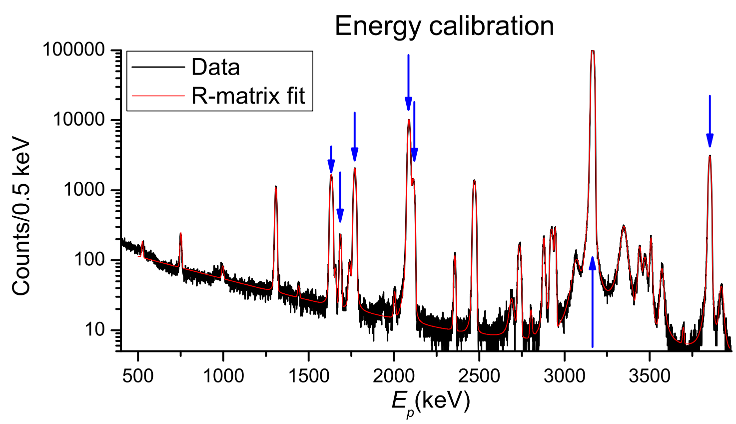

Figure 2.10-1. Beta-delayed proton spectrum from ^{33}Ar with arrows pointing to the calibration lines

In addition to the new data mentioned above in our reanalysis we fixed the response functions of the ^{32}Ar and ^{33}Ar beta-delayed proton spectra to be identical, and we fixed the width of the $T = 3/2$ state in ^{33}Cl to the value measured via scattering.[4] The figure below shows a detail of one of these fits. This results in a correlation coefficient: $\tilde{a} = 0.998(5)$, which is in agreement with no scalar contributions to the Weak Interaction, as prescribed by the Standard Model.

[1] E. G. Adelberger *et al.*, Phys. Rev. Lett. **83**, 1299 (1999).
[2] S. Triambak *et al.*, Phys. Rev. C **73**, 054313 (2006).
[3] K. Blaum *et al.*, Phys. Rev. Lett. **91**, 260801 (2003).
[4] P. G. Ikossi *et al.*, Phys. Rev. Lett. **36**, 1357 (1976); J. F. Wilkerson *et al.*, Nucl. Phys. **A549**, 223 (1992).

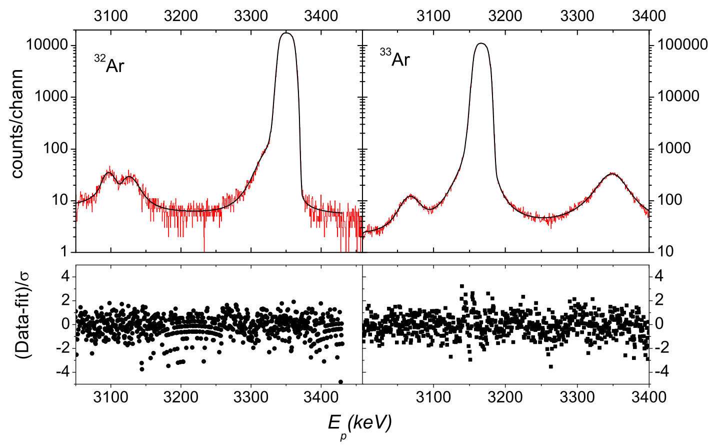

Figure 2.10-2. Simultaneous fit to ^{32}Ar and ^{33}Ar beta-delayed spectra around the superallowed peaks. This is used to extract the e^{+}, ν correlation coefficient.

As by-products of this work, by doing R-matrix fits of the whole beta-delayed proton spectra for both ^{32}Ar and ^{33}Ar, we have determined spectroscopic information (energies, widths and beta feedings) of many states.

Quantum Optics

2.11 Progress on a test of quantum nonlocal communication

J. G. Cramer, W. G. Nagourney, D. G. Prindle, and S. Mzali*

The question we are investigating is whether quantum nonlocality is the private domain of Nature, or whether it can be used in experimental situations to send signals from one observer to another. With the aid of generous private contributions and some use of CENPA resources, we have continued the work on the test of nonlocal quantum communication reported last year.[1] The experiment, described in that reference, employs a high power argon-ion laser operating in the ultraviolet at 351 nm to pump nonlinear crystals (BBO or $LiIO_3$) to produce pairs of momentum-entangled photons, on which measurements are subsequently performed. The initial version of the experiment was temporarily assembled in the UW Laser Physics Facility beginning in late January, 2007. In September, 2007, when a laser table became available in a more permanent laboratory location, the experiment was moved two doors down the hall to Room B055 of the Physics-Astronomy Building, where it presently resides.

In the initial configuration and tests, a Princeton Scientific quantum sensitive cooled-CCD camera was used as the primary photon detector. However, after extensive testing, this CCD detection system was found to be inadequate for the measurements required because of intrinsic noise. Therefore, the experiment was redesigned to use avalanche photodiodes (APD) as the primary photon detectors. This change in photon detection technology was made easier by the similarity in behavior and characteristic between the optical photon detection of APDs and the solid state charged-particle detectors used in nuclear physics experiments. In particular, we were able to implement the APD system with NIM modules borrowed from the CENPA electronics pool. Using funds from private contributions, we purchased five Pacific Silicon Sensor AD100-8-S1 avalanche photodiodes (APD) and two AmpTek A250 charge sensitive preamplifiers, along with high-quality filters and nonlinear crystals. The APD were biased using Tennelec TC280 Bias Supplies. The output of the A250 preamps was amplified and shaped with a CENPA-made Fast-Rise Preamp driving two Ortec 474 Timing-Filter Amplifiers. For coincidence measurements, the APD signals from the TFAs drove two sections of an Ortec Quad Constant-Fraction Discriminator, were reshaped and delayed by a Phillips Scientific 792 Gate/Delay Generator, and were time-matched with an Ortec 418A Universal Coincidence and an Ortec 566 TAC. The system was tested with an LED light pulser and found to have a time resolution of around 1 ns, depending somewhat on APD bias conditions.

The new APD system is now being built into a new configuration of the experiment, and testing is in progress with the light pulser and with entangled photon pairs form the nonlinear crystals. We hope to obtain at least preliminary results bearing on the possibility of nonlocal communication by sometime this Summer.

*UW undergraduate, participated until 10/2007

[1] CENPA Annual Report, University of Washington (2007) p. 52.

3 Nuclear Astrophysics

3.1 Construction of the chamber and completion of the beamline for the ^{22}Na(p,γ) experiment

T. A. D. Brown, A. García, A. L. Sallaska, K. A. Snover, and D. W. Storm

The entire 0° beamline has been completed and can be seen in Fig. 3.1-1. Fig. 3.1-2 displays a view of the chamber. Visible are the liquid nitrogen tank and the feedthrough for the aperture ladder, as well as the front of one detector. A sectional view of the inside of the chamber is illustrated in Fig. 3.1-3.

Figure 3.1-1. Panoramic view of the beamline.

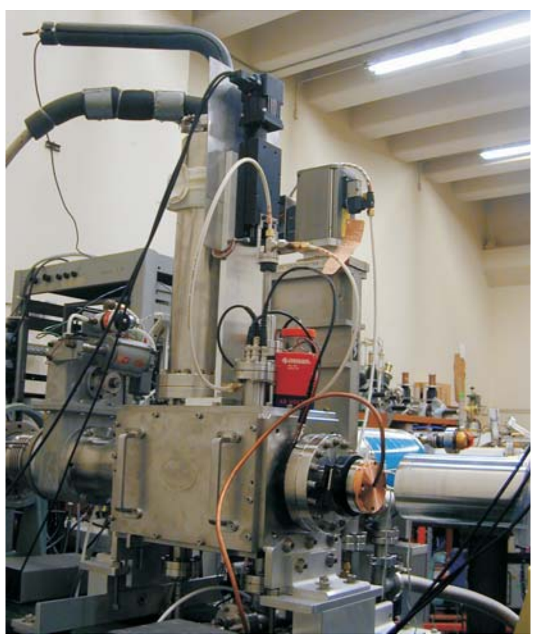

Figure 3.1-2. Side view of the target chamber.

On the chamber, a liquid nitrogen tank is coupled to the upstream copper cold shroud, which is connected to the downstream cold shroud by copper braids (not shown, for clarity). Between the two shrouds is a water cooled, sliding ladder with four different apertures: 1-mm and 3-mm apertures are for tuning purposes, and 7-mm and 8-mm apertures allow the beam to reach the target. Downstream of the ladder is another 8-mm collimator (collimator 1) attached directly to the downstream cold shroud, which is followed by a 10-mm cleanup

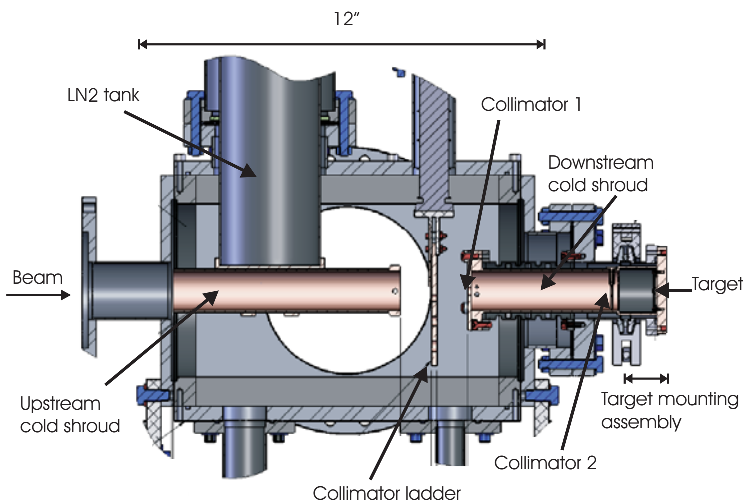

Figure 3.1-3. Sectional view of the target chamber.

collimator (collimator 2). A 3-cm electron suppressor sits directly in front of the target, and the entire downstream cold shroud is connected to the chamber via a stainless steel thermal break. The target extends into the electron suppressor, which is cooled to near liquid nitrogen temperatures. To limit exposure to radiation, the target assembly consists of a KF50 flange bolted directly to the copper backing mount. On this mount, the targets themselves are affixed by compression via a ring clamp. Once the targets are initially mounted to this assembly, the only necessary mounting to the chamber will be done with the quick flange. The backside of the target mount is water cooled, as compressed air cooling was insufficient (see Sec. 3.4).

We have performed cooling tests on the two sections of the cold shroud, which indicate efficiency of the heat transfer of the braids. For the cooling of the two sections of the cold shroud, a temperature sensor was affixed under the clamp that coupled the braids at the end of each section. Fig. 3.1-4 illustrates the cooling from room temperature down to a saturation point for each.

The upstream section is coupled directly to the liquid nitrogen tank and reaches a minimum temperature of 88 K. Because the heat transfer down the braids is not perfect, the saturation temperature for the downstream shroud only reaches 125 K. If successive braids were added to the four present during these tests, it would be possible to decrease this temperature; however, the space in the chamber is limited, and this temperature may be sufficient for our purposes. It should be noted that this temperature is at the front end of the downstream cold shroud, nearest to the aperture ladder; the heat must be further transfered down the shroud to the target $\sim$ 15 cm away.

With the chamber isolated from the rest of the beamline by a gate valve and with the liquid nitrogen tank filled, a vacuum of $1{\times}10^{-8}$ torr has been achieved with a cryopump. There is also a smaller cryopump and a large cold trap upstream of the chamber to pump

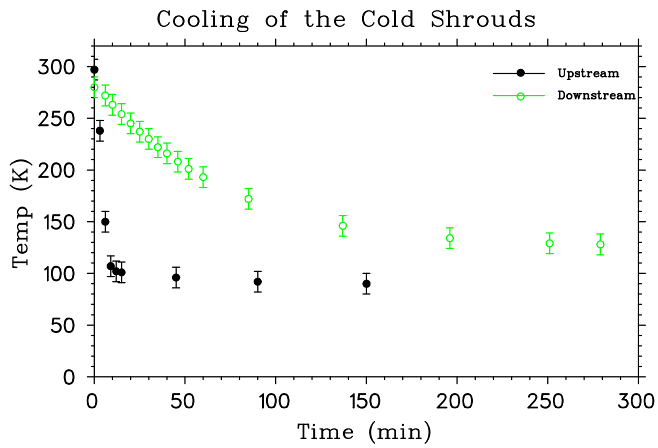

Figure 3.1-4. Cooling of the cold shroud.

out the beamline between the chamber and the switching magnet that directs beam into the six beamlines from the accelerator. Isolated, this section reaches low $\sim 10^{-7}$ torr.

We are currently running with two 100% Germanium detectors at 55° angle to the beam axis with 2.5 cm of lead as shielding from the radioactive target. A battery of Penelope simulations were run to optimize the shielding, and none were extraordinarily better than the others, applying the ratio of the peak efficiency of our gamma ray of interest (5 MeV) to the total efficiency of the 1.275 MeV γ as the figure of merit. In addition to the lead shielding, comic ray shielding has also been installed around the detectors, which consists of plastic scintillators surrounded by lead. These shields were previously used for another experiment so their geometry is not fully optimized for these detectors and will let in some cosmic rays entering from very large angles. However, they will still aid in filtering out excess cosmic rays[1] by rejecting 80% at the energy of interest to this experiment, 5 MeV. Details on the refurbishment of these shields can be seen in Sec. 3.2.

[1]CENPA Annual Report, University of Washington (2007) p. 59.

3.2 Modification of cosmic-ray shielding for the ^{22}Na(p,γ) experiment

A. L. Sallaska and D. W. Storm

In order to reduce the background in the 100% germanium detectors for the ^{22}Na(p,γ) experiment, cosmic-ray shielding is being employed, which consists of lead encased plastic scintillators used in anticoincidence with signals in the germanium. It has previously been shown that this setup reduces the background at a gamma-ray energy of 5 MeV by 80%.[1] Because funding for new scintillators could not be procured, an existing setup was modified to fit the needs of this experiment. This setup includes an annular plastic scintillator as well as a front planar scintillator, both of which fit inside a large lead covering. Previously, the photomultiplier tubes (PMTs) on each annulus had been directly coupled to the flat surface on the back, which was unacceptable for this experiment as they would collide with the cryostat for the germanium detectors. Thus, the PMTs on each annulus had to be moved to the cylindrical side where they would no longer interfere. The planar scintillators posed no problem.

In contrast to their previous construction, the PMTs now required light guides to couple their flat faces to the curved cylindrical surface. Small cylinders of polished lucite were machined to facilitate this coupling and were glued with optical cement directly onto scintillator at the position where center of the germanium crystal would be placed. The PMTs were then glued onto the light guides, which were then covered in black tape to prevent light leaks. In order to accommodate the new PMT positions, the lead covering also had to be modified with a cylindrical hole cut out of the side along the axis where the top portion of the lead interfaced with the bottom to ease assembly. To protect the PMTs, cylindrical cages were machined and affixed to the lead. Also, in their new configuration, the cosmic-ray shields are positioned much closer to one another than in the previous setup, requiring a small portion of lead on the tip of the top section be removed, along with a corresponding section on the aluminum that supports the lead-scintillator setup.

[1] CENPA Annual Report, University of Washington (2007) p. 59.

3.3 TRIM simulations of the ^{23}Na(p,γ) resonance profile at $E_p = 309$ keV

T. A. D. Brown, A. García, and K. A. Snover

The ^{23}Na(p,γ) resonance at $E_p = 309$ keV ($\Gamma < 2$ eV) has been measured using ^{23}Na implanted targets (see Sec. 3.4). For the purposes of understanding the shape of the resonance profile, a series of TRIM[2] simulations have been conducted to calculate the implanted profile of the ^{23}Na and the resulting energy loss of the proton beam. Three types of ^{23}Na target were made, where ^{23}Na was implanted into a copper substrate at three different energies: 10, 20 and 30 keV. Fig. 3.3-1 illustrates the implanted depth profile generated by TRIM for the three implantation energies.

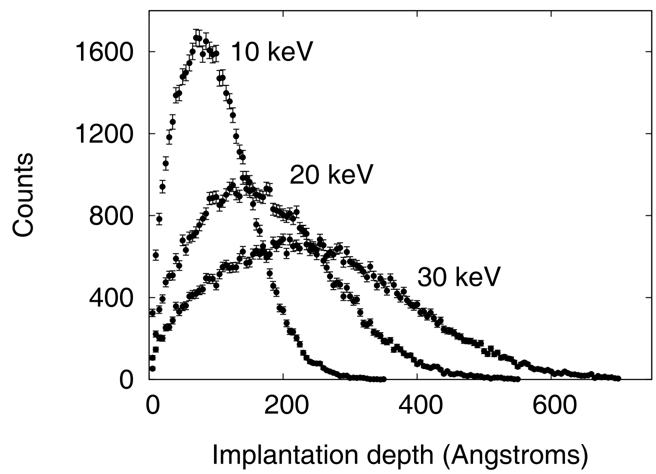

Figure 3.3-1. Implanted ^{23}Na distribution in copper calculated by TRIM for three different bombarding energies.

Using these implantation profiles, TRIM simulations were run at 1-keV intervals for beam energies between 308 and 318 keV to determine the transmitted proton energy distribution in the target. Each incident proton was assigned a target interaction depth equal to the implantation depth of an individual ^{23}Na atom as given by TRIM. The proton bombarding energies were given a Gaussian distribution with a FWHM of 300 eV; the estimated energy resolution of the beam used to make the real measurements. Given the relatively low ^{23}Na implantation densities ($\simeq 10^{16}$ atoms / cm^2) and the stopping power of sodium ($\simeq 70$ % copper stopping power per atom), the target was assumed to be purely composed of copper.

For each bombarding energy, the resulting proton energy distribution was used to calculate the probability of producing a γ-ray (P) from an infinitely narrow resonance at $E_p = 309$ keV. Each proton energy distribution was divided into 50-eV bins so that the following equation could be applied:

$$P \;=\; N_p(Er) \;/\; \Delta E \;/\; N_p(\mathrm{tot}) \tag{1}$$

where $N_p(Er)$ is the number of protons in the bin with $E = 309$ keV, ΔE is the energy width of this bin (50 eV) and $N_p(\mathrm{tot})$ is the total number of transmitted protons. In principle the

[2] J. Ziegler, SRIM: Stopping and Ranges of Ions in Matter, URL www.srim.org.

probability plotted as a function of proton bombarding energy should describe the shape of the resonance for a given ^{23}Na implantation energy. Fig. 3.3-2 illustrates the measured resonance profiles for the three implantation energies (measured before significant target degradation - 1st scans (see Sec. 3.4), plotted with the profiles calculated using the above prescription. Although we get very good agreement between experiment and the calculation in the 30-keV case, we get poor agreement for the lower energies. This lack of agreement may be due to ^{23}Na migration within the target prior to the measurement. The narrower implantation profiles determined by TRIM suggests that these migration effects may be more significant at lower energies. However, the agreement appears to be worst for the 20-keV target. This target was not used until several months after implantation, unlike the 10-keV target where the first resonance measurement was made 4 days after the implantation was completed.

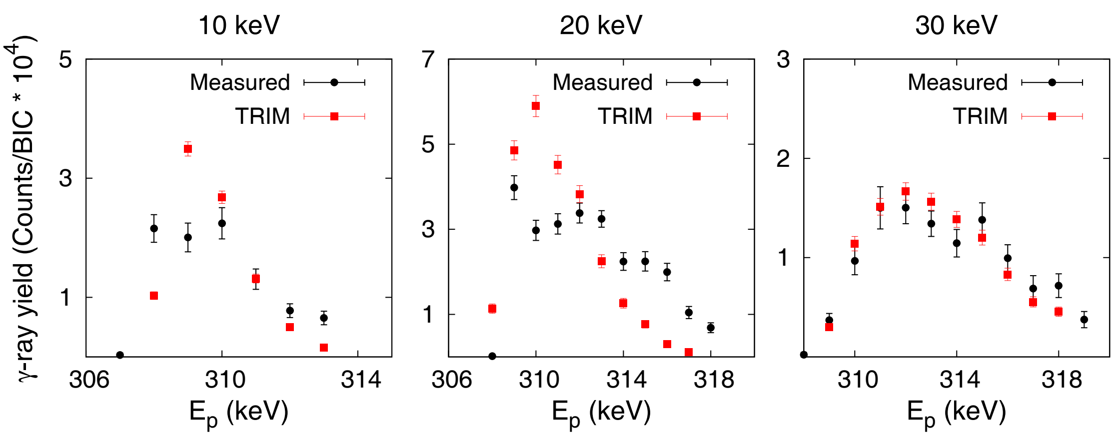

Figure 3.3-2. Comparison of the resonance profiles determined from experiment and calculated using TRIM. The vertical normalization of the calculated profiles has been scaled to match the experimental data. The 10- and 20-keV simulated profiles have been given a -1 keV offset so that they are better aligned with the experimental results.

In an effort to understand the above discrepancies, we have assumed that the ^{23}Na migration has an effect which can be described by folding a Gaussian function with the implantation profiles given by TRIM. Following this procedure we were able to find good agreement assuming that the target implantations needed to be folded with a 200 Å (FWHM) Gaussian for the 10-keV target and a 500 Å Gaussian for the 20-keV target.

3.4 Proton beam tests of ^{23}Na implanted targets

T. A. D. Brown, K. Deryckx, and A. L. Sallaska

Three ^{22}Na implanted targets (originally 10 μCi, 185μCi and 300μCi) have been fabricated at TRIUMF in preparation for a ^{22}Na(p,γ) resonance measurement at $E_p \simeq 200$ keV. The ^{22}Na has been implanted into a copper substrate at an energy of 30 keV. The density and distribution of the ^{22}Na within the copper are vulnerable to heating and sputtering effects under beam bombardment. The degradation of targets implanted in a similar fashion has been observed in previous ^{22}Na(p,γ) resonance measurements.[1] For the purposes of investigating the effects of proton beam bombardment, new targets were implanted using the stable isotope ^{23}Na. These implantations were performed using the Sputter Ion Source on the tandem accelerator. A ^{23}Na beam was rastered over a 1-cm diameter collimator positioned approximately 6 cm upstream of a copper target. ^{23}Na targets were fabricated using beam energies at 10, 20 and 30 keV, in each case achieving an implantation density of approximately 10^{16} atoms / cm^2. The implantation profile for each of these energies has been determined using TRIM simulations (see Sec. 3.3).

All the ^{23}Na implanted targets were tested in the chamber set-up for the ^{22}Na(p,γ) measurement (see Sec. 3.1). An unshielded HPGe detector was positioned along the beam axis directly behind the target, such that the distance between the front of the detector and the target was approximately 16 cm. The ^{23}Na(p,γ) resonance at $E_p = 309$ keV was used to monitor the target degradation as a function of total accumulated charge. At the beginning of each target bombardment, the shape of the resonance was determined by measuring the $E_\gamma = 4.238$ MeV yield for a range of beam energies at 1-keV intervals between 308 and 319 keV. This profile measurement was repeated on later occasions during the bombardment. The shape and the area of the resonance profile provide a description of the implanted ^{23}Na distribution and the amount of ^{23}Na within the target. In between each of these resonance measurements, the target was bombarded at a beam energy equal to the peak energy recorded in the first resonance measurement. The $E_\gamma = 4.238$ MeV yield was recorded every hour as a function of the total accumulated charge. For all of the above measurements the beam was rastered over the target and the current was typically held between 40 and 50 μA.

Initial tests performed with a 10-keV implanted target, using an air jet to cool the target mount, yielded results which indicated a sudden loss of ^{23}Na after the beam current was increased from 38 to 50 μA. This suggested that the current increase was accompanied by a sharp temperature rise in the target. Subsequent beam tests were performed so that the temperature of the back of a blank copper target could be recorded. Using a rastered beam at $E_p = 309$ keV and $I \simeq 45$ μA, the temperature was found to rise by 50 to 80 K in 3 minutes after putting beam on target, depending on the air pressure and jet position. This large temperature rise demonstrated the deficiency of using an air cooled system under such conditions and was the prime motivation behind the introduction of a water-cooled target mount.

Fig. 3.4-1 illustrates the peak yield and resonance profile measurements made for water-

[1] F. Stegmüller, Nucl. Phys. A **601,** 168 (1996).

cooled targets. For the 10-keV target, the area under the second resonance curve is only 48 ± 4 % of the area under the first, i.e. approximately half of the ^{23}Na atoms have been lost from the target between these two measurements. The sharp drop at the beginning of the peak yield plot suggests that these atoms were lost within the first 2 C. The 20-keV target was found to have a much better beam resistance. There were no sudden changes in the peak yield, and it was found to decrease linearly at a rate of 3 % per C. However, the resonance profile measurements indicated that 40 ± 3 % of the sodium had been lost after 7.3 C. The 30-keV target peak yield decreased at a rate of 2 % per C, while the resonance profile measurements indicate that there was no (statistically) significant loss of sodium after 11 C.

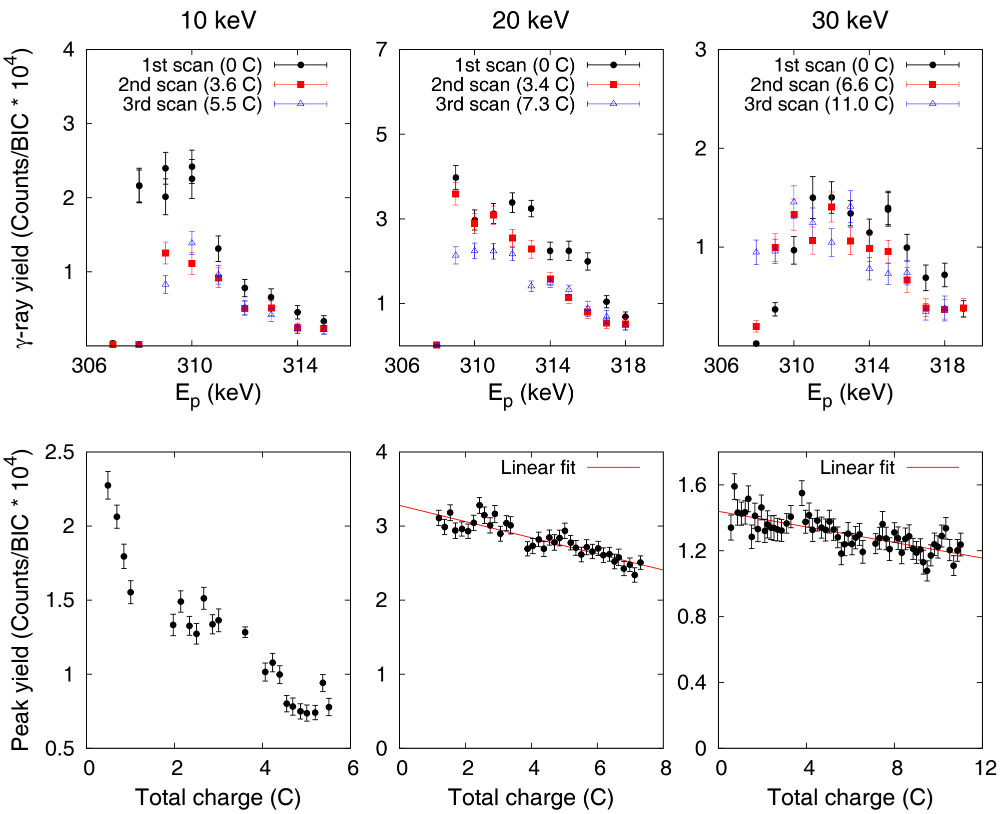

Figure 3.4-1. Resonance profile and peak yield measurements for ^{23}Na targets implanted at three different energies. All measurements were performed with a water-cooled target mount. For a given resonance profile measurement, the total charge deposited on the target prior to the measurement is given.

Given the large loss of ^{23}Na in a relatively short period of time, these results suggest that new ^{22}Na targets implanted at 10 and 20 keV would not be suitable for long – approximately 20 C – resonance measurements. However, it may be possible to reduce the amount of sodium sputtering by evaporating a layer of protective material over the implanted area. In preparation for a future test a new ^{23}Na 10 keV target has recently been fabricated, upon which a thin layer ($\simeq$ 100 Å) of chromium has been evaporated.

4 Nuclear Structure

4.1 ^{100}Tc electron capture branching ratio measurement

K. S. Deryckx, A. García, S. A. Hoedl, D. Melconian, S. K. L. Sjue, H. E. Swanson, and S. Triambak*

We have two motivations to determine the electron-capture (EC) branch from ^{100}Tc: to determine the efficiency of a potential charged-current neutrino detector sensitive to neutrinos from the pp chain; and to get a better understanding on calculations of nuclear matrix elements for double beta decay. There are no concrete plans to build a ^{100}Mo neutrino detector at this point, but the second motivation remains strong: understanding the calculations of nuclear matrix elements in the $A = 100$ system should apply to the other double-beta decay candidate systems as well.

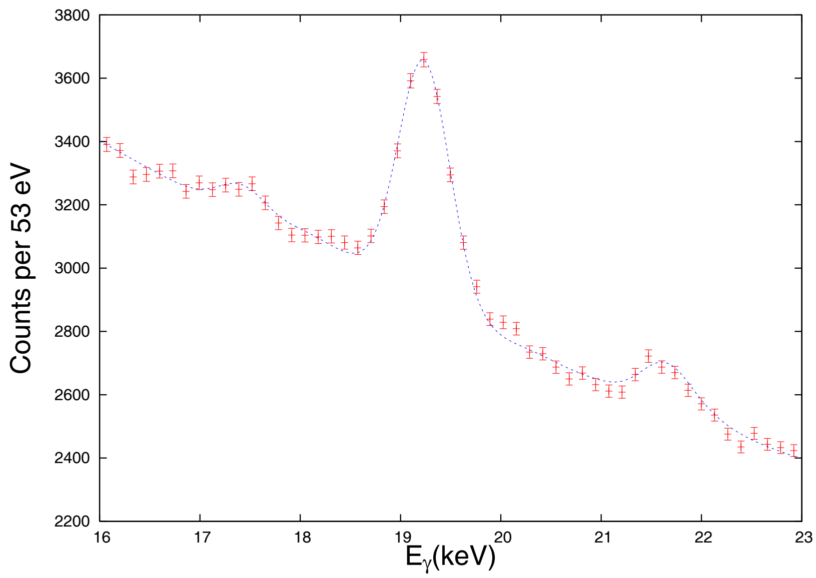

Figure 4.1-1. X ray spectrum from ^{100}Tc. The Mo x rays at $E_\gamma \sim 17.5$ keV are produced in EC decays.

We have just finished taking data at Jyväskylä, where ^{100}Tc ions were produced using the local cyclotron and then stopped in He gas to prevent neutralization. Then the ion beam was extracted, bunched in an RFQ mass filter, and purified in a Penning trap. Finally the ^{100}Tc ions were ejected from the trap into a scintillator with a thin wall, next to which a planar Ge detector was placed. This allowed veto of the profuse beta-related events to better observe the x rays from EC events.

We are presently on the process of analyzing our data. Our preliminary number is: $BR(\mathrm{EC}) = (1.1 \pm 0.2) \times 10^{-5}$.

*Department of Physics, Univ. of Guelph, Guelph, Ontario N1G 2W1

4.2 Isospin breaking in the superallowed decay of ^{32}Ar

E. G. Adelberger, M. Bhattacharya,* A. García, A. Komives,† D. Melconian,‡
H. E. Swanson, and S. Triambak§

The superallowed decay of ^{32}Ar presents a good opportunity to test isospin breaking corrections. Here the correction, usually called *radial overlap*, is about a factor of 5 larger than in the cases that have been measured with the best precision.

We implanted ^{32}Ar ions produced at the NSCL(MSU) into the setup shown in the figure below and had clear identification. We measured the beta-delayed protons and gammas.

Our result for the superallowed branch, $b^{\beta}_{\rm SA} = (22.71 \pm 0.16)\%$, along with the previously determined ^{32}Ar half-life and energy release, is used to determine the ft value of the superallowed decay. This ft value, together with the corrected $\mathcal{F}t$ value extracted from 9 precisely known $T = 1$ superallowed decays, yields the isospin symmetry breaking correction in ^{32}Ar decay $\delta_C^{\rm exp} = (2.4 \pm 0.8)\%$. This can be compared to a theoretical calculation $\delta_C = (2.0 \pm 0.4)\%$.

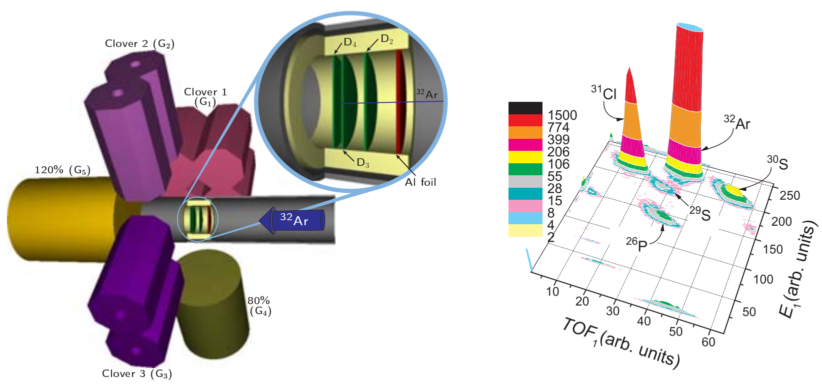

Figure 4.2-1. Left: sketch of detector setup; Right: E vs. TOF spectrum used to identify incoming ions.

In order to produce a stringent test of the theory, a different version of this experiment is being considered.

As by-products of this work, we determined the γ and proton branches for the decay of the lowest $T = 2$ state of ^{32}Cl, made a precise determination of the total proton branch and relative intensities of proton groups that leave ^{31}S in its first excited state, and deduced a value for the ^{32}Cl mass with ≈ 1.6 keV uncertainty, compared to the previous 6.6 keV uncertainty.

*Brookhaven National Laboratory, PO. Box 5000, Upton, NY 11973-5000.
†Department of Physics and Astronomy, DePauw University, Greencastle, IN 46135.
‡Physics Dept., Texas A & M Univ., 4242 TAMU, College Station, TX 77843-4242
§Department of Physics, Univ. of Guelph, Guelph, Ontario N1G 2W1

4.3 ^{54}Mn decay rate

E. G. Adelberger, A. García, S. K. L. Sjue, and H. E. Swanson

We monitored the decay rate of a 10 μCi ^{54}Mn source with a 100% Ge detector in search of deviations from exponential decay. It has been suggested that the decay rate varies in a way correlated with solar activity.[1] The source and detector were enclosed in a 20 cm-thick Pb shield to minimize backgrounds around the 834.848 keV γ-ray. The electronics were kept in a temperature-controlled rack to minimize gain drifts. No statistically significant deviations were observed. Our fitted half-life of $T_{1/2} = 311.12 \pm 0.82$ days can be compared with the quoted half-life, $T_{1/2} = 312.05 \pm 0.04$ days.[2]

A new setup to continue the effort with a different detector is under planning and construction.

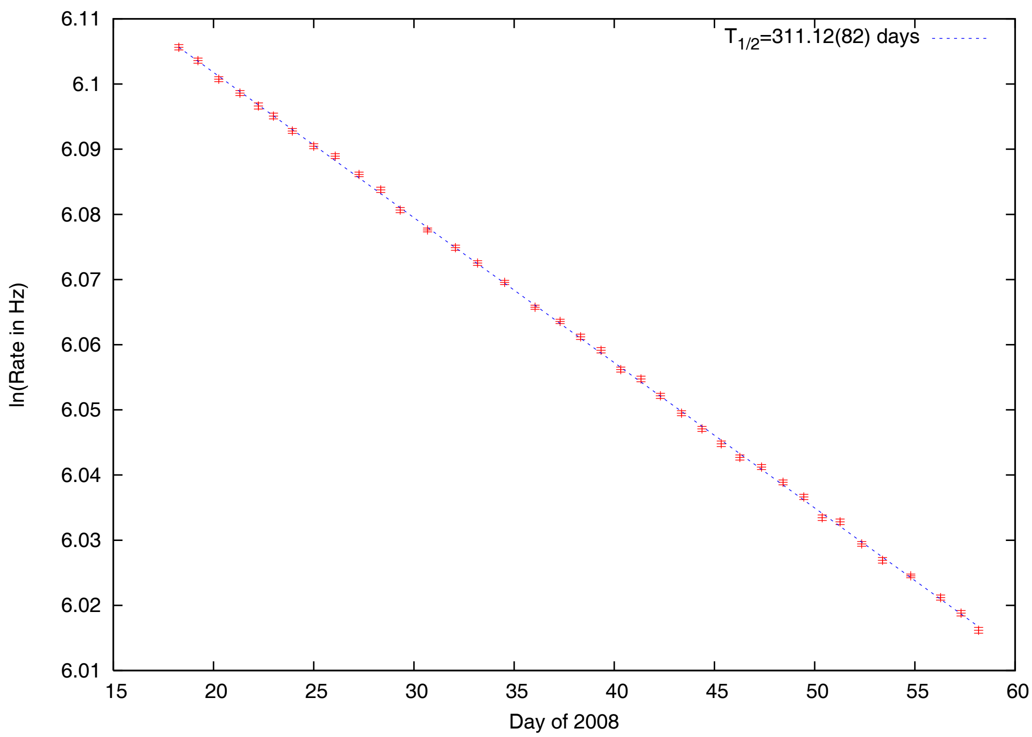

Figure 4.3-1. Preliminary analysis of forty days of ^{54}Mn decay.

[1]Private communication, E. Fischbach to E.G. Adelberger

[2]Nuclear Data Sheets 107, 1393 (2006).

5 Relativistic Heavy Ions

5.1 Summary of event structure research

T. A. Trainor

Until recently this program has emphasized two-particle correlation analysis of nuclear collisions at RHIC. We discovered persistent structure even in central Au-Au collisions at 200 GeV and identified the primary contributions as minijets (fragments from a minimum-bias scattered parton spectrum) and the azimuth quadrupole (conventionally called "elliptic flow"). Both contributions vary strongly with collision centrality and energy. Our results appear to be inconsistent with claims of rapid thermalization and hydrodynamic flow on a collective partonic medium exhibiting very low viscosity ("perfect liquid"). To resolve the apparent contradictions we have focused in the past two years on differential studies of single-particle spectrum structure and azimuth quadrupole systematics. General topics include

- Continuing survey of number correlations in A-A collisions emphasizing minijets
- Identified hadron correlations in preparation for time-of-flight barrel installation
- Differential two-component analysis of p_t and y_t spectra for identified hadrons
- Study of parton energy loss with single-particle spectra and minijet correlations
- Comprehensive study of azimuth quadrupole energy and centrality systematics
- Isolation of the differential quadrupole component as identified hadron spectra on y_t
- The relation of minijets and parton dissipation to the A-A reaction plane
- Rejection of the hydrodynamic model at RHIC with differential data analysis
- Novel QCD phenomena: color screening and gluonic quadrupole radiation

Several issues from our previous summary have been resolved. "Flow" and "nonflow" have been accurately distinguished with our 2D angular autocorrelations, and the nonflow mechanism is identified. The energy and centrality dependence of the p_t-integrated quadrupole component have been determined accurately in Au-Au collisions, with surprising results. The properties of the azimuth quadrupole ("elliptic flow") contradict a hydrodynamic interpretation! Interpretation of spectra in terms of thermodynamic state variables and the concept of a "partonic medium" in heavy ion collisions are questionable. Collision dynamics appear to be closer to N-N linear superposition with modest secondary parton scattering.

Our recent results appear to be consistent with a model of nuclear collisions above 13 GeV in which 1) participant nucleons fragment along the collision axis (soft component), 2) some low-x partons scatter to large angles and 3) their hadron fragments appear as correlations at mid-rapidity (hard component). Those components may interact when the transverse particle density exceeds a threshold. The interaction (parton energy loss) is manifested in modification of parton fragment distributions down to very small p_t or y_t. The quadrupole component appears to be completely independent of the soft and hard components, exhibiting independent systematics which suggest a QCD radiation process.

5.2 Restoring the QCD power law to the hard spectrum component

T. A. Trainor

Spectra of p_t are expected to go asymptotically to power-law trend $1/p_t^n$ at larger p_t, reflecting an underlying power-law parton spectrum. The hard component in p-p p_t spectra is well described by a Gaussian on y_t for $p_t < 6$ GeV/c. However, that description is inadequate at larger p_t, and a power-law trend must be restored to the model. An exponential tail can be added to the Gaussian on y_t to restore the QCD power law to the hard-component model.

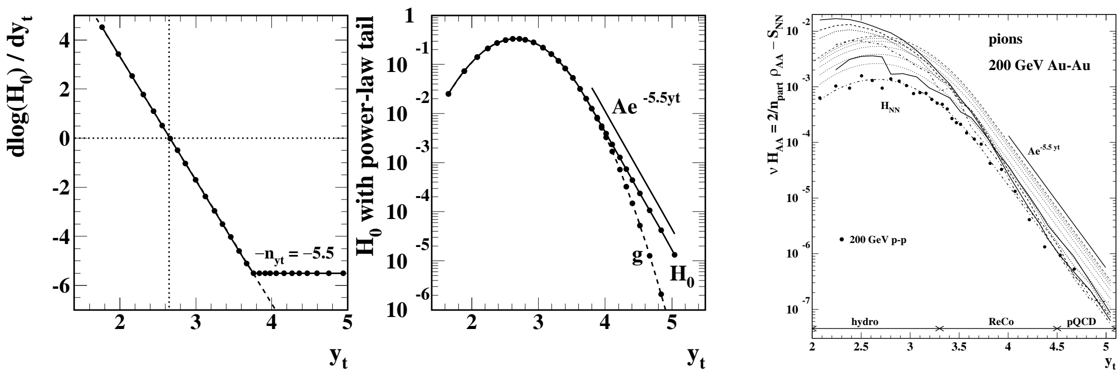

Figure 5.2-1. Left panel: The logarithm derivative for a Gaussian (dashed line) and Gaussian plus exponential tail (solid lines). Center panel: Gaussian (dashed curve) and Gaussian plus exponential (power-law) tail (solid curve). Right panel: Comparison of Gaussian-plus-tail hard component H_{NN} to p-p (solid dots) and Au-Au (bold curves) data.

Extension of the hard-component model to a Gaussian with exponential tail (power law on p_t) results in qualitatively better descriptions of data beyond $p_t = 6$ GeV/c. Description of p-p and peripheral Au-Au collisions is very good to 12 GeV/c. The QCD power-law exponent is expected to be $n_h \sim 7.5$, or $n_{y_t} \sim 5.5$. There is a possible difference between pion and proton exponents—7.5 *vs* 7.0 respectively—at a two-sigma level of significance.

The hard-component model function is defined on transverse rapidity y_t. If the QCD power law is $\rho(p_t) \propto p_t^{-n_h}$ and $\rho(y_t) = \frac{m_t p_t}{y_t}\rho(p_t)$ then $-d\log[\rho(y_t)]/dy_t \sim (n_h - 2) + 1/y_t$ Since the region relevant to the power-law trend is $y_t \sim 5$, and systematic uncertainties in the exponent are comparable to 0.2, I define $n_{y_t} = n_h - 2$ as the relevant exponential constant on y_t. Since $n_h \sim 7.5$ I expect $n_{y_t} \sim 5.5$ for data.

In Fig. 5.2-1 (left panels) the algebraic strategy is illustrated. The hard-component Gaussian model (dashed curve g in the center panel) is $g(y_t) = A_h \exp\{-[(y_t - \bar{y}_t)/\sigma_{y_t}]^2/2\}$, with logarithm derivative $d\log(g)/dy_t = -(y_t - \bar{y}_t)/\sigma_{y_t}^2$ shown by the dashed line in the left panel. To add an exponential tail to the Gaussian the logarithm derivative in the left panel must be limited from below by fixed value $-n_{y_t}$ (solid line in the left panel). The running integral of the resulting function (solid curve in the center panel) is then exponentiated to obtain the desired Gaussian with exponential tail as hard-component model $H_0(y_t)$. The dash-dot hard-component curve in the right panel is compared to p-p (solid dots) and Au-Au data.

5.3 Two-component centrality evolution of single-particle y_t spectra for indentified hadrons from 200 GeV Au-Au collisions

T. A. Trainor

The two-component description of hadron spectra in p-p collisions accurately describes data in terms of longitudinal nucleon (soft) and transverse parton (hard) fragmentation. For RHIC A-A collisions the two-component spectrum model provides an essential reference, and a means for differential spectrum study. In Fig. 5.3-1 (left panels) y_t spectra for pions and protons from five Au-Au centralities are plotted in the conventional format (five solid curves). Soft component S_{NN} is a Lévy distribution on m_t. N-N hard-component reference H_{NN} (dash-dot curve) is a Gaussian with exponential tail, the smooth transition to the QCD p_t power-law trend. At lower right a power-law trend is sketched. The dotted curves are two-component reference curves for the five values of ν from data, bracketed by dashed curves for limiting cases $\nu = 1$, 6. Suppression of the more-central spectra at large p_t relative to the reference is qualitatively apparent.

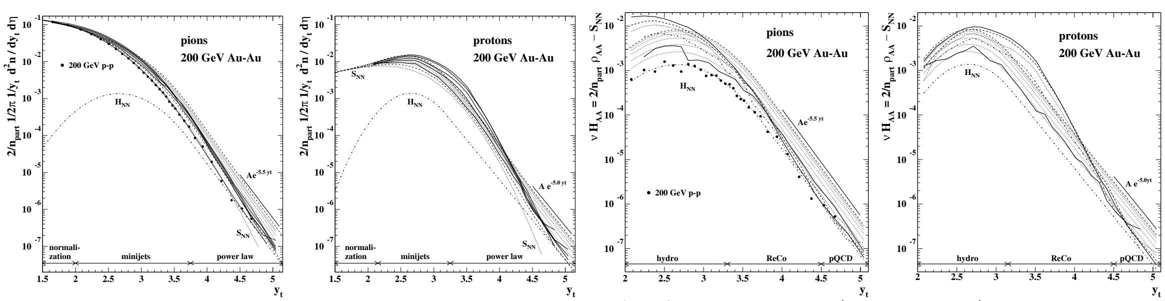

Figure 5.3-1. First panel: Pion y_t spectra for five Au-Au centralities (solid curves). Second panel: Comparable proton y_t spectra. Third panel: The hard component of pion y_t spectra in the form $\nu\, H_{AA}$ (thicker curves with changing line style) compared to two-component reference $\nu\, H_{NN}$ (dotted curves). Fourth panel: Comparable results for proton y_t spectra.

In Fig. 5.3-1 (right panels) $\nu\, H_{AA}$ for pions and protons are plotted. A common soft component S_{NN} has been subtracted from the Au-Au spectra. The N-N hard-component reference H_{NN} (lower, dash-dot model curve) is adopted from p-p collisions but with a power-law tail. The dotted reference curves describe $\nu\, H_{NN}$ for the five data centralities, the reference system. The remarkable new feature of these figures is the large excesses compared to the N-N referenc in localized y_t regions for more central collisions. Whereas there is a substantial reduction of fragments at larger y_t there is strong enhancement at smaller y_t. The small-p_t interval is conventionally claimed for hydro and blast-wave fitting models. The trend with increasing centrality is a shift to *smaller* y_t. The inconsistency with hydro becomes more evident in the proton spectra. In Fig. 5.3-1 (fourth panel) I show $\nu\, H_{AA}$ for protons in five Au-Au centralities (bold curves with different line styles), and the hard-component reference H_{NN} (dash-dot curve) inferred from analysis of the Au-Au spectra. There was no *a priori* model for the proton hard component. It was determined iteratively for this analysis just as for the p-p analysis. Spectrum variation with ν was extrapolated to $\nu = 0$ to obtain the soft-component Lévy parameters. The ν variation of the remainder suggested the presence of a hard model function similar to that for pions and hadrons.

5.4 The proton-to-pion anomaly and two-component y_t spectra

T. A. Trainor

We can use the two-component spectrum model to study the proton-to-pion ratio, which has received considerable theoretical attention. Fig. 5.4-1 (first panel) summarizes the model functions for pions and protons obtained from a two-component analysis of spectrum data. The dotted curves are the fixed soft components S_{NN}. The dash-dot curves are N-N hard components H_{NN}, and the solid curves are H_{AA} for $b = 0$ Au-Au.

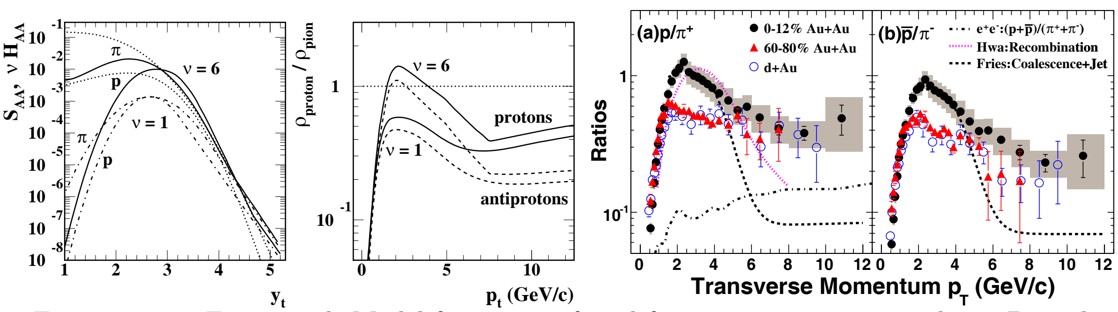

Figure 5.4-1. First panel: Model functions inferred from two-component analysis. Dotted curves are soft components for protons and pions. Dash-dot curves are hard-component N-N ($\nu = 1$) references. The solid curves are hard components for $\nu = 6$ generated from the hard-component N-N references plus parton energy-loss parameterizations $r_{AA}(y_t;\nu)$. Second panel: Proton-to-pion two-component full-spectrum ratios on p_t. Right panels: Published p/π spectrum ratios showing the anomaly for p_t = 2-4 GeV/c.

Using two-component parameters densities $2/n_{part}\,\rho_{AAh} = \{S_{NN} + \nu\, r_{AA}(y_t;\nu)H_{NN}\}$ are defined for the two hadron species. Spectrum ratios $\rho_{\mathrm{AAproton}}/\rho_{\mathrm{AApion}}$ are plotted in the second panel, labeled "protons" for $\nu = 1$, 6 (solid curves). Those results can be compared with published data in the right panels. Correspondence with the measured ratios is good. The proton-to-pion puzzle is thus transformed to details of *parton energy loss and modified fragmentation.*

The full-spectrum ratios share the property of R_{AA} that they mix soft and hard spectrum components, suppressing details at smaller p_t. The change of the spectrum ratio with centrality is actually modest. There is at the peak (2 GeV/c) only a factor 2$\times$ increase for central Au-Au collisions relative to N-N collisions. In the first panel the hard-component ratio for N-N collisions (dash-dot curves) is 1 already at $y_t = 2.66$ ($p_t \sim 1$ GeV/c), descends to 0.5 near 4 GeV/c and then *rises through unity again* due to the apparent difference in the underlying parton spectra (that for protons being harder). For central Au-Au collisions we observe an excess of protons *above* the proton hard-component peak mode and an *even larger excess* of pions *below* the pion hard-component mode. The differential hard components provide a much more detailed story than full-spectrum ratios. Comparing to ratios of fragmentation *functions* (FFs) from e^+-e^- collisions (third panel) introduces further confusion because the spectrum hard components are fragment *distributions* (FDs)—integrals of FFs folded with parton spectra. In general, fully-differential formats such hard-component ratio r_{AA} provide a clearer comparison of different hadron species.

5.5 Defects in the conventional high-p_t spectrum R_{AA} measure

T. A. Trainor

The spectrum ratio R_{AA} used to infer "jet quenching" at larger p_t mixes soft and hard components and is difficult to interpret. In Fig. 5.5-1 (left panels) R_{AA} for pions and protons is plotted on y_t. The thin solid curves are the two-component references for five centralities. The main inference from R_{AA} is "jet quenching"—reduction of data *from unity* in the pQCD region $p_t > 6$ GeV/c ($y_t > 4.5$). Adopting unity as a reference overestimates the magnitude of the reduction, since there is still a substantial soft-component contribution in that interval. The correct reference for each centrality is the corresponding thin model curve. The R_{AA} definition suppresses hard-component structure in the small-p_t region. The entire fragment distribution should be compared to the correct two-component reference.

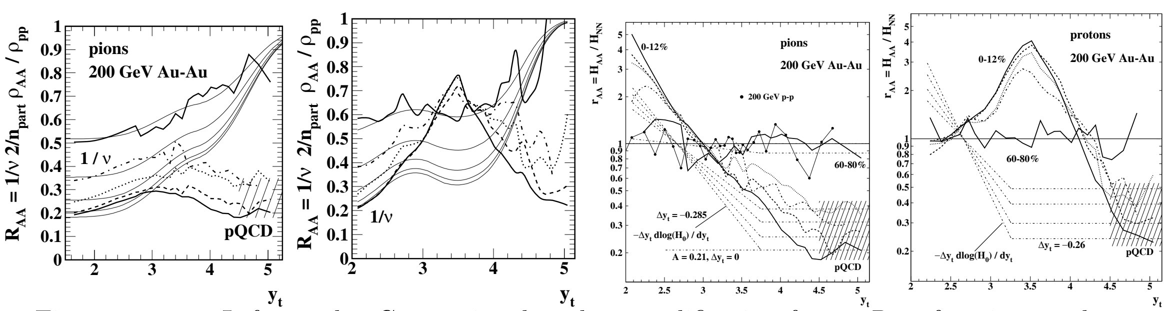

Figure 5.5-1. Left panels: Conventional nuclear modification factor R_{AA} for pions and protons for five Au-Au centralities on y_t (thicker curves with changing line styles). The thin reference curves in each panel are obtained from the two-component model. The R_{AA} limit for small y_t is $1/\nu$. Right panels: Hard-component ratios for pions and protons for five Au-Au centralities (thicker curves with changing line styles) relative to the N-N hard-component reference. The connected dots are data from NSD p-p collisions. The dash-dot lines represent a simple parton energy-loss scenario.

Hard-component references and data are compared *directly* over the entire p_t or y_t acceptance in the form of hard-component ratio $r_{AA} \equiv H_{AA}/H_{NN}$ which generalizes R_{AA} as a measure of parton energy loss. Fig. 5.5-1 (right panels) shows H_{AA}/H_{NN} *vs* y_t, with H_{AA} for pions and protons from five Au-Au centrality classes. The line $r_{AA} = 1$ describes the two-component reference for all centralities (all dotted $\nu\, H_{NN}$ curves). Deviations from 1 represent all residuals from the two-component reference. The trend above $y_t \sim 4.5$ is consistent with R_{AA} measurements. However, below that point the data rise monotonically through 1 and continue to rise for smaller y_t. The centrality trends at smaller y_t are closely (anti)correlated with the trend near $y_t \sim 5$, strongly suggesting that the two widely-separated y_t regions are physically connected by the parton energy-loss and fragmentation process.

The new information from this ratio format is the large excesses of pions for $p_t \sim 0.5$ GeV/c and protons for $p_t \sim 2.5$ GeV/c, apparently linked to parton energy loss. The proton excess is part of the "proton-to-pion" ratio anomaly.

5.6 Parton energy loss and color screening in 200 GeV Au-Au collisions

T. A. Trainor

Parton energy loss can be determined by comparing hard-component spectrum structure in A-A collisions with an N-N reference, as in the r_{AA} ratio. In Fig. 5.6-1 (left panels) hard-component ratios r_{AA} are plotted *vs* y_t for pions (first panel) and protons (second panel) from Au-Au collisions in five centrality classes. The dash-dot lines represent a negative-boost energy-loss scenario—uniform shift of the entire hard component structure to smaller rapidity. Despite a horizontal offset between data and model curves the similarities suggest that parton energy loss is dominated by a negative boost of *some part* of the underlying parton distribution. The offsets suggest that lower-energy partons experience less energy loss.

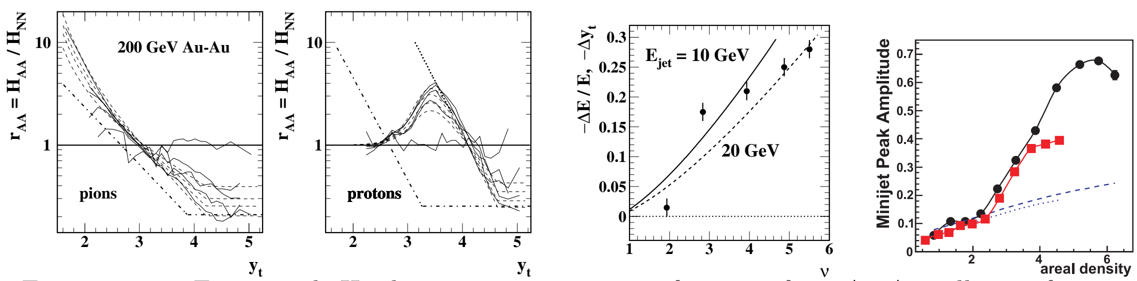

Figure 5.6-1. First panel: Hard-component ratios r_{AA} for pions from Au-Au collisions for five centralities (solid curves). Dash-dot lines represent a rapidity shift Δy_t (negative boost) of the entire N-N hard-component reference H_{NN}. Second panel: Hard-component ratios for protons. The features are similar to the left panel. Third panel: Negative boosts Δy_t for y_t spectra from five centralities of Au-Au collisions (points) and theoretical predictions of relative energy loss $\Delta E/E$ for two parton energies (curves). Fourth panel: Peak amplitudes for same-side minijet peaks in 200 GeV Au-Au.

The dash-dot curves in Fig. 5.6-1 (left panels) are defined by

$$\log[r_{AA}(y_t;\nu)] \quad = \quad -\Delta y_t(\nu)\, d\log(H'_{NN})/dy_t \tag{1}$$

$\Delta y_t(\nu)$ is the negative boost for path-length (centrality) ν, and H'_{NN} is H_{NN} with centroid shifted from 2.66 to 3.1 for pions and 4.2 for protons. The r_{AA} model assumes that all centrality dependence is contained in multiplicative factor Δy_t. In Fig. 5.6-1 (third panel) $-\Delta y_t$ is plotted *vs* participant path length ν compared to theoretical relative energy loss $\Delta E/E$ for 10 GeV (solid curve) and 20 GeV (dashed curve) partons, with $\Delta y_t \sim \Delta p_t/p_t \sim \Delta E/E$ (signed numbers). The Δy_t data trend appears to exhibit a step-wise transition near $\nu = 2.5$. The theoretical centrality dependence is $\Delta E/E \propto \nu^2$, roughly gluon density $(\sim \nu) \times$ outgoing parton pathlength $(\sim \nu)$. The prediction is close to data, but there is no discontinuity in the theory. A sharp transition is also seen in minijet correlation peak systematics. Fig. 5.6-1 (fourth panel) shows same-side minijet peak amplitudes from 62 and 200 GeV Au-Au collisions plotted *vs* areal density. At smaller y_t the trend of r_{AA} for both pions and protons is a return to (and through) unity, which could be interpreted as a decrease in relative parton energy loss, an increase in fragment number due to energy loss or both. The proton data especially seem to indicate that low-energy partons lose little or no energy. Such behavior could signal the onset of color screening at smaller energy scales as part of the hadronization process.

5.7 Integral spectrum measures in a two-component model

T. A. Trainor

Integral spectrum measures are used to infer thermodynamic trends for heavy ion collisions. However, such interpretations can be misleading. In Fig. 5.7-1 (first panel) I show pion spectrum integrals from a two-component model derived from data. The dotted line is the integral of soft component $S_{NN\pi}$. The solid curve is the full spectrum integral, including parton energy loss. The dash-dot line $0.85\,\rho_0[1+0.012(\nu-1)]$ is the extrapolation from N-N collisions. Parton energy loss is thus responsible for a factor $5\times$ increase in pion fragments for central Au-Au collisions relative to the N-N extrapolation. Fig. 5.7-1 (second panel) shows equivalent results for protons. The proton hard component in N-N collisions is a much larger fraction of the total proton yield (11% compared to 1.2% for pions). The increased fragment yield from parton energy loss is 30% for protons (from dash-dot to solid curve) compared to $5\times$ for pions. The large hard-component excess in Au-Au collisions over the N-N extrapolation is thus due to the substantial increase in pion yield resulting from parton energy loss.

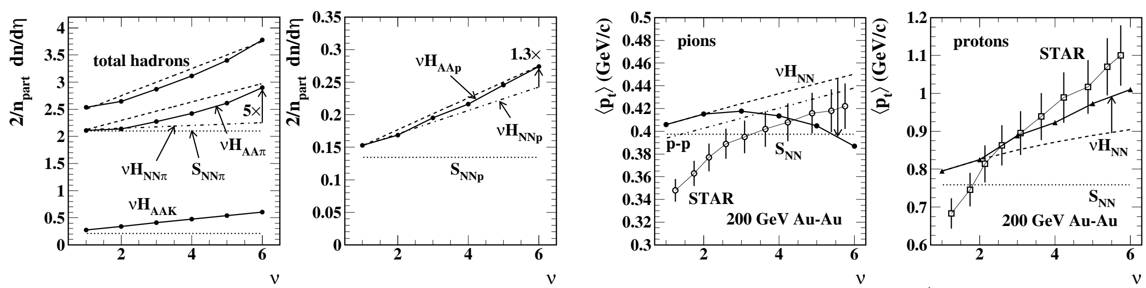

Figure 5.7-1. First panel: Spectrum integrals for pion soft component $S_{NN\pi}$ (upper dotted line) and hard component $\nu\,H_{AA\pi}$ which sum to the middle solid curve. The dash-dot line extrapolates the pion hard-component reference from N-N collisions. Second panel: Similar curves for integrated proton spectra. Third panel: Pion $\langle p_t\rangle$ trends from two-component model functions. The dotted line is the fixed soft component. The dashed line adds the extrapolated N-N reference. The solid curve (total) includes parton energy loss. The open symbols are published data. Fourth panel: Same as the third panel, but for protons.

We can also use the two-component model spectra to determine $\langle p_t\rangle$, the ensemble mean p_t. Fig. 5.7-1 (right panels) show $\langle p_t\rangle$ values obtained with two-component model functions from pion and proton data. The dotted lines are from soft component $\langle p_t\rangle_{S_{NN}}$. The dashed lines show the two-component trend for no parton energy loss. The solid curves and points are from the full data model with energy loss. For pions (third panel) the spectrum mean (solid curve) can drop *below* the dashed line (arrow) because the additional pion yield for central collisions appears below the hard-component spectrum peak. For protons (fourth panel) the solid curve rises above the dashed line (arrow) because the additional proton yield appears above the hard-component peak mode. The apparent mass dependence of $\langle p_t\rangle$ and increase with A-A centrality is commonly interpreted to result from radial flow in heavy ion collisions, described for instance by a blast-wave model. From this analysis the major contribution to the mass dependence is the soft component, which does not change with A-A centrality from N-N collisions. The centrality dependence due to parton energy loss is opposite for pions and protons, further contributing to the false impression of a radial flow phenomenon.

5.8 Charge-independent angular autocorrelations in Au-Au collisions at $\sqrt{s_{NN}} = 62$ and 200 GeV

M. Daugherity,* R. L. Ray,* and T. A. Trainor

p_t-integrated 2D angular autocorrelations reveal two dominant physical processes in RHIC A-A collisions: minijets (minimum-bias jets) and the azimuth quadrupole (conventionally interpreted as "elliptic flow"). Recent comprehensive data from angular autocorrelations exhibit novel properties of both processes. Fig. 5.8-1 (left panels) shows 2D autocorrelations for 90-100% and 10-20% central 200 GeV Au-Au collisions. The results for 62 GeV are qualitatively similar. The first panel is equivalent to N-N collisions. 2D autocorrelations are fitted with model functions

$$\frac{\Delta\rho}{\sqrt{\rho_{\text{ref}}}} \equiv \frac{\Delta\rho_{\text{nf}}}{\sqrt{\rho_{\text{ref}}}}(\eta_\Delta, \phi_\Delta) + 2\sum_{m=1}^{2} \frac{\Delta\rho[m]}{\sqrt{\rho_{\text{ref}}}} \cos(m\phi_\Delta). \tag{1}$$

The main structure is minijets (first term on the RHS) and sinusoids, of which the $m = 2$ quadrupole term is associated with "elliptic flow." Quadrupole results are described in other reports.

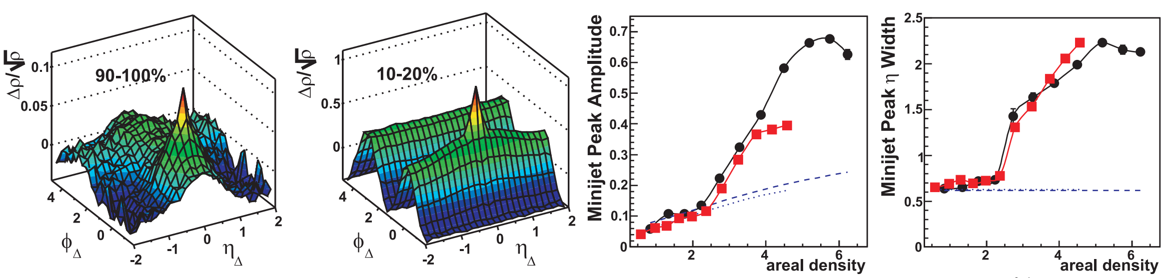

Figure 5.8-1. Left panels: 200 GeV Au-Au angular autocorrelations for 90-100% and 10-20% centralities. Right panels: Amplitude and η width of the same-side minijet peak *vs* transverse areal particle density for 62 and 200 GeV.

Fig. 5.8-1 (right panels) show the centrality dependence (measured by transverse areal particle density) of the same-side minijet peak amplitude and width on pseudorapidity η. The most notable result is the sharp transitions near areal density ~ 2.5. The dashed and dotted curves in the third panel indicate extrapolations of N-N collision trends in a Glauber model, an N-N linear superposition reference. The combination of amplitude and width increases beyond the reference lead to a pair-number increase of nearly $9\times$, corresponding to a fragment number increase of $3\times$ over N-N linear superposition and associated with parton energy loss.

Corresponding sharp transitions are seen in hard-component ratio r_{AA} for pion and proton spectra which describe parton energy-loss systematics. The combined effects suggest a possible coupling (e.g., parton secondary scattering) between soft and hard spectrum components (longitudinal and transverse fragmentation) above a critical particle density. The transition points vary with energy on mean participant path length ν but appear at a common transverse particle density at 62 and 200 GeV.

---

*University of Texas (Austin)

5.9 Contribution of resonance decays to identified two-particle correlations: Results from Monte-Carlo event generators.

D. J. Prindle and T. A. Trainor

Studying correlations on $(\eta_\Delta, \phi_\Delta)$ of identified particles produced in high energy AuAu and CuCu collisions we found interesting structures, appearing also in simulated Hijing events. The K^+K^- number and p_t correlations have ring shaped structures centered at (0,0),[1] and a number of other channels may have similar structure. To study resonance contributions to two-particle correlations we turned to an event generator named THERMINATOR.[2]

THERMINATOR is a Monte Carlo event generator designed for studying particle production in relativistic heavy-ion collisions. Parameters were chosen to simulate a central 200GeV AuAu collision. Thermal events were generated according to the Cracow single-freeze-out model and include all particles from the Particle Data Tables. We can adjust the particle abundances by hand, generating event samples consisting of single types of particles whose energy and angular distributions are similar to real data. We generated and analyzed single particle type event samples for K^0_s, ρ^0, $K^*(892)$, ϕ, Λ and $\Lambda^*(1520)$ in addition to full events. For this study we accepted only $0.1 < p_{\pi^\pm} \leq 1.0$, $0.1 < p_{K^\pm}$ $0.2 < p_p < 1.5$ (momentum in GeV/c) where the STAR TPC has some particle identification efficiency via dE/dx. In Fig. 5.9-1 we show examples of two-particle correlations due to just ϕ decay (panels 1 and 2) and just ρ^0 decay (panels 3 and 4).

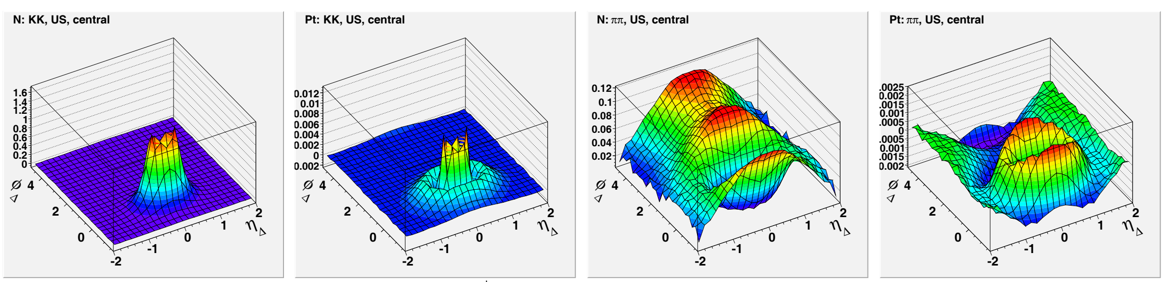

Figure 5.9-1. Panels 1 and 2 show K^+K^- number and p_t correlations on $(\eta_\Delta, \phi_\Delta)$ due to ϕ decays. Panels 3 and 4 show $\pi^+\pi^-$ number and p_t correlations on $(\eta_\Delta, \phi_\Delta)$ due to ρ^0 decays.

The thermal boost is large enough that decays with a small q-value, such as the ϕ, have their decay products boosted to relatively small opening angles, giving an essentially circular two particle correlation. Decays with a large q-value, such as the ρ^0, have large opening angles. When the decay is parallel to the beam axis one of the decay products is often outside our acceptance, while if it is perpendicular to the beam axis we have complete acceptance. Effectively, the two-particle correlation is modulated by our one-particle acceptance.

All of the resonances listed above are observable (although the $\Lambda^*(1520)$ is marginal) even in full THERMINATOR events for specific channels and momenta ranges. We can also identify most of these resonances in full Hijing events.

[1] CENPA Annual Report, University of Washington (2007) p. 69.
[2] A. Kisiel et al. Comput. Phys. Commun. **174**, 669 (2006).

5.10 Contribution of resonance decays to two-particle correlation data.

D. J. Prindle and T.A. Trainor

In the previous article we showed that if we could restrict particle production in heavy ion collisions to particular resonances we would observe strong two-particle correlations, at least in particular channels, due to resonance decays. In this section we discuss how large these contributions are for real events.

Total per-particle p_t correlations between bin a and bin b can be written as[1]

$$\frac{\Delta\rho}{\rho_{\mathrm{ref}}} = \frac{\overline{(\mathrm{p_t}-\overline{\mathrm{p}}_\mathrm{t})_\mathrm{a}(\mathrm{p_t}-\overline{\mathrm{p}}_\mathrm{t})_\mathrm{b}}}{\sqrt{\overline{\mathrm{n}}_\mathrm{a}\overline{\mathrm{n}}_\mathrm{b}}}$$

where $\mathrm{p_t}$ is the total transverse momentum in an event (within bin a or b), n is the total number of particles and the average is over events. ρ_{ref} is typically determined using mixed events. Noting $\mathrm{p_t}-\overline{\mathrm{p}}_\mathrm{t} = (\mathrm{p_t}-\mathrm{n}\hat{\mathrm{p}}_\mathrm{t}) + \hat{\mathrm{p}}_\mathrm{t}(\mathrm{n}-\overline{\mathrm{n}})$ (where $\hat{\mathrm{p}}_\mathrm{t}$ is the particle mean $\mathrm{p_t}$ of all tracks) this correlation can be decomposed into number correlations, mean $\mathrm{p_t}$ correlations, and the covariance of the two.

$$\frac{\Delta\rho}{\rho_{\mathrm{ref}}} = \hat{\mathrm{p}}_\mathrm{t}{}^2\frac{\overline{(\mathrm{n}-\overline{\mathrm{n}})_\mathrm{a}(\mathrm{n}-\overline{\mathrm{n}})_\mathrm{b}}}{\sqrt{\overline{\mathrm{n}}_\mathrm{a}\overline{\mathrm{n}}_\mathrm{b}}} + \mathrm{cov}(\mathrm{n},\mathrm{p_t}) + \frac{\overline{(\mathrm{p_t}-\mathrm{n}\hat{\mathrm{p}}_\mathrm{t})_\mathrm{a}(\mathrm{p_t}-\mathrm{n}\hat{\mathrm{p}}_\mathrm{t})_\mathrm{b}}}{\sqrt{\overline{\mathrm{n}}_\mathrm{a}\overline{\mathrm{n}}_\mathrm{b}}}$$

where the first term is the contribution due to number correlations and the third term is due to mean $\mathrm{p_t}$ correlations. We can further decompose each of these terms into, for example, a resonance and a non-resonance part. Denoting particles due to resonance decays as $\mathrm{n_r}$ and the rest as $\mathrm{n_n}$ the number correlations decompose to

$$\begin{aligned}\frac{\Delta\rho_\mathrm{n}}{\rho_{\mathrm{ref}}} &= \frac{\overline{(\mathrm{n_n}-\overline{\mathrm{n}}_\mathrm{n})_\mathrm{a}(\mathrm{n_n}-\overline{\mathrm{n}}_\mathrm{n})_\mathrm{b}}}{\sqrt{\overline{\mathrm{n}}_\mathrm{a}\overline{\mathrm{n}}_\mathrm{b}}} + \mathrm{cov}(\mathrm{n_n},\mathrm{n_r}) + \frac{\overline{(\mathrm{n_r}-\overline{\mathrm{n}}_\mathrm{r})_\mathrm{a}(\mathrm{n_r}-\overline{\mathrm{n}}_\mathrm{r})_\mathrm{b}}}{\sqrt{\overline{\mathrm{n}}_\mathrm{a}\overline{\mathrm{n}}_\mathrm{b}}} \\ &= \sqrt{\frac{\overline{\mathrm{n}}_\mathrm{na}\overline{\mathrm{n}}_\mathrm{nb}}{\overline{\mathrm{n}}_\mathrm{a}\overline{\mathrm{n}}_\mathrm{b}}}\frac{\Delta\rho_{\mathrm{n_n}}}{\rho_{\mathrm{ref}}} + \mathrm{cov}(\mathrm{n_n},\mathrm{n_r}) + \sqrt{\frac{\overline{\mathrm{n}}_\mathrm{ra}\overline{\mathrm{n}}_\mathrm{rb}}{\overline{\mathrm{n}}_\mathrm{a}\overline{\mathrm{n}}_\mathrm{b}}}\frac{\Delta\rho_{\mathrm{n_r}}}{\rho_{\mathrm{ref}}}\end{aligned}$$

where the first term is the non-resonance contribution and the third term is the resonance contribution. (The mean $\mathrm{p_t}$ and number-$\mathrm{p_t}$ covariance terms have similar decompositions.) In a model such as THERMINATOR the number-number covariance term comes primarily from the resonance decay chain and is expected to be small.

We see that the relative contribution of a resonance to the overall correlation is $\overline{\mathrm{n}}_\mathrm{r}/\overline{\mathrm{n}}_\mathrm{n}$, at least in cases where $\overline{\mathrm{n}}_\mathrm{a} \approx \overline{\mathrm{n}}_\mathrm{b}$. For THERMINATOR, in the ϕ only events we accept an average of 4.6 K^+ (and 4.6 K^-) per event compared to 65 K^+ (and 61 K^-) for full events. The ϕ contribution to full THERMINATOR events in the K^+K^- channel will be 0.079 of Fig. 5.9 -1. This is still quite observable, since there is little other structure in K^+K^-. On the other hand, we accept an average of 782 positive and 766 negative particles per event in full THERMINATOR events, so Fig. 5.9 -1 is scaled by 0.0013 for unidentified plus-minus correlations. This is too small to observe with our current data samples.

[1]T. A. Trainor, R. J. Porter and D. J. Prindle, J. Phys. G **31**, 809 (2005).

5.11 So-called 'nonflow" identified as an aspect of minijet production

D. T. Kettler and T. A. Trainor

Nonflow in conventional elliptic flow analysis is a systematic contribution to v_2 data which does not relate to hydrodynamics. We have quantitatively identified the main source of nonflow as minijets. Fig. 5.11-1 (left panels) shows a Monte Carlo simulation in which 2D angular autocorrelations containing a flow sinusoid and minijet correlations are generated for several Au-Au centralities according to our measurements. The solid curves and points represent the parameters inferred from 2D fits to the simulated autocorrelations. The dashed curves represent the model parameters (input) used to construct the simulated distributions. The agreement is excellent. The fits to 1D projections on ϕ_Δ (dash-dot curve) however differ markedly from the 2D fit results and the input. The differences are similar to the variations of conventional flow measures with different strategies to eliminate "nonflow." With 2D autocorrelations we can accurately distinguish multipole contributions from minijet contributions.

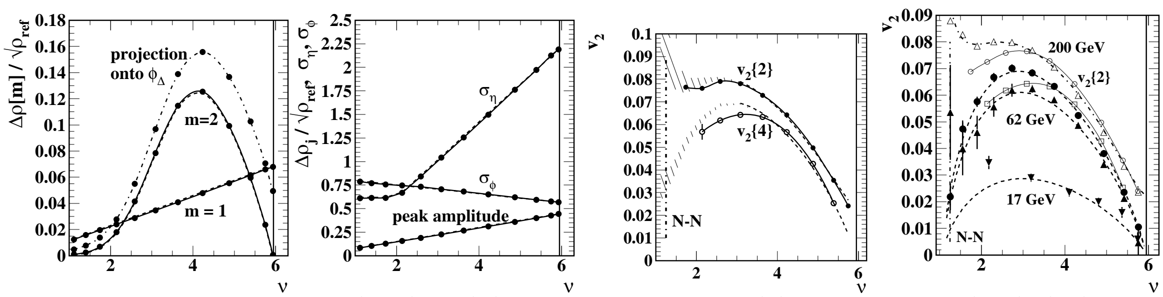

Figure 5.11-1. First panel: The solid curves are input model parameters. The dashed curves are results of fits to the model 2D autocorrelations. The dash-dot curve represents 1D fits to projections on ϕ_Δ corresponding to conventional $v_2\{EP\}$ and $v_2\{2\}$ flow analysis. Second panel: Minijet model parameters derived from correlation data and used in the simulation. Third panel: Conventional flow measures $v_2\{2\}$ and $v_2\{4\}$ (points and solid curves) and Monte Carlo simulations from this work (dashed curves). The hatched regions reflect uncertainties in the definition of eccentricity ϵ. Fourth panel: Quadrupole measurements (solid points for 62 and 200 GeV) using 2D angular correlations from real data.

Fig. 5.11-1 (third panel) shows STAR published v_2 data (points), and 1D and 2D fits to the simulations (dashed curves). The hatched regions indicate the uncertainty in ϵ for peripheral collisions. v_2 is substantial for peripheral A-A and N-N collisions and falls toward zero for central collisions, typical of per-pair correlation measures which contain an extraneous factor $1/n_{ch}$. $v_2\{2\}$ "two-particle correlation" measurements are typically larger than event-plane (EP or "standard") measurements although they estimate the same quantity. The $v_2\{4\}$ are four-particle cumulant measurements intended to eliminate "nonflow" contributions (minijets). The difference between $v_2\{2\}$ and $v_2\{4\}$ has been interpreted as "nonflow" in the past, but more recently has been attributed entirely to v_2 fluctuations. The difference is comparable in shape and magnitude to the difference between fits to the 2D angular autocorrelation and its 1D projection (dashed curves), which is exactly the $m = 2$ component of the Fourier decomposition of the same-side minijet peak, implying that "nonflow" in conventional flow analysis is dominated by crosstalk between minijet correlations and the quadrupole amplitude in a 1D projection on ϕ_Δ.

5.12 What eccentricity estimate is correct for A-A collisions at RHIC?

D. T. Kettler and T. A. Trainor

Interpretation of the A-A azimuth quadrupole requires an accurate eccentricity model, but there are major uncertainties about the correct model for nuclear collisions. Small-x transverse parton structure could be described by a continuum distribution, by point-like participant nucleons or by something intermediate. In Fig. 5.12-1 (left panels) the solid curves show an optical Glauber eccentricity estimate for 200 GeV Au-Au collisions accurately described by a beta distribution on $\log_{10}(n_{bin})$. The dash-dot curves are obtained from a participant-nucleon (Monte Carlo) Glauber model. The difference between optical and Monte Carlo curves is most dramatic for peripheral and central collisions. The large value $\epsilon \to 1$ for peripheral A-A $\to$ N-N collisions implies that N-N collisions are *on average* rod-like (action at a distance). Nonzero ϵ for central A-A collisions implies structure resulting from modeling nuclei as distributions of point-like participant nucleons. What justifies that model for parton (gluon) interactions at $x \sim 0.01$?

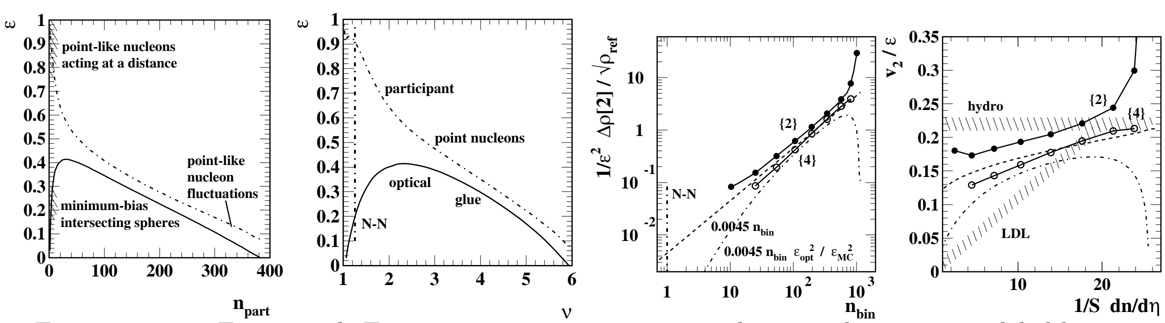

Figure 5.12-1. First panel: Eccentricity ϵ *vs* participant nucleon number n_{part} modeled by an optical (solid) and participant-nucleon (dash-dot) Monte Carlo Glauber. Second panel: The same curves plotted on mean participant path length ν. Third panel: Quadrupole measure $\Delta\rho[2]/\sqrt{\rho_{ref}}$ divided by ϵ^2 (optical Glauber) *vs* binary-collisions estimator n_{bin}. Fourth panel: Conventional ratio v_2/ϵ *vs* collision-number estimator $1/S\, dn_{ch}/d\eta$. The hatched regions represent low-density-limit (LDL) and ideal hydro expectations.

In Fig. 5.12-1 (third panel) v_2 data are plotted in the format $1/\epsilon^2\, \Delta\rho[2]/\sqrt{\rho_{ref}}$ *vs* n_{bin}, the number of binary collisions from a Monte Carlo Glauber simulation. Data derived from $v_2\{4\}$ are well approximated by

$$1/\epsilon^2\, \Delta\rho[2]/\sqrt{\rho_{ref}} \quad = \quad 0.0045\, n_{bin}, \qquad (1)$$

suggesting that the azimuth quadrupole may be determined *solely by initial-state collision parameters* $(b, \sqrt{s_{NN}}, A)$. The surprisingly simple linear relation suggests that the physical mechanism of the quadrupole component is the same from N-N to central A-A collisions. It is therefore important to test its validity with accurate data over the broadest possible centrality range and for other collision systems (e.g., lighter A-A and lower energies). In Fig. 5.12-1 (fourth panel) STAR v_2 data are plotted in the hydro format v_2/ϵ *vs* $1/S\, dn/d\eta$, the latter reflecting the low-density limit (LDL) expectation that v_2/ϵ increases toward a thermal hydro limit with increasing number of in-medium particle collisions as part of an equilibration process. Neither data set follows the hatched LDL trend. The dashed curve is transformed from the dashed line in the left panel.

5.13 Obtaining quadrupole amplitudes from 2D autocorrelations

D. T. Kettler and T. A. Trainor

Measurements of the azimuthal quadrupole moment, commonly represented as v_2, have been one of the major results at RHIC. Although there is a wide variety of techniques used to measure v_2, usually attributed to the phenomenon of 'elliptic flow', most of them either do not reliably distinguish between so-called flow and nonflow effects or do so in very model-dependent ways. Here we present a method that makes use of 2D angular autocorrelations to measure accurately and effectively the azimuth quadrupole even in the presence of large nonflow terms. An autocorrelation is derived from pair density $\rho(x_1, x_2)$ by averaging it along diagonals in space (x_1, x_2) parallel to the sum axis. A 2D autocorrelation is made by applying this procedure to two pairs of variables simultaneously, in this case a projection from the $(\phi_1, \phi_2, \eta_1, \eta_2)$ space onto the $(\phi_\Delta, \eta_\Delta)$ space. The upper left panel in the figure below gives an example of such a 2D autocorrelation. The joint autocorrelation can then be decomposed into Fourier components on azimuth.

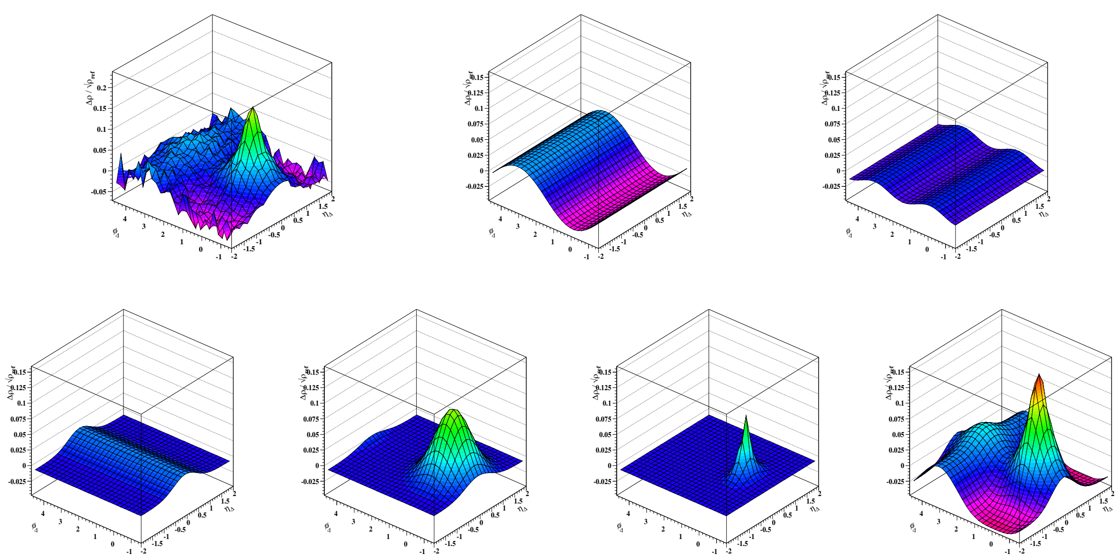

Figure 5.13-1. Data (upper left), fit components, and final combined fit (lower right)

The Fourier coefficients can be compared to the standard v_2 measure with the relation $\Delta\rho[m]/\sqrt{\rho_{ref}} = n v_m^2/2\pi$. A simple Fourier decomposition is all that is necessary if the only sources of correlations are related to flow. However, in real data there will also be significant contributions from nonflow terms. The key to distinguishing them is the information on the η_Δ axis, because within the STAR TPC acceptance elliptic flow is observed to be independent of η to good approximation. The principal structures are a 2D same-side Gaussian peak, a 1D gaussian on η_Δ, a dipole component $\cos(\phi_\Delta)$, and a quadrupole component $\cos(2\phi_\Delta)$. There is also a sharp peak at the origin representing electron pairs and HBT effects which we have modeled here with an exponential. In order to measure the azimuthal quadrupole we fit all components and extract the quadrupole term, which can then be related to the conventional v_2 measure as described above.

5.14 Azimuth quadrupole measurements from 2D angular autocorrelations

D. T. Kettler and T. A. Trainor

2D angular autocorrelations provide accurate separation of quadrupole (elliptic flow) and minijet (nonflow) correlations. Fig. 5.14-1 (first panel) shows 200 GeV Au-Au 2D angular autocorrelations for the 22-32% centrality bin. Autocorrelations for 62 GeV have similar features but with quantitative differences. Fig. 5.14-1 (second panel) summarizes 2D fits of $\Delta\rho[2]/\sqrt{\rho_{\rm ref}}$ for 200 GeV (solid dots) and 62 GeV (solid upright triangles) data, with corresponding values of $v_2\{2D\}$ (third panel) for comparison to previous analyses. $v_2\{\rm EP\}$ data from NA49 (inverted solid triangles) provide a reference for energy-dependence systematics.

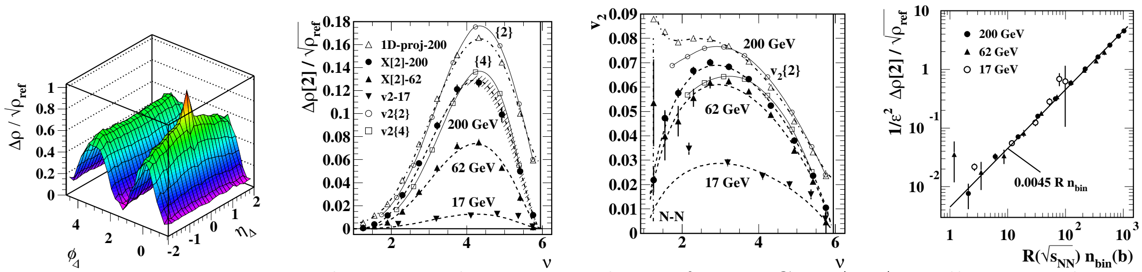

Figure 5.14-1. First panel: 2D angular autocorrelation for 200 GeV Au-Au collisions and 22-32% centrality. Second panel: Quadrupole component $\Delta\rho[2]/\sqrt{\rho_{\rm ref}} \equiv X[2]$ inferred from model fits to 2D angular autocorrelations (solid dots and upright triangles). Third panel: $v_2[2D]$ from 2D autuocorrelations (solid points). v_2 data at $\sqrt{s_{NN}} = 17$ GeV are inverted solid triangles in both panels. Dashed curves have the same form for all energies above 13 GeV. Dash-dot curves include "nonflow." Fourth panel: Azimuth quadrupole divided by optical ϵ^2 *vs* energy-dependent factor $R(\sqrt{s_{NN}})$ times 200 GeV Au-Au binary-collision number $n_{bin}(b)$.

Published data for two-particle $v_2\{2\}$ (open circles) and four-particle cumulant $v_2\{4\}$ (open squares) at 200 GeV are compared to $v_2\{2D\}$ (solid points) from this 2D autocorrelation analysis. The $v_2\{1D\}$ (open triangles) are fits of $\cos(2\phi_\Delta)$ to 1D projections onto ϕ_Δ of the 200 GeV 2D autocorrelations, roughly consistent with the $v_2\{2\}$ analysis. The nonflow offset, the difference between open triangles and solid dots, is exactly the $m = 2$ Fourier component of the same-side minijet peak. $v_2\{4\}$ is expected to eliminate nonflow. The open squares in Fig. 5.14-1 (center panels) are closer to the 2D analysis, but systematic deviations well outside published uncertainties remain. Fig. 5.14-1 (fourth panel) shows $1/\epsilon^2_{\rm opt}\, \Delta\rho[2]/\sqrt{\rho_{\rm ref}}$ *vs* n_{bin}, the number of binary N-N collisions. The data are well described by the model

$$\frac{\Delta\rho[2]}{\sqrt{\rho_{\rm ref}}}(n_{bin}, \sqrt{s_{NN}}) \;=\; A\, R(\sqrt{s_{NN}})\, n_{bin}\, \epsilon^2_{\rm opt}(n_{bin}). \tag{1}$$

$R(\sqrt{s_{NN}}) \equiv \log\{\sqrt{s_{NN}}/13 \text{ GeV}\}/\log(200/13)$ describes the energy scaling, with intercept 13 ± 1 GeV. Coefficient A is defined by $1000A = 4.5 \pm 0.2$. Eccentricity $\epsilon_{\rm opt}(n_{bin})$ was derived from an *optical* Glauber simulation. Eq. (1) accurately describes measured p_t-integrated azimuth quadrupole moments in heavy ion collisions for all centralities over three decades down to N-N collisions and all energies down to $\sqrt{s_{NN}}$ ~13 GeV. Transformed to each plotting space it is the basis for the dashed curves in the center panels.

5.15 Monte Carlo studies of v_2 measurement methods

D. T. Kettler and T. A. Trainor

Given the large number of existing methods used to measure the azimuthal quadrupole moment in heavy ion collisions it is desirable to test some of these methods under controlled conditions. In this analysis we use a Monte Carlo simulation to explore two types of correlation signals. First there are minijets which are described by two or more particles distributed according to a two-dimensional Gaussian probability function about the jet center. The number of particles in a minijet is determined according to a Poisson distribution. The second source of correlation comes from flow terms. These terms are implemented by first randomly selecting a true reaction plane and then biasing the distribution of single particles and minijet centers by sinusoids.

We present measurements using $v_2\{2\}$, $v_2\{4\}$, $v_2\{2D\}$, and $v_2\{1D\}$. $v_2\{2\}$ is the conventional two-particle cumulant method and $v_2\{4\}$ is the four-particle cumulant. $v_2\{2D\}$ is obtained using two dimensional fits to 2D autocorrelations. $v_2\{1D\}$ is the fit to the same data projected onto ϕ_Δ using only Fourier components, and thus cannot distinguish flow from nonflow. For all of the simulation results, the difference between $v_2\{2\}$ and $v_2\{1D\}$ is completely negligible, which is to be expected as both are really just variants on a simple two-particle azimuthal correlation. For the sake of simplicity we just plot $v_2\{2\}$.

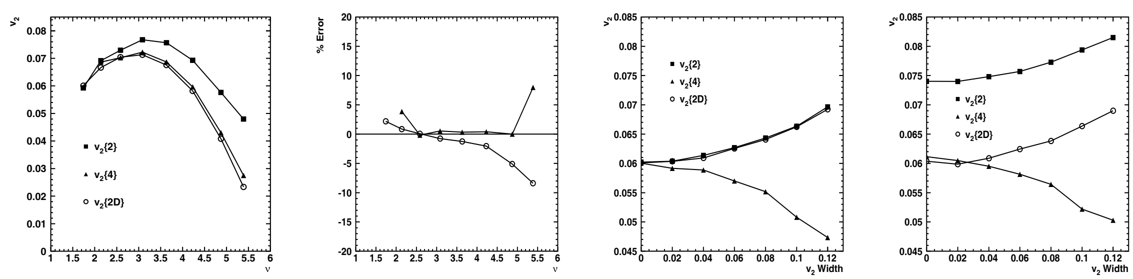

Figure 5.15-1. Measurements of v_2 from Monte Carlo data

In the leftmost plot above we see results for $v_2\{2\}$, $v_2\{4\}$, and $v_2\{2D\}$ as a function of simulated centrality described by the mean participant path length ν. While $v_2\{2\}$ appears to be quite distinct, the other two methods are very close. The next panel shows $(v_2\{\text{measured}\} - v_2\{\text{true}\})/v_2\{\text{true}\}$ for $v_2\{4\}$ and $v_2\{2D\}$. The decreasing accuracy of $v_2\{2D\}$ for very central events is expected due to very large η widths in the minijet peaks, and in practice an average of these open measurements and an imposed binary-collision scaling hypothesis is used. The difference between $v_2\{2\}$ and $v_2\{4\}$ is an important quantity because the it is usually attributed to some combination of nonflow and v_2 fluctuation effects. The difference between $v_2\{1D\}$ and $v_2\{2D\}$ is similar, however it is only sensitive to nonflow. Thus the combination of the two types of methods can potentially be used to accurately measure the effect of flow fluctuations. This is demonstrated in the rightmost two panels which show measured v_2 as a function of the size of imposed fluctuations. The first panel has nonflow turned off and the second panel has it turned on.

5.16 Is the azimuth quadrupole related to A-A collision evolution and thermalization?

D. T. Kettler and T. A. Trainor

Recent analysis suggests that the azimuth quadrupole, identified as "elliptic flow," may not be coupled significantly to most of the A-A collision evolution. Fig. 5.16-1 (first panel) incorporates two interesting trends in quadrupole data: 1) all energies are described by the same centrality variation, and 2) the energy dependence of the quadrupole amplitude is $\propto \log(\sqrt{s_{NN}}/13 \text{ GeV})$. A similar energy dependence was observed for $\langle p_t \rangle$ fluctuations/correlations attributed to minijets. The quadrupole data fall on a single two-parameter line for all collision systems. In Fig. 5.16-1 (second panel) we show values of rapidity shift Δy_t obtained from two-component spectrum analysis *vs* participant path length ν. The rapidity shift measures relative parton energy loss as $\Delta y_t \sim \Delta p_t/p_t \sim \Delta E/E$. Predicted relative energy loss $\Delta E/E$ for 10 GeV (solid curve) and 20 GeV (dashed curve) *vs* centrality are also plotted.

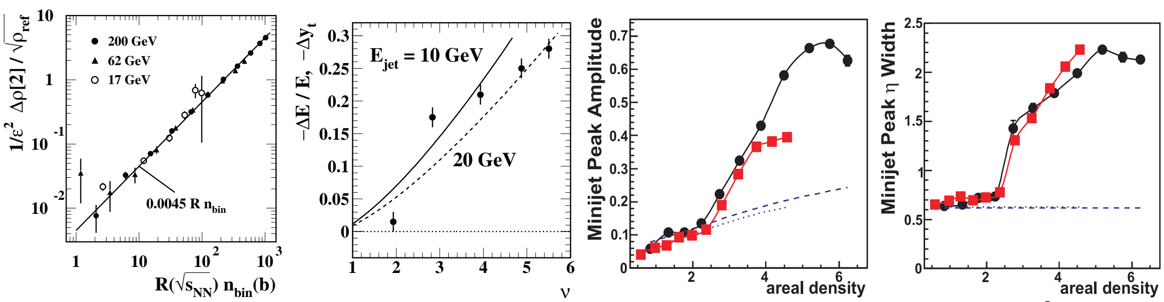

Figure 5.16-1. First panel: The azimuth quadrupole component divided by *optical* ϵ^2 *vs* energy-dependent factor $R(\sqrt{s_{NN}})$ times 200 GeV Au-Au binary-collision number $n_{bin}(b)$. The data are consistent with simple proportionality over three decades. Second panel: Hard-component negative boosts Δy_t for y_t spectra from five centralities of Au-Au collisions at 200 GeV (points) and theoretical predictions of relative energy loss $\Delta E/E$ for two parton energies (curves). Right panels: Minijet same-side peak amplitude and eta width *vs* Au-Au centrality in the form of areal particle density.

The energy-loss data trend appears to exhibit a step-wise transition near $\nu = 2.5$. The theoretical centrality dependence (curves) is $\Delta E/E \propto \nu^2$, roughly gluon density ($\sim \nu$) $\times$ outgoing parton pathlength ($\sim \nu$). The predicted magnitudes are close to the data, but there is no discontinuity mechanism contained in the theory. A step structure is also seen in minijet correlation peak systematics. Fig. 5.16-1 (right panels) shows same-side minijet peak amplitudes and widths from 62 and 200 GeV Au-Au collisions in which both peak amplitude and η width increase dramatically from p-p extrapolation (dashed curves) above a common tranverse particle density.

Taken together these systematics reveal that "elliptic flow" depends only on the initial-state A-A geometry (impact parameter b), not on any aspect of subsequent collision evolution (EoS, viscosity, chemistry, energy-loss medium). In contrast, other aspects of the final state indicate that a major transition in parton scattering and fragmentation does occur, possibly at a fixed transverse particle density. The quadrupole component apparently does not relate to a thermalization process or medium properties.

5.17 Energy and centrality dependence of the azimuth quadrupole for 62 and 200 GeV Au-Au collisions

D. T. Kettler and T. A. Trainor

2D angular autocorrelations provide undistorted access to two major phenomena in RHIC heavy ion collisions: minijets and the azimuth quadrupole (conventionally associated with "elliptic flow"). Autocorrelations on difference axes $(\eta_\Delta, \phi_\Delta)$ are fitted with model function

$$\frac{\Delta\rho}{\sqrt{\rho_{\rm ref}}} \quad\equiv\quad \frac{\Delta\rho_{\rm nf}}{\sqrt{\rho_{\rm ref}}}(\eta_\Delta,\phi_\Delta)+2\sum_{m=1}^{2}\frac{\Delta\rho[m]}{\sqrt{\rho_{\rm ref}}}\cos(m\phi_\Delta), \tag{1}$$

where the first term describes peaked distributions on pseudorapidity difference η_Δ, and the second term describes sinusoids on azimuth difference ϕ_Δ. The fitting results on centrality are shown in Fig. 5.17-1 (first panel). The second panel shows a remarkably simple energy dependence $\propto \log(\sqrt{s_{NN}})$ above 13 GeV *common to any A-A centrality.* The third panel shows the corresponding energy dependence for conventional measure v_2.

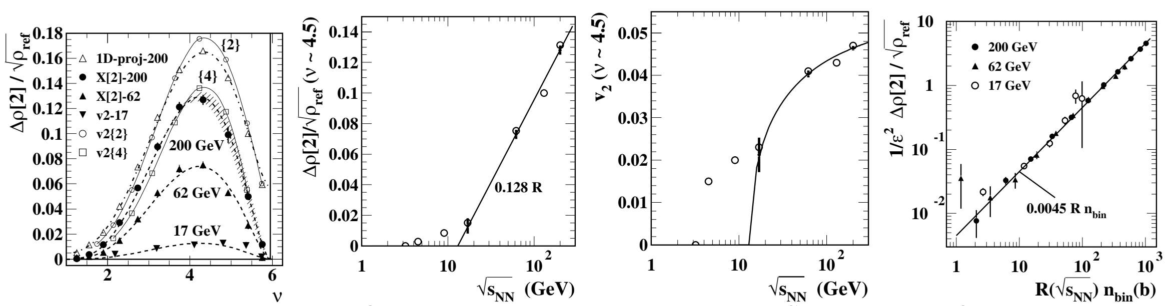

Figure 5.17-1. First panel: Quadrupole amplitude *vs* centrality. Second panel: Quadrupole energy dependence. Third panel: v_2 energy dependence. Fourth panel: Combined quadrupole energy and centrality systematics.

Fig. 5.17-1 (fourth panel) shows the linear relation satisfied by quadrupole data

$$\frac{\Delta\rho[2]}{\sqrt{\rho_{\rm ref}}}(n_{bin},\sqrt{s_{NN}}) \quad=\quad A\,R(\sqrt{s_{NN}})\,n_{bin}\,\epsilon^2_{\rm opt}(n_{bin}). \tag{2}$$

The common linear relation from N-N to central Au-Au argues against a bulk-medium hydro phenomenon, and there is no sensitivity to an EoS. Those results are inconsistent with the LDL expectation that ϵ and v_2 are related by the number of in-medium collisions during thermalization with transition to ideal-hydro trend $v_2/\epsilon \sim 0.2$ for central collisions and large collision energies. Instead, all initial- and final-state azimuth quadrupole moments are accurately related to *mean participant path length* ν.

The quadrupole component seems to be determined by initial-state QCD interactions leading to simple scaling with $\log(\sqrt{s_{NN}})$ and interaction path length ν. The product $R(\sqrt{s_{NN}})\,\nu(b)$ could represent the integrated relative flux of two QCD field components with energy-dependent coupling. The quadrupole component may thus represent an elementary QCD field interaction describing radiation from extended interaction of QCD fields.

5.18 Misidentification of minijets as v_2 ("elliptic flow") fluctuations

T. A. Trainor

Flow fluctuations have generated considerable recent interest. While the absolute relation of v_2 to hydro modeling may be uncertain, *relative fluctuations* might confirm event-wise thermalization ($v_2 \propto \epsilon$). But if flow fluctuations are shown to be negligible then the conventional ideal-hydro flow scenario could be threatened. v_2 fluctuations are inferred from the "Q-vector" distribution, given in terms of $\tilde{q}_2 \equiv \tilde{Q}_2/\sqrt{n}$ in simplified form by

$$\frac{dn}{d\tilde{q}_2^2} \propto \exp\left\{-\frac{\tilde{q}_2^2}{1+g_2(\nu,n)+2n\sigma_{v_2}^2}\right\}. \tag{1}$$

It is assumed that any change in the width of Eq. (1) with *random track discard* isolates v_2 variance $\sigma_{v_2}^2$, based on the assumption that "nonflow" term g_2 is approximately independent of multiplicity. However, systematic studies show that minijet correlations represented by g_2 decrease *linearly with random track discard*. Since the expected width trend from random discard for v_2 fluctuations is $2n\sigma_{v_2}^2$ and that measured for nonflow is $g_2 \propto n$ one cannot distinguish $g_2/2n$ from $\sigma_{v_2}^2$ by random discard.

Recent studies of flow fluctuations emphasized the relation of v_2 fluctuations and eccentricity fluctuations, and the trend $\sigma_{v_2}^2/v_2^2 \sim \sigma_\epsilon^2/\epsilon^2$ has been claimed. The apparent relation $\sigma_{v_2}^2/v_2^2 \sim \sigma_\epsilon^2/\epsilon^2$ results from two misconceptions: 1) the trend identified as $\sigma_{v_2}^2/v_2^2$ reflects a simple relation between the final-state momentum quadrupole component and the initial-state spatial quadrupole moment unrelated to fluctuations, and 2) the quantity identified as $\sigma_\epsilon^2/\epsilon^2$ models the small-x parton distribution as point-like nucleons and NSD N-N collisions as point-like nucleons acting at a distance. From our recent quadrupole measurements $\Delta\rho[2]/\sqrt{\rho_{ref}} \sim 0.005\, n_{bin}\, \epsilon^2$ and the measured $v_2\{2\}-v_2\{4\}$ difference we obtain the nonflow relation $g_2 \sim 2\pi\, 0.005\nu$. If we misidentify the nonflow term as $g_2/2n \rightarrow$"$\sigma_{v_2}^2$" and ignore $O(1)$ constant factors we obtain

$$\begin{aligned} \frac{``\sigma_{v_2}^2"}{v_2^2} &= \frac{2\pi\, 0.005\nu}{2n\, v_2^2} \\ &= \frac{0.005\nu}{2\Delta\rho[2]/\sqrt{\rho_{ref}}} \\ &= \frac{\nu}{2\, n_{bin}\, \epsilon^2} \\ &\sim \frac{1}{n_{part}\, \epsilon^2}. \end{aligned} \tag{2}$$

But since the participant-weighted eccentricity variance for Poisson statistics is "σ_ϵ^2" $\equiv \sigma_\epsilon^2\{n_{part}\} \sim 1/n_{part}$ it follows that "$\sigma_{v_2}^2$"$/v_2^2 \sim$ "σ_ϵ^2"$/\epsilon^2$. Thus, if the minijet contribution denoted $g_2/2n$ is misinterpreted as "$\sigma_{v_2}^2$" and low-x partons are modeled by point-like nucleons, v_2 data and Monte Carlo Glauber seem to support an event-wise $v_2 \propto \epsilon$ connection between initial and final states, consistent with ideal hydro expectations.

5.19 Relation between "event-plane" elliptic flow analysis and two-particle azimuth correlations

D. T. Kettler and T. A. Trainor

To interpret quadrupole measurements we must establish relevant algebraic relationships. The basic measures of sinusoidal azimuth correlations are the Fourier power spectrum elements V_m^2. The 2D p_t-integrated quadrupole term V_2^2 can be generalized to a p_t-differential form with unit vectors $\vec{u}(2\phi_i)$. $V_2^2(p_{t1}, p_{t2}) \equiv \sum_{i \in p_{t1} \neq j \in p_{t2}=1}^{n_{p_{t1}}, n_{p_{t2}}} \vec{u}(2\phi_i) \cdot \vec{u}(2\phi_j) \equiv \vec{V}_2(p_{t1}) \cdot \vec{V}_2(p_{t2})$, where index p_{t1} labels a histogram bin of width δp_t with center at p_{t1} containing $n_{p_{t1}}$ particles. *Marginal* distribution $V_2(p_t)$ is obtained by integrating $V_2^2(p_{t1}, p_{t2})$ over one p_t axis

$$\begin{aligned} V_2^2(p_t) &\equiv \sum_{i \in p_t \neq j=1}^{n_{p_t}, n-1} \vec{u}(2\phi_i) \cdot \vec{u}(2\phi_j) \\ &= \vec{V}_2(p_t) \cdot \vec{V}_2 \\ v_2\{2\}(p_t) &\equiv \frac{V_2(p_t) \cdot \vec{V}_2}{n_{p_t} V_2}. \end{aligned} \tag{1}$$

The last line defines conventional flow measure $v_2\{2\}(p_t)$ in terms of two-particle correlations.

The differential amplitude ratio $q_2(p_t)$ can be obtained by inverting the Fourier series

$$\begin{aligned} q_2(p_t) &= \langle \vec{u}(2\phi_{i \in p_t}) \cdot \vec{u}(2\Psi_2[p_t]) \rangle \\ &= \frac{\vec{Q}_2(p_t)}{n_{p_t}} \cdot \frac{\vec{Q}_2(p_t)}{Q_2(p_t)} = \frac{Q_2(p_t)}{n_{p_t}}. \end{aligned} \tag{2}$$

According to standard methods $\vec{Q}_2(p_t)/Q_2(p_t) \to \vec{Q}_2/Q_2 = \vec{u}(2\Psi_2)$ to give the event-plane angle, and "autocorrelations" (self pairs) are eliminated from the dot product. For each particle i $\vec{Q}_2 \to \vec{Q}_{2i}$ is formed by omitting the i^{th} particle from the $\vec{Q}_2$ sum over j to obtain

$$\begin{aligned} v_{2obs}(p_t) &= \langle \vec{u}(2\phi_{i \in p_t}) \cdot \vec{u}(2\Psi_{2i}) \rangle \\ &= \left\langle \frac{\vec{Q}_2(p_t)}{n_{p_t}} \cdot \frac{\vec{Q}_{2i}}{Q_{2i}} \right\rangle \\ &\approx \frac{\vec{V}_2(p_t) \cdot \vec{V}_2}{n_{p_t} \langle Q_{2i} \rangle}, \end{aligned} \tag{3}$$

where the $\vec{V}_2$ dot product defined in Eq. (1) represents the double sum with $j \neq i$. v_{2obs} is then divided by the "event-plane resolution" $\langle \cos(2[\Psi_2 - \Psi_r]) \rangle$ to obtain

$$\begin{aligned} v_2\{EP\}(p_t) &\equiv \frac{\langle \vec{u}(2\phi_{i \in p_t}) \cdot \vec{u}(2\Psi_{2i}) \rangle}{\langle \cos(2[\Psi_2 - \Psi_r]) \rangle} \\ &= v_2\{2\}(p_t) \cdot \frac{V_2/\langle Q_{2i} \rangle}{\langle \cos(2[\Psi_2 - \Psi_r]) \rangle}, \end{aligned} \tag{4}$$

which gives the exact relation between $v_2\{EP\}$ and $v_2\{2\}$ in terms of the $O(1)$ second factor. The difference between $\{EP\}$ and $\{2\}$ results from a misconception about the v_{2obs} numerator leading to introduction of $\langle Q_{2i} \rangle \sim Q_2$ in the denominator of Eq. (3) in place of V_2 as in Eq. (1) (last line).

5.20 Resonstructing azimuth quadrupole y_t spectra from $v_2(p_t)$ data

T. A. Trainor

From $v_2(p_t)$ data we can infer the associated quadrupole spectrum using $\rho_0(y_t;T_0,n_0)\,v_2(p_t) = p_t'/2T_2 \cdot f(y_t)\,\Delta y_{t2}\,\rho_2(y_t;\Delta y_{t0},T_2,n_2)$, where $\rho_0(y_t)$ is the single-particle spectrum, and $\rho_2(y_t)$ is the quadrupole spectrum. Fig. 5.20-1 (left panel) illustrates how to match $\rho_0(y_{t\pi})$ parameterizations to $v_2(p_t)/p_t$ data. Single-particle spectra in the form $2/n_{part} \cdot \rho_0(y_{t\pi})$ for three hadron species are given by the dotted curves. The open symbols show the specific values of ρ_0 for each v_2 datum and hadron species. The solid symbols show the corresponding values of $2/n_{part} \cdot \rho_0(y_{t\pi})\,v_2(p_t)/p_t$. The dashed curves show the result of modeling the $v_2(p_t)$ data with boosted soft component S_{NN}' (Lévy distribution). The solid curves show the quadrupole spectra in the form $\gamma_t(1-\beta_t)/2T_2 \cdot\ f(y_t)\,2/n_{part}\,\Delta y_{t2}\,\rho_2(y_t)$.

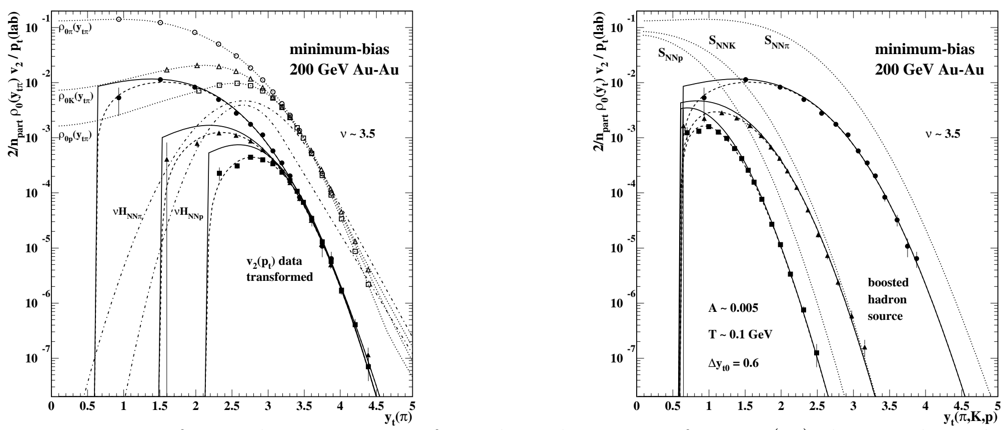

Figure 5.20-1. Left panel: Formation of quadrupole spectra from $v_2(p_t)$ data and single-particle spectra. The open symbols are the values of $\rho_0(y_t)$ used for the conversion. The solid symbols are the resulting approximations to quadrupole spectra. Right panel: Spectra from the left panel transformed to proper y_t for each hadron species. The dotted curves are soft components from respective single-particle spectra for comparison. The hadron abundances and spectrum shapes are the same as the single-particle spectrum soft components.

Fig. 5.20-1 (right panel) shows data (solid points) from the left panel transformed to $y_t(\pi,K,p)$ (proper y_t for each hadron species) with the appropriate Jacobians. The common left edge reveals monopole boost $\Delta y_{t0} \simeq 0.6$. The *form* of the data is $\propto p_t'/p_t\ \cdot f(y_t) \cdot \rho_2(y_t;\Delta y_{t0})$, the last factor being the quadrupole spectrum.

The quadrupole spectrum for each hadron species can be modeled with the same form of Lévy distribution used for the soft component of the single-particle spectrum. Also plotted in Fig. 5.20-1 (right panel) are soft components $S_{NNX}(y_t)$ from the single-particle spectra for three hadron species (dotted curves). The dashed curves through data points are $A/T_2 \cdot p_t'/p_t\,\gamma_t(1-\beta_t) \cdot S_{NN}'(y_t - \Delta y_{t0};T_2,n_2)$, with factor A and monopole boost Δy_{t0} common to the three species. The factors are $A/T_2 \sim 0.005/(0.1\text{ GeV}) \sim 1/20\text{ GeV}^{-1}$. The description of data is good. The solid curves are the same but with factor $p_t'/p_t\gamma_t(1-\beta_t)$ removed, revealing the undistorted shapes of quadrupole spectra $\rho_2(y_t,\Delta y_{t0})$. Comparison with the single-particle soft spectrum components (dotted curves) reveals the similarities of the single-particle soft and quadrupole hadron sources.

5.21 Detailed comparisons of quadrupole spectra and hydro models

T. A. Trainor

By a simple data transformation it is possible to provide detailed comparisons of hydro theory predictions to $v_2(p_t)$ data, especially regarding boost distributions. Fig. 5.21-1 (first panel) illustrates the essential features of "elliptic flow" measurements with $v_2(p_t)$ data for three hadron species. The mass trend at small p_t is a kinematic effect true for any boosted hadron source independent of boost mechanism (i.e., hydrodynamics is not required). $v_2(p_t)$ includes the ratio of two single-particle densities, a boosted soft component $S'_{NN}(y_t - \Delta y_{t0})$ (numerator) and the single-particle spectrum (denominator). Typical hydro models do not include a hard component. The spectrum ratio is then $S'_{NN}(y_t - \Delta y_{t0})/S_{NN}(y_t) \sim \exp\{-\gamma_t(m_t - \beta_t\, p_t)/T_2\}/\exp\{-m_t/T_0\}$, where γ_t, β_t are determined by monopole boost Δy_{t0}. Fig. 5.21-1 (second panel) shows typical hydro spectrum ratios for three hadron species.

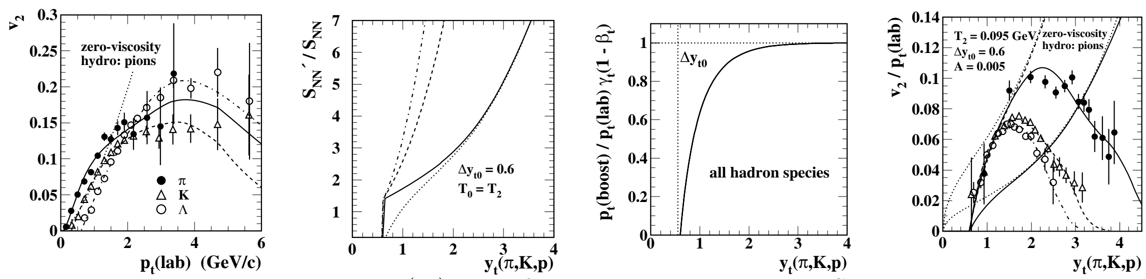

Figure 5.21-1. First panel: $v_2(p_t)$ data for three hadron species. Second panel: Hydro theory spectrum ratios plotted on proper y_t for each hadron species. Third panel: A common kinematic factor for boosted sources plotted on proper y_t for each hadron species. Fourth panel: Ratio $v_2(p_t)/p_t$(lab) plotted on proper y_t for each hadron species.

Fig. 5.21-1 (third panel) relates $p'_t = m_0 \sinh(y_t - \Delta y_{t0})$ (p_t in the boost frame) to transverse rapidity $y_t(\pi, K, p)$. The dotted curves in first and fourth panels represent a zero-viscosity hydro calculation for pions interpreted to support claims for formation of a "perfect liquid" in RHIC collisions. The dotted curve in the second panel, including additional factor $p'_r/p_t\gamma_t(1 + \beta_t)$, is within a constant factor the solid curve in the fourth panel. In Fig. 5.21-1 (fourth panel) the solid curve following the hydro dotted curve at larger y_t is $B\, p'_t/p_t \cdot S'_{NN}(y_t - \Delta y_{t0})/S_{NN}(y_t)$ (dotted curve in the second panel). B was adjusted to match the hydro theory (lower dotted) curve at larger y_t. Agreement of the shapes is good except near the origin where the *boost distributions differ*. The dashed and upper dotted curves in the right panel are 2.7× the solid and hydro curves. The dashed curve describes the data for three masses well in the smaller-y_t region where the hard component does not dominate the variation.

The structure in $y_t \leq 1.5$ is possibly the first *direct* comparison of boost distributions from data and hydro theory. Boost comparisons provide essential tests of hydro and the expanding bulk medium scenario for heavy ion collisions. Boost details are strongly suppressed in plots of $v_2(p_t)$ *vs* p_t (first panel). The data indicate a narrow boost distribution centered at $\Delta y_{t0} = 0.6$. The hydro prediction suggests a broad distribution starting at $y_t = 0$ and roughly consistent with Hubble expansion of a bulk medium. Inferences of small (or any) viscosity from comparisons of $v_2(p_t)$ data with the lower dotted curve are not justified.

5.22 Falsification of so-called "consitutent-quark number (n_q) scaling" conventionally inferred from $v_2(p_t)$ data

T. A. Trainor

"Constituent-quark scaling" of $v_2(p_t)$ data is used to support inferences of a small-viscosity thermalized bulk partonic medium in RHIC collisions. However, detailed analysis shows that any such scaling cannot be related to hydrodynamics or soft hadron production. In Fig. 5.22-1 (left panel) p_t' (p_t in the boost frame) is plotted on $m_t - m_0$, with source boost $\Delta y_{t0} \sim 0.6 \sim \gamma_t (1 - \beta_t)$ common to three hadron species. The mass dependence near the origin *appears* to be reduced from the p_t case, but the locations of the curve intercepts are simply given by $m_{t0} - m_0 = m_0(\cosh[\Delta y_{t0}] - 1) \sim m_0 (\Delta y_{t0})^2/2$ on $m_t - m_0$ compared to $p_{t0} = m_0 \sinh(\Delta y_{t0}) \sim m_0 \Delta y_{t0}$ on p_t. Evidence of the source boost is compressed on $m_t - m_0$ (by a factor 3 for $\Delta y_{t0} \sim 0.6$), but the boost is accurately determined from the data. In Fig. 5.22-1 (second panel) both axes are scaled by $2/n_q$. The intercept at smaller m_t is reduced by 2/3 for baryons, and the constant vertical offset m_0 at larger m_t is also reduced by 2/3 for baryons.

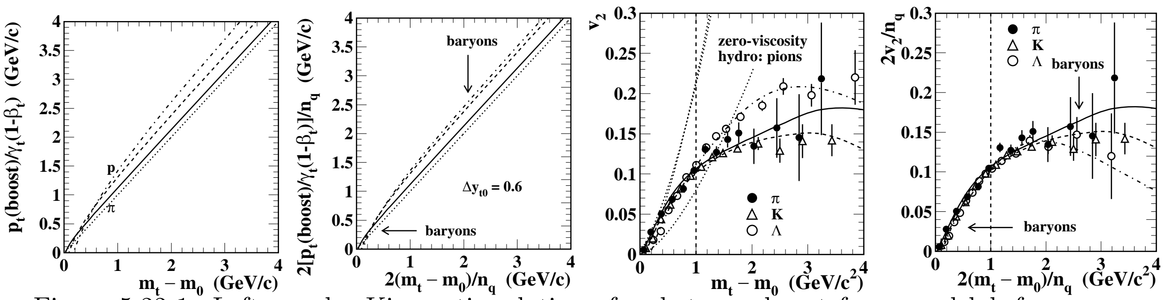

Figure 5.22-1. Left panels: Kinematic relation of p_t between boost frame and lab frame. Right panels: $v_2(p_t)$ data on $m_t - m_0$ without and with "constituent quark scaling."

Fig. 5.22-1 (third panel) shows $v_2(p_t)$ data for three hadron species plotted on $m_t - m_0$. Data near the origin follow the p_t' systematics in the first panel. Note the limited region of comparison between the upper hydro (dotted) curve and the data. The turnover of $v_2(p_t)$ above 0.5 GeV/c is due to the hard component (minijets) in the v_2 denominator. In Fig. 5.22-1 (fourth panel) the n_q scaling strategy is used to minimize apparent differences between baryon and meson data, the resulting shifts indicated by the arrows. The most dramatic changes occur above 1 GeV/c where the data are *not relevant to a hydrodynamic mechanism or soft processes.* In scaling exercises the region above 1 GeV/c is viewed as dominated by elliptic flow and soft hadronization. Scaling trends there are interpreted in turn to imply that hadron production is dominated by coalescence of constituent quarks. The apparent correspondence of data for different hadron species left of the vertical dotted lines indicates that all-important information about the source boost distribution is *visually inaccessible.* v_2 data to the right of the vertical dashed lines are dominated by a complex mixture of hard processes (parton scattering and fragmentation), soft spectrum components and quadrupole components. Inference of "constituent quark scaling" from v_2 data is derived from a combination of several conventional collision mechanisms confused by a poorly-designed correlation measure.

5.23 Is "elliptic flow" a manifestation of initial-state gluonic radiation?

T. A. Trainor

The quadrupole component of azimuth correlations, interpreted as "elliptic flow," is seen as confirming the creation of a thermalized bulk partonic medium in central RHIC Au-Au collisions. However, a number of recent results suggest that the hydrodynamic interpretation of the quadrupole is incorrect. Taking those results together suggests that the azimuth quadrupole may be a manifestation of gluonic radiation.

The hydro sequence *parton scattering* $\rightarrow$ *fast thermalization* $\rightarrow$ *flow with EoS* $\rightarrow$ *hadronization* provides one scenario for large-scale phase-space transport. But there appears to be insufficient time with known microscopic processes to unpack the nuclear wave function, equilibrate the results, flow them and reconstitute them into hadrons in the observed final state. In a viscous hydro model the viscosity-to-entropy ratio η/s as a model parameter is driven to very small values in attempts to describe data. But does that imply a real medium with very small viscosity (perfect liquid) or an inappropriate physical model?

We have recently observed that 200 GeV Au-Au p_t-integrated v_2 data are consistent with

$$\begin{array}{rcl} \Delta\rho[2]/\sqrt{\rho_{ref}} & \approx & A\, n_{bin}\, \epsilon^2 \\ \text{or} \quad \bar{n}_{ch} v_2^2/2\pi & \approx & \pi A\, \nu(b)\, \{n_{part}(b)\, \epsilon^2(b)/2\pi\}, \end{array} \tag{1}$$

where the curly bracket on the RHS represent the per-particle quadrupole moment of the source, and the LHS is the per-particle quadrupole moment of final hadrons. Eq. (1) suggests that all p_t-integrated quadrupole systematics are described by one or two parameters representing the initial A-A system. There is no apparent sensitivity to intervening collision dynamics, no need to invoke a hydrodynamic scenario, equation of state or medium properties such as viscosity. The quadrupole may be completely determined by the initial small-x parton (glue-glue) interaction. We also know from minijet studies that flow fluctuations are much smaller than previously claimed and presently consistent with zero. The absence of measurable flow fluctuations hints at the true transport mechanism, a simple relation between the hadronic quadrupole component and initial collision geometry defined by small-x gluonic *field* interactions.

Parton interactions at larger energy scales are modeled in pQCD as point-like interactions. However, near the gluon saturation energy scale QCD interactions may extend over a significant space-time volume—the "partonic participants" (interacting fields) may even extend across the nuclear diameter. In a generalization of the pQCD parton-parton vertex to non-pQCD interactions over extended space-time volumes the interaction strength should be the product of a cross section and a *relative* current density, a space-time current autocorrelation. Such an interaction would be consistent with Eq. (1), provided an energy-dependent factor is incorporated. The alternative to "elliptic flow" may be an extended field-field interaction representing a generalization of pQCD. A radially expanding gluonic field might *appear* as a flow field, and some hydrodynamic properties (e.g., viscosity) could be ascribed to it. But "elliptic flow" could be a manifestation of gluonic quadrupole radiation.

5.24 Updates to the STAR online QA system

D. T. Kettler

The STAR QA system is used to actively monitor data being taken by the various subcomponents of the detector in order to ensure that they are working properly and that the data are valid. QA can be divided into two components: online QA and offline QA. Online QA is what the shift crew monitors while actively taking data, and the offline QA is a more detailed analysis which is conducted in QA shifts on data that have already been taken. The importance of online QA is that while offline QA can be used to mark runs as bad it is less useful for noticing and responding to detector problems as they occur.

As the STAR detector itself evolves the software must be updated and improved along with it. I was placed in charge of maintaining this system starting in Run 8. Though most software development can be done remotely I worked closely with Paul Sorensen, Jeff Landgraf, and Valeri Fine at BNL.

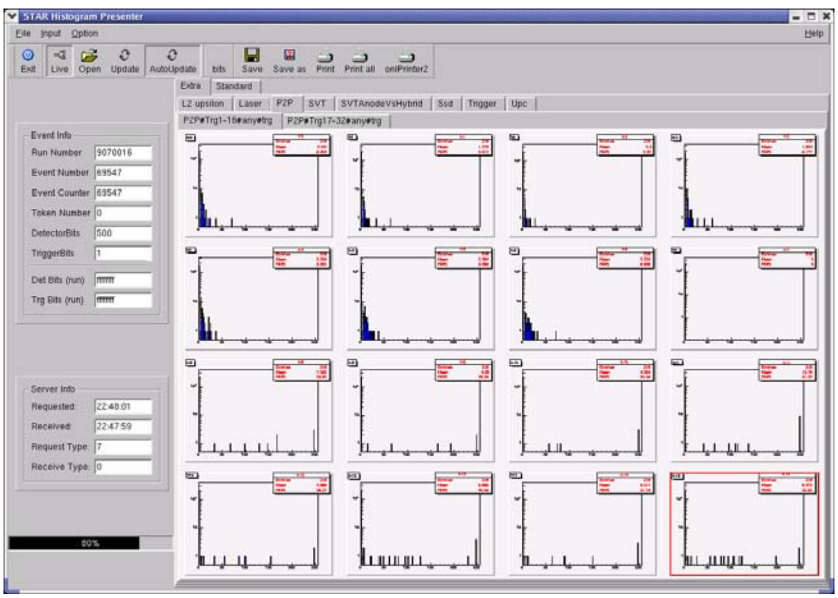

Figure 5.24-1. Example of plots in the online QA client software

Updates to the online QA system since the beginning of Run 8 in November included new plots for the forward meson spectrometer (FMS) and time of flight (TOF) detectors as well as some additional plots requested by the pp2pp experiment. There were also updates to the laser drift velocity algorithm, and some obsolete plots were removed.

In addition to software development it is also necessary to perform maintenance tasks. In February there was a hard drive failure on the computer running the online QA system, which necessitated a rebuild of the whole system and regeneration of plots from data that were missed during the down time.

5.25 Relativistic Heavy Ion Physics-Analysis of Pionic Interferometry: the DWEF Model

J. G. Cramer, G. A. Miller,* and M. Luzum†

In relativistic heavy ion collisions it is usually assumed that the pion source resulting from the collision is cylindrically symmetric around the beam axis and is transparent to emitted pions. Thus the detector should receive particles from all kinematically-allowed regions of the source. This leads to a prediction that the radius parameter toward the detector, R_O, is larger than the corresponding radius perpendicular to the detector, R_S, for particles of zero rapidity: $R_O^2 \approx R_S^2 + \beta_0^2 \delta\tau^2$, with $\delta\tau$ the duration of pion emission, and β_0 is the pion velocity in the direction of the detector. However, HBT radii extracted from measured two-particle momentum correlation functions indicate that for Au+Au collisions at RHIC, R_O is approximately equal to R_S. These observations contradict theoretical expectations and have been taken as an indication that the emission duration may be extremely short, i.e. the source freezes out quite suddenly.

To avoid this scenario, Heiselberg and Vischer[1] proposed that the source should be treated as opaque rather than transparent to pions. Their study, as well as a more detailed one by Tomasik and Heinz,[2] showed that an opaque source would lead naturally to R_O smaller than R_S for plausible emission durations. However, both of these studies used the high energy limit and the semi-classical (eikonal) approximation to treat the pions emerging from the source. This procedure cannot be justified for the pions of momenta of a few hundred MeV/c used in the experimental correlation studies.

We have handled the effects of opacity and refraction by using an optical potential and solving quantum mechanical wave equations for the pions in a highly dense medium, using a relativistic, complex optical model potential consistent with the constraints of chiral symmetry. Our first results[3] presented a relativistic quantum mechanical treatment of opacity and refractive effects that allows reproduction of observables measured in two-pion (HBT) interferometry and pion spectra at RHIC. The net result is that the emission of pions produced within a dense, strongly-interacting system of matter in the presence of strong radial flow is described using a relativistic optical model formalism. The result is a distorted-wave emission function model (DWEF).

During the past three years we continued the studies of the HBT effects of final state interactions. We detailed our formalism[4] so that others can use it, explained why the eikonal approximation is inadequate to handle HBT physics for pions of momentum of less than 1 GeV/c, and extended our analysis to cover HBT measurements made at AGS and SPS energies as well as the lower energy RHIC data. Fig. 5.25-1 shows our latest fits to the STAR

---

*supported by the UW Nuclear Theory DOE Contract

†UW Nuclear Theory Grad. Student

[1]H. Heiselberg and A. P. Vischer, Eur. Phys. J. C **1**, 593 (1998).

[2]B. Tomasik and U. W. Heinz, arXiv:nucl-th/9805016.

[3]J. G. Cramer, G. A. Miller, J. M. S. Wu, and J.-H. Yoon, Phys. Rev. Lett. **94**, 102302 (2005).

[4]Gerald A. Miller and John G. Cramer, Journal of Physics G **34**, 703-739 (2007).

HBT data[5] for central Au+Au collisions at $\sqrt{S_{nn}}$ =200 GeV.

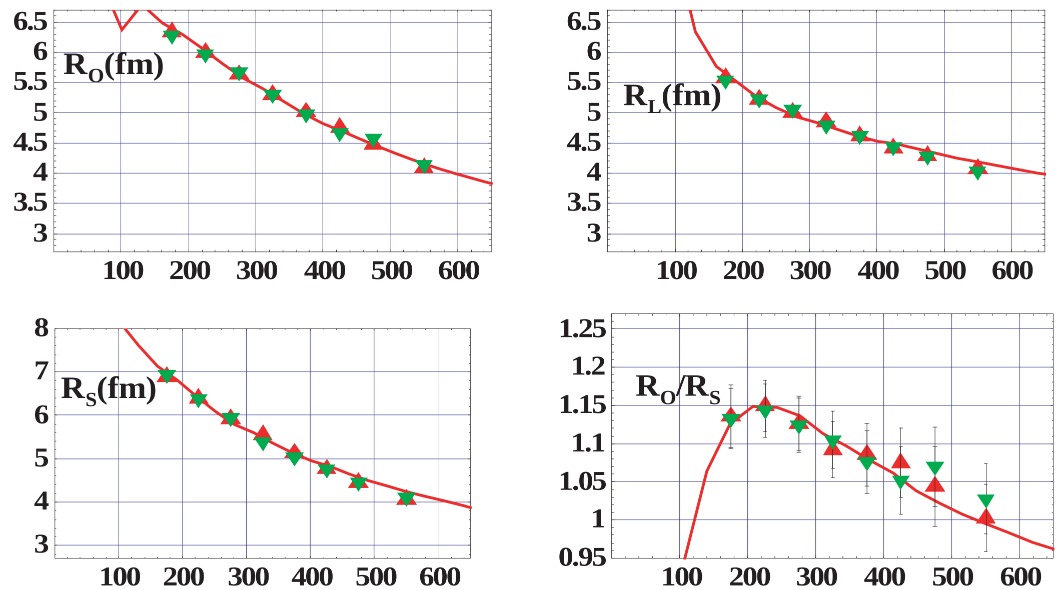

Figure 5.25-1. (Color online) STAR HBT Radii $R_s, R_o,$, R_l and the ratio R_o/R_s for Au+Au at $\sqrt{s_{nn}}$ = 200 GeV; Data: (see Ref. 5) ∇ (green) $\Rightarrow \pi^+\pi^+$; $\triangle$ (red) $\Rightarrow \pi^-\pi^-$. Curves: solid (red) DWEF fit to these data

We also studied kaon HBT correlations to determine any necessary final state interactions and to test our formalism. So far the results are inconclusive as the value of the parameter λ which governs the size of the KK correlation function is very small and not well enough known for us to simultaneously compute the kaonic spectrum and HBT radii.

So far we have concentrated on central collisions, but we intend to extend our formalism to study the impact parameter dependence. This is being done by M. Luzum who explicitly solves the Klein-Gordon equation when the optical potential has the famous walnut shape.

[5] J. Adams, *et al.* [STAR Collaboration], Phys. Rev. C **71**, 044906 (2005).

6 Electronics, Computing, and Detector Infrastructure

6.1 Electronic Equipment

G. C. Harper, A. W Myers, and T. D. Van Wechel

The electronics shop personnel provided normal maintenance and repair on all laboratory electronics equipment in support of all experiments conducted at CENPA. Other projects undertaken by the electronics shop include the following.

1. Development work continued on the parametric amplifier. This project has been discontinued owing to its expanding complexity.
2. Design and construction of the External Alpha Counter for the NCD Array at SNO was completed.
3. Modifications and improvements were made to the KATRIN electron gun (see Sec. 1.13).
4. Several projects were undertaken for the KATRIN experiment (see Sec. 1.7).
5. Designed and built a test chamber for KATRIN Prototype Detector Tests (see Sec. 1.12).
6. Designed and built an interface between the AUGER Crate electronics on loan from FZK Germany and the Neutron TPC experiment at LBNL for data taking.
7. Constructed a PID Controller for the ^{3}He + ^{4}He experiment.
8. Built several controllers to switch optics from the 0° beam line to the 45° beam line for the ^{22}Na(p,γ) experiment.
9. Upgraded the Electronics Shop capabilities with the addition of a Ball Grid Array (BGA) surface mount soldering and inspection system

6.2 Additions to the ORCA DAQ system

M. A. Howe and M. G. Marino

The Object-oriented Real-time Control and Acquisition (ORCA) system is an application software tool-kit that is designed for quickly building flexible and robust data acquisition systems. The world-wide base of installed ORCA systems continues to grow, with the most recent additions including the nTPC experiment at Livermore Labs, a Majorana development test stand at Los Alamos, a Tritium source development system at FZK, two FZK IPE hardware development test stands, and the KATRIN pre-spectrometer at FZK. At CENPA, ORCA continues to be used in several test stands for the development of the KATRIN pre-spectrometer (see Sec. 1.7) and the Majorana electronics (see Sec. 1.22). Since ORCA has been described extensively in past annual reports[1] only the most recent developments will be reported here.

A number of improvements and additions were made to the ORCA infrastructure, including the release of an explorer object that enables rapid examination of the run headers of a group of data files. The Header Explorer is integrated with the existing Data Explorer so if a run is identified for more analysis, it can be immediately opened for a record-by-record examination of the raw data. Another important advance was the addition of single board computer support for VME, cPCI, and the IPE hardware (see Sec. 6.3) and the expansion of ORCA's data analysis capabilities to include a direct link to ROOT's function fitting and FFT routines. Finally, ORCA is now a universal application, which means that it can run on both PPC and Intel Macintoshes.

Support for a number of new hardware devices was implemented. New VME support includes the IP220 16 channel DAC, a VME64 crate object, the LBL Gretina 4 digitizer, an e-beam controller object, and the Concurrent Vx407 single board computer. For compact PCI hardware, the PCI crate and Acqiris digitizer objects were added. The set of objects that connect via a serial port was expanded to include the LakeShore 210 temperature monitor, the BOC Turbo Instrument 3 head controller, and the Ami 286 cryogenic level controller. Support for the new IPE KATRIN FLT and SLT version 4 cards has been started.

An important advance for ORCA was the development of a new scripting language called FilterScript. It is an interpreted language with a very small command set that can be used to write data filtering and simple event building routines right into ORCA. One of the primary design goals was to provide a C-like language that would be fast enough to filter a live data stream. FilterScripts are created and edited using the Data Filter object and are integrated into the ORCA data flow so that each data record causes the script to be executed once. Stacks are provided to allow the accumulation of events.

ORCARoot continues to be developed in lock-step with ORCA to fully support ROOT analysis of data from the new ORCA hardware objects.

[1] CENPA Annual Report, University of Washington (2001) p. 83; (2002) p. 81; (2003) p. 70; (2004) p.66; (2005) p.85; (2006) p.80; (2007) p.81.

6.3 ORCA support of single board embedded computers

M. A. Howe and M. G. Marino

ORCA (see Sec. 6.2) now supports the use of Linux-based single board computers (SBC) as crate controllers for VME, compact-PCI, and the FZK IPE v4 crates. In this general implementation, the code that runs on an SBC is split into two sections. One part is general and implements the low-level communication protocol, the socket connection, and all data transfer. The other part is specific to each type of hardware, i.e. VME, cPCI, or IPE. ORCA manages both sets of SBC code and assembles them automatically into a download package that is transfered to the SBC, compiled, and then started. An interface layer in ORCA makes the use of SBCs transparent and no legacy code needs to be modified to use an SBC controller.

On the SBC, the code is multi-threaded with one thread controlling hardware readout and the other controlling communication to ORCA. A circular buffer is used to move the data from the read-out thread to the ORCA communication thread. For data read-out, a small piece of read-out specific code needs to be written for each card. The hardware read-out order is set up by the user using ORCA.

Using a Concurrent Vx407 2.16GHz Core 2 Duo Intel SBC running Fedora Linux in a VME crate, speed tests were run to determine communication speeds between an ORCA DAQ computer and the SBC. To minimize packet loss and latency across the network the SBC and DAQ computers were directly connected. ORCA data packet sizes were modified and readout speeds recorded for the 100 Mb/s (1 Gb/s) network speed achieving a maximum readout speed of $\sim$ 11 MBytes/s ($\sim$ 80 MBytes/s).

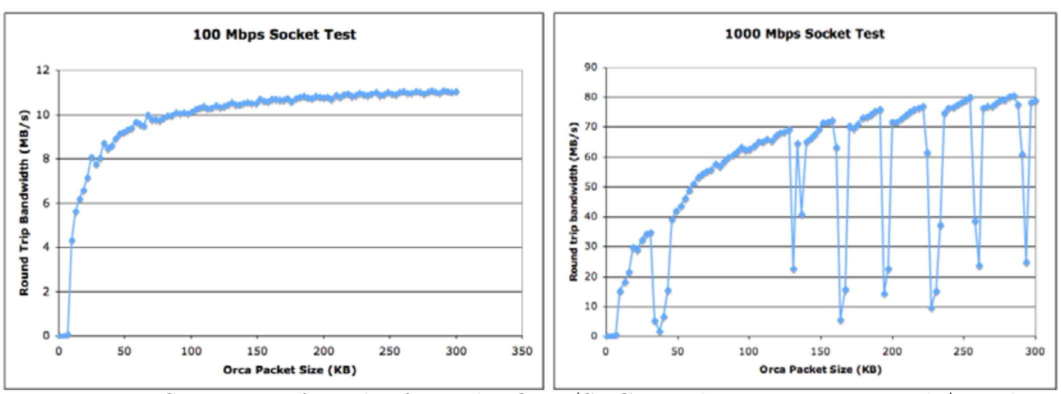

Figure 6.3-1. Summary of results from the Orca/SBC speed tests using 100 Mb/s and 1 Gb/s direct network connections.

As you can see in Fig. 6.3-1 the 1-GB/s network has a periodicity that is believed to be caused by ORCA packets that are slightly larger than a multiple of the network packet size, thus forcing the inclusion of a mostly empty record and incurring a large of amount of latency. ORCA has tools to map the transfer speed vs packet size, allowing the user to set the packet size to minimize latency.

6.4 Progress on the OrcaRoot analysis framework and development of near-time data display tools

J. A. Detwiler,* M. A. Howe, M. G. Marino, and J. F. Wilkerson

The OrcaRoot system is a cross-platform analysis framework designed to process ORCA (see Sec. 6.2) data streams using the ROOT toolkit. The user base of OrcaRoot continues to grow, including usage in KATRIN test stands at CENPA and FZK and MAJORANA test stands at Los Alamos and the University of Washington. Since OrcaRoot has been described in past annual reports[1] only recent and major developments will be outlined.

Several advances in the OrcaRoot framework have been made. For example, a buffered socket thread has been introduced to enable handling of large bursts of data coming over a socket stream. Thread safety has been implemented within the framework, opening the door for multi-threaded applications running one or more OrcaRoot data-processing engines. Both of these advances take significant advantage of multi-core systems common in modern computers. In addition, more robust signal catching has been implemented to allow synchronous handling of asynchronous signals. Support for handling the output from additional hardware continues to grow as new devices are implemented within ORCA.

A general ORCA-request processor has been implemented within OrcaRoot. An OrcaRoot server program can handle real-time requests from ORCA and return results immediately after processing to ORCA, giving access to the powerful analysis tools contained in the ROOT toolkit. A central OrcaRoot server can handle connections from multiple ORCA programs so that, for example, a set of laboratory DAQ machines can share the same server. Currently, fitting and Fourier transform processors have been created allowing these routines to be performed on plots in ORCA.

QtOrcaRoot, a cross-platform data display and online monitoring tool, couples the GUI framework of Qt with the data processing framework of OrcaRoot to enable graphical visualization of data in near- or real-time. QtOrcaRoot can run multiple, independent OrcaRoot processing threads each uniquely latched to a separate ORCA data stream. Display of data can be handled using Qt graphics widgets or the built-in Root widgets by using the ROOT Qt Extensions.[2] Plugin functionality enables the user to develop his or her own visualization tools and dynamically load them into the program at runtime. A number of basic plugins and examples have been developed. Successful testing has been performed on a number of systems, including Intel- and PowerPC-based Macintoshes and Linux machines.

*Currently at Lawrence Berkeley National Laboratory

[1] See e.g. CENPA Annual Report, University of Washington (2005) p. 85.

[2] See http://root.bnl.gov/QtRoot/QtRoot.html

6.5 Update on characterization of ultracold neutron detectors for use in the UCNA experiment at LANL

A. García, S. A. Hoedl, D. Melconian, A. L. Sallaska, and S. Sjue

Because of their reflective properties, detection of ultracold neutrons is challenging. We have fabricated converter foils of natural LiF and ^{10}B in combination with vanadium to use in conjunction with solid state detectors for the UCNA experiment at LANL, which is detailed in Section 2.9 of this report. These detectors were tested at the Institut Laue-Langevin (ILL) with a gravitational spectrometer setup, and both detectors and experimental setup have previously been described in detail.[1] A key element to and problem for any UCN experiment, however, is detecting the neutrons. In addition to being neutral, their energies are less than a few hundred neV, which causes them to reflect off a variety of materials at all angles of incidence. For UCN detection, solid state detectors coupled with charged particle converter foils are quite small, relatively simple to produce, and have a negligible background. However, neutrons will only be detected if they penetrate the surface (or surface window) of the detector. This will occur if the velocity of the UCN is greater than a "cutoff velocity," defined by the effective potential barrier of the foil.

The characterization experiment at the ILL was rigorously modeled with a Monte Carlo simulation in order to extract this cutoff velocity. The concept behind the gravitational spectrometer was to change the velocity distributions at the detector by altering the net gravitational barrier that the neutrons must overcome. Decreasing this barrier in turn decreases the minimum velocity needed to reach the detector. The results from the simulations yield a cutoff velocity of 365 cm/s for boron/vanadium and 314 cm/s for LiF. In trying to understand some of our results from our simulations, we uncovered mistakes in our code that were fixed. Presently the results from the simulation make sense, and we are finishing a paper with the details.

[1] CENPA Annual Report, University of Washington (2007) p. 50.

6.6 Laboratory computer systems

M. A. Howe, R. J. Seymour, H. E. Swanson, J. F. Wilkerson, and D. I. Will

This year was dominated by the conversion of our computer room to house the Athena cluster. This entailed the retirement of our two dual processor DEC Alpha 4000 systems, migration of printer, plotter and drafting support facilities to other rooms and some relocation of work activities. What had been a general user area become a sealed environment: Fig. 6.6-1. This was done while maintaining the usual background activity of additions, upgrades and replacements of existing desktop systems. See Secs 6.7 and 6.8.

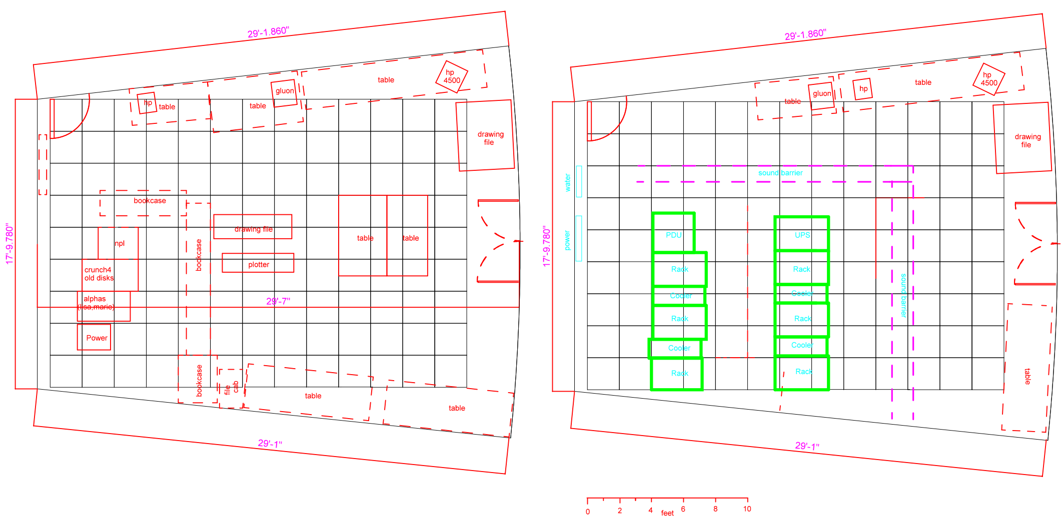

Figure 6.6-1. CENPA Computer Room before and after renovation

We are a mixed shop of Windows XP, Mac OS X and various flavors of Linux.
Windows Vista SP1 is installed on only one testbed.
Our Fedora-hosted 4 Terabyte SATA RAID system finally had its remaining eight slots filled with 320 MB disks bringing the total capacity to 6.5 TB.
We are now staging all daily Linux and Windows backups through one third of that system, from whence they are written to LTO tape by the Physics Computer Center.

Our computing and analysis facility consists of:
- The 1024-core Athena cluster as a shared resource with Physics, the Institute for Nuclear Theory (INT) and Astronomy Department.
- A mix of Linux systems, RedHat v7.3 through v9.0 and Fedora Core 6
- Three VMS/Vaxes and two VMS Alphas for "legacy" computing.
- The SNO, NCD, KATRIN and emiT groups rely upon Macintosh systems.
- One SunBlade 100 workstation serves CADENCE circuit design, analysis and layout duties.
- A VAXstation is the Linac and Vacuum systems' control and display system.
- Various WindowsXP desktop JAM acquisition and analysis systems, plus two laptops for taking to other installations.

• The bulk of CENPA's Windows-based PCs are behind a Gibraltar Linux-based logical firewall using an automated setup procedure developed by Corey Satten of the University's Networks and Distributed Computing group. http://staff.washington.edu/corey/fw/

• Although not directly used by Lab personnel, we provide co-location services for the INT and the Physics Nuclear Theory group in the form of one VMS Alphastation 500. The Astronomy Department has located a 64-processor Xeon-based Beowulf cluster in our old "counting" room.

6.7 The Athena Cluster

R. Amitai, J. Clark,* M. Clegg,* R. Coffey,† A. Jedlow,† M. MacAdam,† M. Mochkatel,‡ Z. Nazari,§ V. Peterson,¶ M. C. Reschke,‖ R. J. Seymour W. R. Somsky,† and D. I. Will

This year saw the installation of an approximately three teraFLOP (3 TF) computer cluster in our computer room. We are providing co-location, power and cooling, with on-site physical system management. Most of the "logical" system management is supplied by staff and faculty in the Institute for Nuclear Theory (INT), and the Departments of Physics and Astronomy.

The Athena eScience Cluster is a 128 node, 1024 core, Intel-based computational resource. Each node has 146GB of local SAS disk, 8GB of RAM, and two 2.33GHz Intel Quad-core based processors. It has a Cisco Infiniband DDR interconnect for all of the compute nodes. Finally, there is 45TB of local disk space provided by a Polyserve SAN available via NFS over a GigE backbone. The whole cluster is managed by Cluster Resources' Moab Cluster Suite and provides access to Intel's optimized compilers and toolkits for clusters and OpenMP.

The Infiniband infrastructure is a 4x DDR IB Cisco/TopSpin fabric capable of up to 16 Gbit/s bandwidth and 1.26 microsecond of latency. Currently the fabric is 33% non-blocking. OpenMPI and MVAPICH compiled for both Intel and gcc are available to broker communication over Infiniband. At this time, there is no plan to use IP over IB.

The Polyserve distributed file system provides a high-availablility file system for the Athena cluster. Sharing up both fiber channel and SATA disks, Polyserve makes it possible to achieve massive reads and writes from the cluster nodes to the disks. In addition, this software can support a distributed database system, something the Athena team will explore over the next year.

Power for the Polyserves and communication network is routed through a 16KW APC Symmetra LX UPS unit, which provides time for a controlled shutdown and proper closure and flushing of disk activity in the event of power failure or an environment-mandated shutdown.

As described in this report's Sec. 6.8, cooling is provided by four APC RC units serving as closed-loop heat exchangers to CENPA's accelerator's chilled water supply.

Power for the entire system is fed from a 225 amp feed from CENPA's 480 VAC substation. Under full compute load, the cluster uses roughly 45 KW of the available 80 KW of power.

The operating system is fundamentally Red Hat Enterprise Linux v4.5, with the compute

---

*Dell Corporation

†UW Physics

‡ECS

§UW Aeronautics & Astronautics

¶APC

‖UW Astronomy

nodes configured and reloaded as needed by the NSF-funded Rocks (www.rocksclusters.org) deployment system.

As of this writing, the cluster is in a “beta” stage of deployment. A (not very) limited group of users are running production jobs, but they are facing occasional interruptions of a single- or multiple-node basis as we shake out the job queuing system and memory allocation issues.

Moab and Torque, the workload management and resource management software enables a unique sharing method. Athena is shared by two departments and two institutes: CENPA, INT, Physics, and Astronomy. Allocation on the cluster is governed by “buy in” instead of distributing based upon computational hours. Users own segments of the cluster and have priority. However, all are welcome to the computational resource and can backfill while those cycles go unused.

The lifespan of the Athena cluster is estimated at 2 years for cutting edge science, 4 years before decommissioning. The service contract runs out in 2010, and hardware generally lasts 1-2 years after this contract winds down. CENPA expects that either the eScience group or interests within CENPA will continue to use the HVAC infrastructure for future high-performance computing related projects.

6.8 Cooling and electrical design for the Athena computer cluster

J. E. Alferness,* R. M. Coffey,* Z. Nazari,† R. J. Seymour, and D. I. Will

Initial cluster cooling and electrical design was based on Dell's[1] advertised power consumption of approximately 400 W for each of the 128 compute nodes. Power for disk storage, memory management and supervisory nodes, fast and slow networks, fan coils, power and control systems added about 10 kW bringing the grand total to roughly 60 kW consumption in the room. The building chiller reserve exceeds the room cooling load of 15 tons.[2] An APC[3] Power Distribution Unit (PDU) with integral stepdown transformer from 480 Vac 3 phase provides 160 kW (the smallest capacity available to safely handle 60 kW) 208 Vac 3 phase wye power at a distribution subpanel with computer monitoring and control of power systems. Computer room design specified 65F cold aisle and 100F hot aisle. The building chiller provides 50F water with reserve pump capacity exceeding the needed 60 gpm. At these temperatures each of the four APC RC units[4] provides 25 kW cooling while drawing 15 gpm chilled water. The four RCs together can cool 100 kW, substantially exceeding the 60 kW design.[5] UW Facilities Services installed plumbing and electrical service from our mechanical room.

Tests[6] of a sample node and of the nodes as actually delivered gave power consumptions of 380 W and 350 W, respectively.[7] The central PDU, which contains an accurate sampling power meter, indicates about 14 kW per phase for a total of 42 kW total consumption in the room under the maximum cluster load. This value implies a more accurate consumption for each compute node between 250 and 300 W. Tests of room temperature rate-of-rise and rate-of-recovery indicate that maximum cooling capacity at elevated hot aisle temperatures exceeds 100 kW. The building chiller load is difficult to measure. Under normal cluster operations it appears less than 20 tons total. These values are consistent with the design calculations. Total costs of electrical and plumbing upgrades (exclusive of APC items ordered through Dell) was roughly $ 100,000.

A multi-tiered environmental monitoring system was implemented to ensure proper function of supporting utilities for the cluster, especially room cooling. Primary monitoring and control is implemented using APC InfraStruXure environmental utilities and scripts to gracefully shut down the cluster if critical environmental conditions are exceeded. This system depends on network connectivity, so a second emergency shutdown system was developed to trip the primary PDU breaker if extreme environmental conditions are reached so that equipment is protected even if network connectivity should fail. The emergency system is a series circuit of three thermostats plus water sensing relays connected to a circuit breaker supplying the PDU transformer. Lastly, a phone monitoring system was installed and is monitored by ADT security who independently alert personnel at preset warning conditions.

*UW Physics
†UW Aeronautics & Astronautics

[1] Dell, Inc.
[2] CENPA Annual Report, University of Washington (2007) p. 86.
[3] American Power Conversion Corp.
[4] The RC is a rack-sized, half-width, in-row fan coil.
[5] Design was confirmed by APC's proprietary design program thanks to Vance E. Peterson of APC.
[6] Made with a non-sampling rms power meter prone to inaccuracy for switching power supplies.
[7] Discharge air temperatures met design specifications with internal node fans running at low speed.

7 Accelerator and Ion Sources

7.1 Van de Graaff accelerator and ion source operations and development

R. Amitai, G. C. Harper, A. W. Myers, T. D. Van Wechel, and D. I. Will

The tandem was entered twelve times this year. The terminal ion source (TIS) extractor supply was either replaced or repaired during three openings. Gas bottles of ^{4}He and $^1H_2$ were installed in the TIS manifold during one opening. The internal TIS parts were replaced during one extended opening in which the plasma bottle and boron-nitride insulator were broken. The accelerator tube gradient for single ended use was changed during two openings. Four openings were devoted to switching the accelerator configuration between single ended and tandem modes. An idler wheel in the low energy midsection was replaced during one opening. A faulty low energy georator circuit breaker was replaced during one opening.

This year there were no improvements made to either the DEIS or the model 860 SpIS, the two ion sources on the injector deck. Several ion beam test runs were performed with the SpIS to evaluate possible ion implantations. The SpIS was then used for eight ion implantation runs. The DEIS was used in conjunction with the tandem for two, short runs to make specific radioisotopes as gamma calibration sources.

During the 12 months from April 1, 2007 to March 31, 2008 the tandem pellet chains operated 630 hours, the SpIS 643 hours, and the DEIS 42 hours. Additional statistics of accelerator operations are given in Table 7.1-1.

ACTIVITY SCHEDULED	**DAYS SCHEDULED**	**PERCENT of AVAILABLE TIME**
Ion implantation, deck ion sources	32	9
Nuclear physics research, terminal ion source	63	17
Subtotal, ion implant or nuclear physics research	95	26
Machine development, maintenance, or crew training	54	15
Grand total	149	41

Table 7.1-1. Tandem Accelerator Operations April 1, 2007 to March 31, 2008

8 Outside User

8.1 Proton Induced APD displacement damage experiment

Andrew Huntington,* Madison Compton,* and George Soli*

Displacement damage experiment results for APDs (Avalanche Photo Diodes) exposed to protons at the Tandem Van de Graaff are presented. 2 MeV protons at a fluence of 1×10^{11} proton/cm^2 produce a measurable amount of displacement-damage dark-current as shown in Fig. 8.1-1. The damage mechanism is identified as bulk displacement damage and dark current increases for any space proton energy spectrum can now be computed for total fluences below 1×10^{11} proton/cm^2.

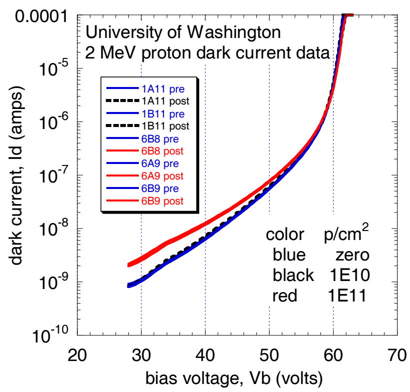

Figure 8.1-1. The measured damage factor is the measured change in dark current per change in fluence above the blue baseline for 1×10^{10} and 1×10^{11} protons/cm^2.

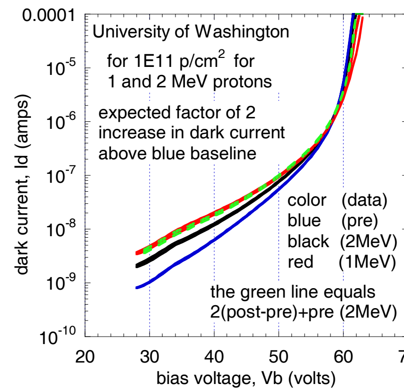

Figure 8.1-2. The dark current increases by a factor of 2, as the proton energy is lowered from 2 to 1 MeV. {[(post radiation)-(pre radiation)] x 2} + pre radiation for the 2 MeV data equal the 1 MeV data, and this shows that the measured damage factor changes as a function of proton energy as published in reference [1] in their Figure 1.

To adjust the dark current increase for 60 MeV protons, at the same fluence, just multiply the measured dark current change from the blue baseline to the red 1×10^{11} value by the published damage factor change of (0.067) shown in Figure 1 in reference [1]. We prove that these dark-current damage-factor transformations are possible in Fig. 8.1-2.

*Voxtel, Inc., 12725 SW Millikan Way, Suite 230, Beaverton, OR 97005.

[1]R. Reed, P. Marshall, C. Marshall, R. Ladbury, H. Kim, L. Nguyen, J. Barth, and K. LaBel, IEEE Trans Nucl Science, **47**, 42 (2000).

8.2 Status of the Career Development Organization

R. A. Johnson, M. L. Leber, M. G. Marino, N. S. Oblath, and B. L. Wall

The Career Development Organization has successfully completed its eighth year, once again lead by CENPA students. The seventh annual Networking Day was well received. Twenty-eight students participated, giving talks, posters and lab tours. Almost all of the past CDO presidents were in attendance, mostly as employer representatives. Five national labs attended in addition to three local companies and three international companies. At least one post-doc position was a result of the event, and a number of other students are in contact with the employer representatives.

Peripheral events of this year's Networking Day were the second annual employer talk session, a resume workshop given by UW's Career Services, and a growing website resource for students and employers. The employer talk session is open to all students, including departments outside physics. The employers discuss opportunities for physicists and related fields in their organizations. The resume workshop was tailored to physicists. Because of the workshop, the number and quality of student resumes available at Networking Day increased over past years. The website lists information about students and employers participating in Networking Day. Links to job listings and resources for students looking for employment are also available.

In addition to Networking Day, the CDO organizes lab tours, speakers and informational meetings for grad students. Officers of the CDO gain valuable leadership experience and many contacts outside the University. The continuity of Networking Day has strengthened our contacts and visibility. Past CDO presidents have maintained their commitment to CDO by attending as employers, and their organizations benefit. CENPA has always supported the CDO with storage space, office supplies, and donated printing.

Planning for next year's Networking Day and inquiries by employers have already begun. We hope the Networking Day continues to grow.

9 CENPA Personnel

9.1 Faculty

Eric G. Adelberger	Professor Emeritus
Hans Bichsel	Affiliate Professor
John G. Cramer	Professor
Peter J. Doe	Research Professor
Alejandro García	Professor
Jens H. Gundlach	Professor
Isaac Halpern	Professor Emeritus
Blayne R. Heckel	Professor
R. G. Hamish Robertson	Professor; Scientific Director
Leslie J. Rosenberg	Professor
Stephan Schlamminger[1]	Research Assistant Professor
Kurt A. Snover	Research Professor Emeritus
Derek W. Storm	Research Professor; Executive Director
Nikolai S. Tolich	Assistant Professor
Thomas A. Trainor	Research Professor
Robert Vandenbosch	Professor Emeritus
William G. Weitkamp	Research Professor Emeritus
John F. Wilkerson	Professor

9.2 CENPA External Advisory Committee

Baha Balantekin	University of Wisconsin
Russell Betts	University of Illinois at Chicago
Stuart Freedman	UC Berkeley

9.3 Postdoctoral Research Associates

Thomas Brown	Jessica Dunmore
Frank Fleischer[1]	Seth Hoedl
Daniel Melconian[2]	Brent VanDevender

[1] Not supported by DOE CENPA grant.
[2] Left during 2007; present address: Physics Dept, Texas A.& M. Univ, College Station, TX 77843-4242

9.4 Predoctoral Research Associates

Ted Cook[1]	G. Adam Cox-Mobrand[2]
Claire Cramer[3]	Prashant Siva Emani[1,4]
Charles Hagedorn[1]	Robert Johnson
David Kettler	Michelle Leber
Michael Marino	Noah Oblath
Anne Sallaska	Alexis Schubert
Sky Sjue	William Terrano[1]
Smarajit Triambak[5]	Matthew Turner[1]
Grant Volle[1]	Todd Wagner[1]
Brandon Wall	

9.5 University of Washington undergraduates taking research credit

Jacob Barnett	Erik Swanson, Advisor
Joseph Buchanan-Vega[6]	John Wilkerson, Advisor
Kseniya Deryckx	A. García, Advisor
Matthew Haefele	Ted Cook, Advisor
Holly Hess	Eric Adelberger, Seth Hoedl, Advisors
William Miao	Blayne Heckel, Claire Cramer, Advisors
Julie Michel	Hamish Robertson, Advisor
Andrew Palmer	A. García, Advisor
Natalie Ann Ramien	Nikolai Tolich, Advisor
Marissa Rodenburg	Nikolai Tolich, Advisor
Holgar Schweinfurther	Peter Doe, Advisor
Cosmo Smith	J. F. Wilkerson, Advisor
Levi Thomas	Tom Trainor, Advisor
Thomas Wolowiec	Leslie Rosenberg, Advisor

[1] Not supported by DOE CENPA grant.

[2] Ph.D., January, 2008. Presently at Forschungszentrum Karlsruhe, Institut für Kernphysik, Postfach 3640, D-76021 Karlsruhe, Germany

[3] Ph.D., October, 2007. Presently at Dept. of Physics, Harvard U., 17 Oxford St., Cambridge, MA 02138

[4] Left in 2007.

[5] Ph.D., May, 2007. Presently at Dept. of Physics, Univ. of Guelph, Guelph, Ontario, Canada, N1G 2W1

[6] Summer visitor in STAR program. Undergraduate at Grambling State University, Grambling, LA 71245

9.6 Professional staff

The professional staff are listed with a description of their recent major efforts.

John F. Amsbaugh	Research Engineer	Mechanical design, vacuum systems
Tom H. Burritt	Research Engineer	KATRIN design
Gregory C. Harper	Research Engineer	Electronic and mechanical design
Mark A. Howe	Research Engineer	Software for DAQ, control systems
Allan Myers	Research Engineer	
Duncan J. Prindle, Ph.D.	Research Scientist	Heavy ion software
Richard J. Seymour	Computer Systems Manager	
Hendrik Simons	Instrument Maker, Shop Supervisor	
H. Erik Swanson, Ph.D.	Research Physicist	Precision experimental equipment
Timothy D. Van Wechel	Electronics Engineer	Analog and digital electronics design
Douglas I. Will	Research Engineer	Cryogenics, ion sources

9.7 Technical staff

James Elms	Instrument Maker
David Hyde	Instrument Maker

9.8 Administrative staff

Victoria A. Clarkson	Administrator
Kate J. Higgins	Fiscal Specialist

9.9 Part time staff

Rahn Amitai
Cosmo Smith
Eugene Ngai

10 Publications

10.1 Published papers:

"Determination of the ν_e and total ^{8}B solar neutrino fluxes with the Sudbury Neutrino Observatory Phase I Data Set," B. Aharmim and the SNO Collaborators,* Phys. Rev. C **75**, 045502 (2007) arXiv:0610020 [nucl-ex].

"Search for the second-forbidden beta decay of ^{8}B to the ground state of ^{8}Be," M. K. Bacrania, N. M. Boyd, R. G. H. Robertson and D. W. Storm, Phys. Rev. C **76**, 055806 (2007) arXiv:0710.5197.

"The RHIC azimuth quadrupole: 'perfect liquid' or gluonic radiation?," T. A. Trainor, Mod. Phys. Lett. A **23**, 569 (2008) arXiv:0708.0792 [hep-ph].

"An array of low-background ^{3}He proportional counters for the Sudbury Neutrino Observatory," J. F. Amsbaugh and the SNO Collaborators,* Nucl. Instrum. Meth. A **579**, 1054 (2007) arXiv:0705.3665 [nucl-ex].

"The ^{3}He + ^{4}He $\rightarrow$ ^{7}Be Astrophysical S-factor," T. A. D. Brown, C. Bordeanu, K. A. Snover, D. W. Storm, D. Melconian, A. L. Sallaska, S. K. L. Sjue and S. Triambak, Phys. Rev. C **76**, 055801 (2007) arXiv:0710.1279 [nucl-ex].

"Multi-layer scintillation detector for the MOON double beta decay experiment: Scintillation photon responses studied by a prototype detector MOON-1," P. J. Doe and the MOON collaborators,* J. Phys. Soc. Jpn **76**, 114201 (2007) arXiv:0609008 [nucl-ex].

"rho^0 Photoproduction in Ultra-Peripheral Relativistic Heavy Ion Collisions with STAR," B. I. Abelev and the STAR collaborators,* Phys. Rev. C **77**, 34910 (2008) arXiv:0712.3320.

"Forward Lambda Production and Nuclear Stopping Power in d+Au Collisions at $\sqrt{s} = 200$ GeV," B. I. Abelev and the STAR collaborators,* Phys. Rev. C **76**, 64904 (2007) arXiv:0706.0472.

"Measurement of Transverse Single-Spin Asymmetries for Di-Jet Production in Proton-Proton Collisions at $\sqrt{s} = 200$ GeV," B. I. Abelev and the STAR collaborators,* Phys. Rev. Lett. **99**, 142003 (2007) arXiv:0705.4629.

"Global polarization measurement in Au+Au collisions," B. I. Abelev and the STAR collaborators,* Phys. Rev. C **76**, 024915 (2007) arXiv:0705.1691.

"Energy dependence of pi, p and pbar transverse momentum spectra for Au+Au collisions at $\sqrt{s_{NN}} = 62.4$ and 200 GeV," B. I. Abelev and the STAR collaborators,* Phys. Lett. B **655**, 104 (2007) arXiv:0703040 [nucl-ex].

"Partonic flow and phi-meson production in Au+Au collisions at $\sqrt{s} = 200$ GeV," B. I. Abelev and the STAR collaborators,* Phys. Rev. Lett. **99**, 112301 (2007)

arXiv:0703033 [nucl-ex].

"Mass, quark-number, and $\sqrt{s_{NN}}$ dependence of the second and fourth flow harmonics in ultra-relativistic nucleus-nucleus collisions," B. I. Abelev and the STAR collaborators,* Phys. Rev. C **75**, 54906 (2007) arXiv:0701010 [nucl-ex].

"Two-particle correlations on transverse momentum and momentum dissipation in AuAu collisions at $\sqrt{s_{NN}} = 130$ GeV," B. I. Abelev and the STAR collaborators,* J. Phys. G **34 No 5**, 799-816 (2007).

"The energy dependence of p_t angular correlations inferred from mean-p_t fluctuation scale dependence in heavy ion collisions at the SPS and RHIC," B. I. Abelev and the STAR collaborators,* J. Phys. G **34**, 451 (2007) arXiv:0605021 [nucl-ex].

"Rapidity and species dependence of particle production at large transverse momentum for d+Au collisions at $\sqrt{s_{NN}} = 200$ GeV," B. I. Abelev and the STAR collaborators,* Phys. Rev. C **76**, 54903 (2007) arXiv:0609021 [nucl-ex].

"Strange particle production in p+p collisions at $\sqrt{s} = 200$ GeV," B. I. Abelev and the STAR collaborators,* Phys. Rev. C **75**, 064901 (2007) arXiv:0607033 [nucl-ex].

"Transverse momentum and centrality dependence of high-pT non-photonic electron suppression in Au+Au collisions at $\sqrt{s_{NN}} = 200$ GeV," B. I. Abelev and the STAR collaborators,* Phys. Rev. Lett. **98**, 192301 (2007) arXiv:0607012 [nucl-ex].

"Delta-phi Delta-eta Correlations in Central Au+Au Collisions at $\sqrt{s_{NN}} = 200$ GeV," B. I. Abelev and the STAR collaborators,* Phys. Rev. C **75**, 034901 (2007) arXiv:0607003 [nucl-ex].

"Scaling properties of hyperon production in Au+Au collisions at $\sqrt{s_{NN}} = 200$ GeV," B. I. Abelev and the STAR collaborators,* Phys. Rev. Lett. **98**, 062301 (2007) arXiv:0606014 [nucl-ex].

"Strangelet Search in AuAu collisions at $\sqrt{s_{NN}} = 200$ GeV," B. I. Abelev and the STAR collaborators,* Phys. Rev. C **76**, 011901 (2007) arXiv:0511047 [nucl-ex].

"Transverse momentum correlations and minijet dissipation in Au-Au collisions at $\sqrt{s_{NN}} = 130$ GeV," B. I. Abelev and the STAR collaborators,* J. Phys. G **34**, 799 (2007) arXiv:0408012 [nucl-ex].

"Polishing the lens: I. Pionic final state interactions and HBT correlations: distorted wave emission-function (DWEF) formalism and examples," G. A. Miller and J. G. Cramer, J. Phys. G **34**, 703-739 (2007).

"Validation of spallation neutron production and propagation within Geant4," M. G. Marino, J. A. Detwiler, R. Henning, R. A. Johnson, A. G. Schubert and J. F. Wilkerson, Nucl. Instrum. Meth. A **582**, 611-620, (2007) arXiv:0708.0848 [nucl-ex].

10.2 Papers submitted or to be published 2008:

"The Cascades proposal for the Deep Underground Science and Engineering Laboratory," W. C. Haxton and J. F. Wilkerson, submitted for publication to the Neutrino 2006 Proceedings, arXiv:0705.3699.

"Centrality evolution of p_t and y_t spectra from Au-Au collisions at $\sqrt{s_{NN}} = 200$ GeV," T. A. Trainor, accepted for publication in Int. J. Mod. Phys. E, arXiv:0710.4504 [hep-ph].

"The azimuth structure of nuclear collisions – I," T. A. Trainor and D. T. Kettler, accepted for publication in Int. J. Mod. Phys. E, arXiv:0704.1674 [hep-ph].

"Azimuth quadrupole component spectra on transverse rapidity $\mathbf{y_t}$ for identified hadrons from Au-Au collisions at $\sqrt{s_{NN}} = 200$ GeV," T. A. Trainor, submitted for publication to Phys. Rev. C, arXiv:0803.4002 [hep-ph].

"KATRIN: an experiment to measure the neutrino mass," R. G. H. Robertson for the KATRIN Collaboration, in Proc. Topics in Astroparticle and Underground Physics, Sendai, Japan, September, 2007, to be published in J. Phys. Conf. Series, arXiv:0712.3893 [nucl-ex].

"Centrality dependence of charged hadron and strange hadron elliptic flow from $\sqrt{s_{NN}} = 200$ GeV Au+Au collisions," B. I. Abelev and the STAR collaborators,* January, 2008, submitted for publication to Phys. Rev. C.

"Forward Neutral Pion Transverse Single Spin Asymmetries in p+p Collisions at $\sqrt{s} = 200$ GeV," B. I. Abelev and the STAR collaborators,* January, 2008, submitted for publication to Phys. Rev. Lett.

"Spin alignment measurements of the K* and phi vector meson at RHIC,"B. I. Abelev and the STAR collaborators,* January, 2008, submitted for publication to the Phys. Rev. Lett.

"Hadronic resonance production in d+Au collisions at $\sqrt{s} = 200$ GeV at RHIC," B. I. Abelev and the STAR collaborators,* January, 2008, submitted for publication to Phys. Rev. C.

"Longitudinal double-spin asymmetry for inclusive jet production in $\vec{p} + \vec{p}$ collisions at $\sqrt{s} = 200$ GeV," B. I. Abelev and the STAR collaborators,* October, 2007, submitted for publication to Phys. Rev. Lett.

"Enhanced strange baryon production in Au+Au collisions compared to p+p at $\sqrt{s_{NN}} = 200$ GeV," B. I. Abelev and the STAR collaborators,* May, 2007, submitted for publication to Phys. Rev. Lett.

"Charged particle distributions and nuclear modification at high rapidities in d+Au collisions at $\sqrt{s_{NN}} = 200$ GeV," B. I. Abelev and the STAR collaborators,* March, 2007, submitted for publication to Phys. Lett. B.

"Determination of Gamow-Teller Strength for ^{40}Ar $\rightarrow^{40}$ K," M. Bhattacharya,

C. D. Goodman and A. García, March, 2008, submitted to Phys. Rev. Lett.

"*ft* value of the $0^+ \rightarrow 0^+$ decay of ^{32}Ar: a measurement of isospin symmetry breaking in a super-allowed decay," M. Bhattacharya, D. Melconian, A. Komives, S. Triambak, A. García, E. G. Adelberger, B. A. Brown, M. W. Cooper, T. Glasmacher, V. Guimaraes, P. F. Mantica, A. M. Oros-Peusquens, J. I. Prisciandaro, M. Steiner, H. E. Swanson, S. L. Tabor and M. Wiedeking, April, 2008, submitted to Phys. Rev. C.

"Limits on Scalar Currents from the $0^+ \rightarrow 0^+$ decay of ^{32}Ar and Isospin Breaking in ^{33}Cl and ^{32}Cl," A. García, November, 2007, submitted to AIP Proceedings of the 4th ANL/MSU/INT/JINA RIA Theory Workshop.

"Neutrino masses and mixings: Status and Prospects," L. Camilleri, E. Lisi and J. F. Wilkerson, April, 2008, submitted for publication to Ann. Rev. Nucl. Part. S, Volume 58.

10.3 Invited talks, abstracts and other conference presentations:

"From Brownian motion to perfect liquid: The conflict continues 100 years later," T. A. Trainor, Seminar, Institute for Theoretical Science, University of Oregon, Eugene, OR, April, 2007.

"What is 'elliptic flow'?," T. A. Trainor, Conference on Early Time Dynamics in Heavy Ion Collisions, McGill University, Montreal, Canada, July, 2007.

"Hydrodynamics in RHIC collisions: Perfect liquid or desert mirage?," T. A. Trainor, Seminar, Los Alamos National Laboratory, Los Alamos, NM, November, 2007.

"Systematics of complete fragment distributions from nuclear collisions," T. A. Trainor, Workshop on 'Parton fragmentation processes: in the vacuum and in the medium,' European Center for Theoretical Studies in Nuclear Physics and Related Areas, Trento, Italy, February, 2008.

"Fragmentation in $e^+ - e^-$ collisions at low Q^2," D. T. Kettler, Workshop on 'Parton fragmentation processes: in the vacuum and in the medium,' European Center for Theoretical Studies in Nuclear Physics and Related Areas, Trento, Italy, February, 2008.

"Plugging leaks and mopping up: Recovering from hydro at RHIC," T. A. Trainor, Seminar, Los Alamos National Laboratory, Los Alamos, NM, March, 2008.

"Future geoneutrino detectors," N. S. Tolich, Applied Antineutrino Physics Workshop, Paris, France, December, 2007.

"A Deep Underground Science and Engineering Laboratory in the U.S.," R. G. H. Robertson, NW Sectional Meeting of the APS, Pocatello, ID, May, 2007.

"Neutrino Observatories, Present and Future," R. G. H. Robertson, Nuclear Astrophysics, 1957 – 2007, Beyond the First Fifty Years, Pasadena, July, 2007.

"The KATRIN Experiment," R. G. H. Robertson, Topics in Astroparticle and Underground Physics (TAUP) International Conference, Sendai, Japan, September, 2007.

"Experimental Determination of Neutrino Mass," R. G. H. Robertson, Focus Meeting on Neutrinos, Institute for Physics and Mathematics of the Universe, Kashiwa, Japan, March, 2008.

"Recent Axion Search Experiments: A New Torsion Pendulum and Other Methods," S. A. Hoedl, Stanford Linear Accelerator Center, Stanford, California, January, 2008.

"A Torsion Pendulum Axion Search," S. A. Hoedl, California Institute of Technology Nuclear Physics Seminar, Pasadena, California, October, 2007.

"Electron-neutrino correlation and Isospin Breaking in the $0^+ \rightarrow 0^+$ decay of ^{32}Ar," A. García, November 2007, 4th ANL/MSU/INT/JINA RIA Theory Workshop, Seattle, WA, September, 2007.

"Background simulations and detector design for the KATRIN experiment," M. L. Leber, T. H. Burritt, J. A. Dunmore, P. J. Doe, J. A. Formaggio, R. G. H. Robertson, M. Steidl, B. A. VanDevender, B. L. Wall and J. F. Wilkerson, IEEE Nuclear Science Symposium Conference Record, November, 2007.

"Henry Primakoff Lecture, Neutrinoless Double-Beta Decay," J. F. Wilkerson, APS Spring Meeting, Jacksonville, FL, April, 2007.

"Neutrinoless Double-Beta Decay Program," J. F. Wilkerson, NSAC Long Range Plan Working Group Meeting, Galveston, TX, May, 2007.

"2007 Nuclear Physics Long Range Plan and DUSEL," J. F. Wilkerson, DUSEL Town Meeting, Washington, DC, November, 2007.

"B1. Low Level Counting, Radon control, ultra-pure materials, and Homeland Security Cross-Cutting Working Group White Paper," J. F. Wilkerson, P. Cushman and J. F. Wilkerson, DUSEL Town Meeting, Washington, DC, November, 2007.

"Neutrinos – Extreme properties, revolutionary consequences," J. F. Wilkerson, Physics Colloquium, University of North Carolina, Chapel Hill, NC, November, 2007.

"Searching for Neutrinoless Double-Beta Decay," J. F. Wilkerson, Physics Seminar, University of Illinois, Champagne-Urbana, IL, March, 2008

"Searching for Neutrinoless Double-Beta Decay," J. F. Wilkerson, Physics Seminar, National Institute of Standards and Technology, Gaithersburg, MD, March, 2008

"Going Deep – Nuclear Science Underground ," J. F. Wilkerson, APS Spring Meeting, St. Louis, MO, April, 2008.

*UW collaborators for the various CENPA research groups are listed below (April 1, 2007 - March 31, 2008):

MOON Collaborators: P. J. Doe, V. M. Gehman, R. G. H. Robertson, J. F. Wilkerson and D. I. Will

SNO Collaborators: J. F. Amsbaugh, T. H. Burritt, G. A. Cox-Mobrand, P. J. Doe, C. A. Duba, G. Harper, M. A. Howe, S. McGee, A. Myers, N. S. Oblath, R. G. H. Robertson, N. Tolich, B. A. VanDevender, T. D. VanWechel, B. L. Wall, J. F. Wilkerson

STAR Collaborators: H. Bichsel, J. G. Cramer, D. T. Kettler, R. J. Porter, D. J. Prindle and T. A. Trainor. In cases where some CENPA personnel played a major role in a STAR publication, their names are listed explicitly.

10.4 Ph.D. degrees granted:

The Isobaric Multiplet Mass Equation and ft Value of the $0^+ \rightarrow 0^+$ *Fermi Transition in* ^{32}Ar*: Two Tests of Isospin Symmetry Breaking*, Smarajit Triambak (May, 2007).

A Torsion Balance Search for Spin-Coupled Forces, Claire E. Cramer (August, 2007).

Physics Reach of the Global Neutrinoless Double-Beta Decay Program and Systematic Uncertainties of the Majorana Project, Victor M. Gehman, (August, 2007).

Data Integrity and Electronic Calibrations for the Neutral Current Detector Phase Measurement of the 8B Solar Neutrino Flux at the Sudbury Neutrino Observatory, Adam Cox-Mobrand, (January, 2008).